FACULTY
OF MATHEMATICS
AND PHYSICS
Charles University

DOCTORAL THESIS

RNDr. Katarína Pekárková
(Ridzoňová)

Optical methods for characterization of semiconductor radiation detectors

Institute of Physics of Charles University

Supervisor of the doctoral thesis: doc. Ing. Eduard Belas, CSc.

Study programme: Physics

Specialization: Quantum Optics and Optoelectronics

Prague 2023

I declare that I carried out this doctoral thesis independently, and only with the cited sources, literature and other professional sources.

I understand that my work relates to the rights and obligations under the Act No. 121/2000 Coll., the Copyright Act, as amended, in particular the fact that the Charles University has the right to conclude a license agreement on the use of this work as a school work pursuant to Section 60 paragraph 1 of the Copyright Act.

In Prague date 13.10.2023 Signature: RNDr. Katarína Pekárková

Acknowledgment

Especially, I would like to thank my supervisor doc. Ing. Eduard Belas, CSc. for the procreative discussions about the ideas of the work and experiments, and Prof. RNDr. Roman Grill, CSc. for his patience with long-lasting valuable theoretical discussions. I am also thankful to doc. Ing. Petr Praus, CSc., RNDr. Jakub Pekárek, PhD. and other colleagues at the Institute of Physics at Charles University for their help in my research and study. Further, I am grateful to my colleagues from the Institute of Physics of the Czech Academy of Sciences, specifically to Ing. Lucia Landová and Amalraj Peter Amalathas, PhD. for sample preparation and to doc. Jakub Holovský, PhD., Mgr. Zdeněk Remeš, PhD. and Mgr. Maksym Buryi, PhD. for their support in my research. My thanks also belong to my parents, Anna Ridzoňová, Ľúbomír Ridzoň, brother Ľubomír Ridzoň, my husband Jakub Pekárek, my closest friends, Jana Krížová and Tomáš Bažant, and my animal companions, Haka, Emil and Minnie, for their support during my whole study at Charles University. At last, I would like to thank the Charles University Grant Agency for the financial support of the part of my PhD study.

Title: Optical methods for characterization of semiconductor radiation detectors

Author: RNDr. Katarína Pekárková (Ridzoňová)

Department/ Institute: Institute of Physics of Charles University

Supervisor of the doctoral thesis:
doc. Ing. Eduard Belas, CSc., Institute of Physics of Charles University

Abstract:

CdZnTe and perovskites are promising materials for radiation detectors. Here, we address the main obstacles to their application, CdZnTe charging, and perovskite stability by photocurrent measurements. In the first part, models describing space-charge-limited photocurrents are developed, and an excellent agreement with measured data is obtained. The Drift-diffusion model provided us with a detailed defect analysis of CdZnTe. A linear rise of photocurrent at low voltage originates in the trapping of injected holes close to the cathode. We propose a simple procedure to evaluate space-charge density from photocurrents. The influence of space-charge, photoconductive gain, and shallow levels result in inaccurate evaluation of mobility-lifetime product via photoconductivity. The second part focuses on light-induced changes in perovskites. Laser-induced transient current measurements show improvements in hole lifetime and surface recombination in $CH_3NH_3PbBr_3$ single crystals. We further study phase segregation in mixed-halide perovskites by Fourier-Transform photocurrent spectroscopy. The recorded gradual formation of an I-rich phase correlates with an increase in deep defect concentration, which we attribute to charged iodide interstitials. Phase segregation is associated with iodide migration through interstitial positions. The importance of grain size in determining the degree of segregation is pointed out.

Keywords: CdTe/ CdZnTe, transient-current technique, photocurrent, surface recombination, space-charge, photoconductive gain, perovskite, deep defects, ion migration, Fourier-transform photocurrent spectroscopy, light-soaking, phase segregation, grain size

Contents

1. Introduction

1.1 Ionizing radiation detectors

The high-energy photon radiation, including X-rays with photon energies 0.1-100 keV and gamma rays with photon energies 0.1-100 MeV, have thanks to their strong penetration a wide use in non-destructive probing of condensed matter. Radiation rays find applications in medical imaging, security monitoring, defect and contamination inspection, radiotherapy, nuclear physics, astrophysics, etc. [1]–[4].

Semiconductor-based radiation detectors work similarly to photodetectors which operate in the UV-visible-infrared light ranges. Semiconductors with an appropriate bandgap can easily detect radiation-induced free charges under the applied voltages and produce corresponding current signals. Current X-ray and gamma-ray radiation detectors are mainly based on silicon (Si), germanium (Ge), cadmium telluride (CdTe), cadmium zinc telluride (CZT), amorphous selenium (a-Se), mercury iodide (HgI_2) and thallium bromide (TlBr) [1], [5]. A high-performance direct radiation detector should possess several key features. First, high bandgaps ranging from 1.5 eV to 2.5 eV are required to reduce thermal noise due to band-to-band thermal generation of free electrons and holes, which further contributes to the dark current. Another key feature is the large average atomic number Z and high mass density, which increases the probability of the absorption of high-energy radiation within the device. Carrier mobility- lifetime product $\mu\tau$ is also an important factor of suitable semiconductors as it ensures a long carrier diffusion length and thus reduces the charge carrier recombination probability. [1], [5], [6].

Besides direct radiation detectors, radiation can also be detected using scintillators, which first convert high-energy particles and photons into ultraviolet-visible light via radio luminescence. This luminescence is further detected by photodetectors such as Si photodiodes, complementary metal-oxide semiconductors (CMOS), avalanche photodiodes, charge-coupled devices (CCDs) or photomultiplier tubes (PMTs). Thus, the performance of the scintillator is highly dependent on the conversion efficiency.

The sensitivity of current commercial detectors is insufficient, especially in computed tomography (CT) scanning, where a high radiation dose must be used as a

consequence of the low sensitivity of radiation detectors. According to a study in [7] ~2% of cancers could be related to the performed CT scans. Moreover, current commercially used radiation detectors usually require costly growth methods and severe operating conditions.

The first part of the work focuses on the material characterization of CdZnTe, which has already shown excellent performance in commercial radiation detectors [8]. Combining photocurrent and time-of-flight measurements, we discuss the transport properties and the influence of deep and shallow defects on charge-collection efficiency. In the second part of the thesis, we focus on lead halide perovskites, which also have a high potential in radiation detection. We study perovskite transport properties and their insufficient stability under irradiation.

1.2 CdTe/ CdZnTe

Cadmium Telluride (CdTe) belongs to the II-VI group of semiconductors and crystallizes in a cubic zinc-blende structure with a lattice constant a = 0.648 nm [9], as can be seen in Fig. 1a. CdTe has been studied as an X-ray and gamma-ray detector since the 1960s. The main advantage of CdTe detectors is no necessity of cooling them down. This is thanks to its wide direct bandgap of 1.5 eV at room temperature [9], which lowers thermal noise caused by band-to-band thermal generation of free electrons. A relatively high average atomic number of 50 increases the probability of high-energy radiation absorption. For comparison, a widely-used semiconductor Si has a smaller atomic number Z of 14 and a smaller bandgap of 1.12 eV, which leads to larger dark currents at room temperature [10]. Thanks to other unique properties of CdTe, such as high carrier mobility, high resistivity, chemical and structural stability, and surface properties allowing the formation of good Ohmic contact with metals, CdTe is a promising material not only in applications connected with radiation detection [8], [9].

Substitution of Cd with zinc (Zn) in cadmium zinc telluride $Cd_{1-x}Zn_xTe$ (CZT) leads to the increase of the band-gap energy (1.57 eV at room temperature for x~0.1) [8]. The resistivity of CZT detectors thus reaches higher values of 10^9 to 10^{10} Ω·cm [5] in comparison with CdTe. The state-of-the-art CZT detectors reach an excellent energy resolution of 0.5% at room temperature [8], [11]. This is close to the best

current energy resolution (0.3%) of the high-purity geranium-based detector (HPGe) [12], which, however, requires cryogenic cooling. The disadvantage of CZT is that the zinc concentration is a function of position within CZT due to the Zn segregation coefficient in CZT [13]. Consequently, the defect concentration also varies along the crystal growth axis thanks to what the detector-grade material properties are achieved only in part of the crystal. Further, the high price of single crystal fabrication limits the CdTe/ CZT in its broader commercial application.

CZT detectors are nowadays commercially used in mammographic X-ray imaging [14] and have been also used as sensors in astrophysics (in satellite INTEGRAL and the NASA mission SWIFT) [15]. Another important field of use is application in solar cells. Currently, CdTe thin films are the second most common photovoltaic technology (occupying 5% of the market) after conventional crystalline Si-based solar cells. The current state-of-the-art CdTe thin films have reached a power conversion efficiency (PCE) of 22%, which is close to the record efficiencies of the crystalline Si solar cells [16]. The advantage of CdTe thin film-based photovoltaic technologies over Si solar cells is the lower cost of preparation [17]. CdTe/ CdZnTe may be further used in electro-optic modulators [18] and as a substrate for the epitaxial growth of the semiconductor $Hg_{1-x}Cd_xTe$ [19], which is used as an infrared radiation detector.

The CdTe/ CZT single crystals are most often grown by the Vertical High-Pressure Bridgman Method (HPB), Traveling Heater Method (THM), and Vertical gradient Freeze Method (VGF) [20]–[24]. The HPB method works at high temperatures above the melting point of grown material and therefore results in higher defect concentrations [25], [14], [26]. Defects such as grain boundaries, twinning, stacking faults, zinc segregation, and Te inclusions and precipitates where Te segregates as a separate phase, may be introduced within the CZT crystal [25]. Trapping and recombination on these defects may lead to a decreased value of the mobility-lifetime product and to the formation of space charge, which may shield the applied bias and thus reduce the resulting charge collection efficiency (CCE). After the growth, the crystal ingot is cut into wafers and subsequent smaller monocrystalline samples.

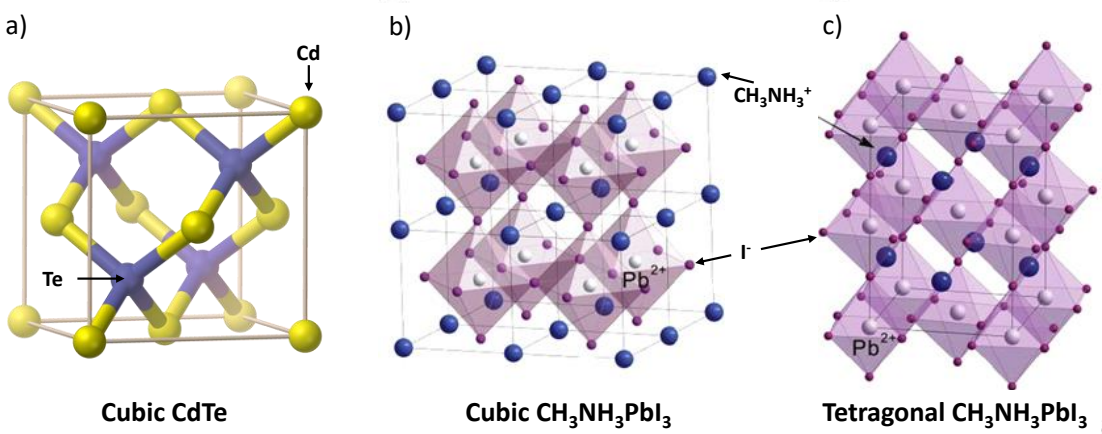

Fig. 1: Crystal structure of a) CdTe (here yellow and purple balls represents Cd and Te atoms, respectively), b) $CH_3NH_3PbI_3$ in a cubic phase and c) $CH_3NH_3PbI_3$ in a tetragonal phase (here blue balls represents $CH_3NH_3^+$ cation, blue balls are Pb atoms and purple balls are I atoms). b), c) is reprinted from reference [183].

1.3 Lead halide perovskites

Term perovskite generally refers to any material with a crystal structure of $CaTiO_3$ and chemical formula AMX_3. In this thesis, we will focus on the specific group of organic-metal halide perovskites which were for the first time reported by Weber in 1978 [27]. Here, A corresponds to organic cation, typically $MA^+ = CH_3NH_3^+$, $FA^+ = CH(NH_2)_2^+$ and/or Cs^+. M represents divalent metal cation, such as Pb^{2+} or Sn^{2+}, and X monovalent halogen anion I^-, Br^-, or Cl^-. The crystal structure of lead halide perovskites depends on the composition and the temperature. The most investigated methylammonium (MA) lead iodide, $CH_3NH_3PbI_3$ (MAPI), exists at room temperature in a tetragonal (I4/ mcm) structure while $CH_3NH_3PbBr_3$ (MAPB) in a cubic (Pm-3m) structure [28]–[30] (see Fig. 1). At temperatures above 165 K and 327 K, MAPI have the transition from orthorhombic to tetragonal and to cubic structures, respectively. Regarding the crystal structure of mixed-halide perovskites, $MAPb(I_xBr_{1-x})_3$ at room temperature undergoes a cubic-to-tetragonal phase transition for $x > 0.2$ [31]. Thanks to the weak bond between organic cations A and inorganic framework, the AMX_3 perovskites have soft crystal lattices and show mixed electronic-ionic behaviour [32].

Halide perovskites have been the focus of intense scientific research due to their advantageous properties ranging from low-cost manufacturing [33], high carrier

diffusion length of over 1000 nm [34], long carrier lifetime of 200 ns or even 1μs [35], [34], high absorption coefficient, sharp absorption edge onset [36], and defect tolerance [37]. MAPI is a direct bandgap semiconductor (1.55 eV) with a strong absorption coefficient in the order of $1.5\times10^4 cm^{-1}$ at 550 nm [36]. Although carrier mobilities ranging from 10^1 $cm^2/V{\cdot}s$ to 10^2 $cm^2/V{\cdot}s$ [5], for thin films and single crystals, respectively, are lower than those of Si and GaAs, they are still at least three orders of magnitude higher than those of many organic semiconductors. In the case of single crystals, which have reduced trap density thanks to the absence of grain boundaries, the diffusion length of holes increases to 175 μm and mobility-lifetime product μτ of holes to 1.2×10^{-2} cm^2V^{-1} [5]. The hole μτ in $MAPbI_3$ and $MAPBr_3$ single crystals have thus comparable values as those for CZT crystals.

Thanks to these properties, perovskites are highly promising materials for solar cells (PSCs), photodetectors, lasers, transistors, light-emitting diodes, and memory devices. Regarding solar cells, single-junction perovskite devices now reach a power conversion efficiency of >25% [38]. In addition, the low temperature of deposition and bandgap tunability of mixed-halide perovskites $AM(I_xBr_yCl_{1-x-y})_3$, with more than one type of halide anion, also makes them well-suited for multi-junction solar cells. The bandgaps can be tuned between 1.2 and $>$ 2 eV.

The high atomic numbers of Cs^+, Pb^{2+}, Sn^{2+}, I^-, and Br^- ions of 55, 82, 50, 53, and 35, respectively, combined with the large density of perovskite (4 g/cm^3) make halide perovskites also promising semiconductor for radiation detection [5]. Halide perovskites have thus a comparable attenuation coefficient to CdZnTe [5]. In addition, they have low-cost fabrication at low temperatures (below 150 °C).

Despite constant progress, the perovskite long-term stability remains the main drawback of their commercialization. For example, the longest reported lifetime of perovskite solar cells is about 1 year under standard operation conditions [39] which is still far from a 25-year warranty on silicon photovoltaic modules. While degradation pathways due to oxygen and moisture exposure may be managed by the encapsulation, stimuli like light, heat, and electrical bias cannot be avoided during operation. The lack of stability of perovskite devices has been explained by ion migration inside the material [40], [41]. Ion migration refers to a process when ions inside perovskite become mobile and hop through the perovskite lattice. This may be

induced by external bias application or by irradiation in both polycrystalline and single perovskite crystals [42]. The prevailing migrating species are halide ions, thanks to their low activation energies for the migration of [42]. The diffusion/drift of MA^+ cations with higher activation energies for migration has been, however, also observed [43]. The grain boundaries, lattice distortion, and large density of point defects have been reported as the main paths enhancing ion migration [29], [44]–[48]. Ion migration is more severe in iodine-based than bromine-based perovskites and may be further mitigated by replacing MA^+ cation with FA^+ or Cs^+ [5], [42].

Besides a negative effect on long-term stability, the ion conductivity in perovskites also leads to short-term phenomena such as the hysteresis effect and polarization effect. The hysteresis consists of the discrepancy of the measurements under applied bias, where the measured curve depends on the time of applied voltage, rate of scanning, and the scan direction (forward or reverse scanning). The polarization effect refers to the screening of the internal electric field, which may fall to zero or negligibly small values under one electrode. As a consequence, charge carrier drift is here negligible, and the probability of charge carrier recombination increases. This negatively affects the resulting CCE of the radiation detector. The polarization originates in the space charge, which forms by migrating ions or trapped charge carriers accumulation under the corresponding electrode. The last one is the leading cause of polarization in CZT detectors [49].

1.4 Motivation and goals

Despite an extensive research effort to improve the single crystal growth technology for CZT radiation detectors, the resulting quality of CdTe/CZT crystals is still not sufficient for their wide commercial use. Reduction of defects such as dislocations, grain boundaries, twinning, zinc segregation, and tellurium inclusions together with the reduction of material growth cost remains an open issue. To effectively study and compare fabrication methods, there is a necessity to develop simple and fast experimental methods for the characterization of prepared detectors.

Optical methods are massively used in material physics. One of the most used methods to evaluate important transport properties of semiconductors, such as the carrier mobility-lifetime product $\mu\tau$, are steady-state photocurrent-voltage

characteristics. Photocurrents are often evaluated by Many´s equation which presumes a uniform internal electric field and so neglects the impact of a space charge [50]–[55]. Substantial space charge influencing applied bias can be created within the material as a consequence of photo-carriers trapping at deep defect levels or as a consequence of ion migration.

Many´s equation has been used to determine μτ on various semiconductor materials such as CdZnTe [50]–[52], [54]–[56], HgI_2 [57], [58], Tl_4CdI_6 [59], SbSeI [60], $TlSi_4$ [61], $Cs_2Hg_3S_4$ [62], hexagonal boron nitride [63]–[67], $CH_3NH_3PbI_3$ [68], $CsPbBr_3$ [69] and others. However, to the best of our knowledge, none of the papers assessed the validity of the homogeneous field assumption, and the accuracy of the approach is thus doubted.

In this thesis, we complete photoconductivity measurements under above-band-gap illumination by laser-induced transient current technique to study the space charge formation in CdZnTe. To include space charge formation, three models, SCLP1, SCLP2, and drift-diffusion model, describing space-charge limited photocurrents are developed (sections 2.4, 2.5, and 2.6, respectively). An excellent agreement with measured data was obtained (section 4.1). Detailed analysis done on the CdZnTe sample proves that the right μτ exceeds five times the μτ obtained by the fit of Many's equation. The thesis will not only help to prevent the misuse of Many´s relation in future works but also give numerical tools for detailed defect structure analysis of studied material. Understanding defect structure and its influence on charge carrier transport is crucial for the further development of detector-grade CdTe/ CZT materials.

The second part of this thesis is devoted to perovskite materials whose poor long-term stability under illumination remains an obstacle to their commercialization. For example, light may enhance ion migration, formation of new defects, lattice disordering, or can cause redistribution of halides in mixed-halide perovskites [31]. A precise mechanism of degradation and especially the role of deep defect levels is not yet well understood. More importantly, only a little attention has been paid to the effect of light on charge carrier transport properties.

In section 5, we emphasized understanding the transport properties and light-induced effects of $CH_3NH_3PbBr_3$ single crystals. For this purpose, we performed L-TCT under continuous illumination as previously on CdZnTe (section 4).

In Section 6, we investigated the so-called phase segregation of mixed-halide perovskites into I-rich and Br-rich domains. This phenomenon occurs in mixed-halide $APb(I, Br)_3$ perovskites with a bandgap >1.65 eV under continuous illumination or applied electric field [29], [31]. The process was first recorded by photoluminescence (PL) redshift under prolonged illumination, further light-soaking (LS). This shift resulted from the formation of small I-rich narrow bandgap clusters that were highly emissive [29]. Extensive research has been performed to understand the mechanisms controlling phase segregation and mitigate it. The segregation is driven by excited charge carriers [44], [70]–[73] and surface quality and overall crystallinity plays an important role [74], [75]. Several solutions have been found to mitigate phase segregation by passivating bulk and interfacial defect states (e.g. by adding a small amount of Cl [76]) or by replacing MA^+ with FA^+ or Cs^+ [77], [71].

While phase segregation is known to result from halide transport, the exact halide migration channels and the force driving the process remain elusive. A comparison of the segregation rates in either halide-deficient or halide-excessive perovskites when halide vacancies or interstitials prevail, respectively, has led to the conclusion that the process is vacancy-mediated [47], [78], [79]. However, LS itself may create additional defects which may further affect phase segregation. There are only a few works that have recorded such light-induced formation of deep defects in mixed-halide perovskites [80], [81]. Understanding how deep defect levels are linked to phase segregation and what are the main ion migration channels is crucial to suppress phase segregation. However, a detailed evolution of light-induced defects under illumination of mixed-halide perovskites is still missing, and it remains unclear how these defects are linked to phase segregation. Here, we record a detailed evolution of deep defects under illumination in mixed-halide perovskites and point to a strong correlation between the concentration of light-induced deep defects and phase segregation rate. Moreover, we show the importance of grain size in determining the degree and terminal phase of segregation. These observations may open up new possibilities for suppressing phase segregation.

2. Theory

The electrons in an isolated atom may occupy only discrete energy levels. However, when a large number of atoms N join together to form a crystal lattice, the discrete energy levels spread into continuous energy bands, thanks to the overlapping of atomic orbitals with the nearby orbitals. At absolute zero temperature, the electrons in the semiconductor fill several energy bands, leaving the rest of the energy bands empty [6]. The highest-filled band is called the valence band E_V. The next conduction band E_C is separated from the valence band by an energy band-gap E_g with forbidden energetic states. However, energy levels may also form inside the energy band gap thanks to the defects and impurities in the crystal lattice. Levels localized close to the valence or conduction band with activation energy in the order of thermal energy k_BT are called shallow levels and generally act as dopants (donors or acceptors). The levels positioned in the middle of the band gap, called deep levels, may act as recombination or trap centres [6].

At thermodynamic equilibrium, the probability that an electron occupies the energy level E_t is given by the Fermi-Dirac distribution function [6]:

$$f(E_t) = \frac{1}{1 + e^{(E_t - E_F)/(k_B T)}}. \tag{2.1}$$

Here k_B is the Boltzmann constant, T is the absolute temperature in Kelvin, and E_F is the Fermi energy level, representing the hypothetical energy state with a 50% probability of being filled by an electron regardless of the temperature. In the case of non-degenerate semiconductors, which have low dopant concentration in the range of ppm and their Fermi energy is at least $3k_BT$ away from either band edge, the Boltzmann statistics may be used. Considering that the bottom of the conduction band is set to zero, the electron density on trap level n_t and electron density near the bottom of conduction band n are then given as [6]

$$n = N_C \exp\left(\frac{E_F}{k_B T}\right) \tag{2.2}$$

$$n_t(E_t) = N_t \exp\left(\frac{E_F - E_t}{k_B T}\right) \tag{2.3}$$

Here N_c and N_t represent the effective density of states in the conduction band and the effective density of states on trap level, respectively. The ratio of the free electron density n and trapped electron density n_t is expressed by parameter θ

$$\theta = \frac{n}{n_t} = \frac{N_C}{N_t} \exp\left(\frac{E_t}{k_B T}\right), \tag{2.4}$$

The dimensionless parameter θ depends only on the material parameters, like the effective mass of electrons in the conduction band, and the temperature.

2.1 Charge carrier transport parameters

The charge carrier mobility μ is an important material parameter, which define the ability of an electron/ hole to move through a semiconductor in the presence of applied electric field E with drift velocity v_{dr} [6]

$$\mathbf{v_{dr}} = \mu \mathbf{E}. \tag{2.5}$$

Its value is affected by collisions of carriers with other carriers, crystal defects, and with phonons (lattice vibrations). For average time τ_m between two scattering events, the electron mobility may be defined as [6]

$$\mu_e = \frac{e}{m_e^*} \tau_m, \tag{2.6}$$

where m_e^* is the effective mass of the electron. Carrier mobility is further related to Einstein carrier diffusion coefficient [6]

$$D_e = \left(\frac{k_B T}{e}\right) \mu_e \tag{2.7}$$

where k_B corresponds to Boltzmann constant and T to absolute temperature.

The conductivity σ of semiconductor in the dark is connected with electron and hole mobility by the following equation [6]

$$\sigma_0 = e(n_0 \mu_{e0} + p_0 \mu_{h0}), \tag{2.8}$$

where n_0 and p_0 correspond to the densities of free electrons and holes. Under sample illumination, the dark conductivity increases by the photoconductivity Δσ. This may result either from the increase in electron density by the value Δn or from the change of mobility by the value $\Delta \mu_e$ [82]

$$\sigma = \sigma_0 + \Delta\sigma = (n_0 + \Delta n) e (\mu_{e0} + \Delta \mu_e). \tag{2.9}$$

Change in electron mobility $\Delta\mu_e$ can be induced, for instance, by the light-induced formation of new charged defects, which further affect the rate of electron scattering events, or directly by changing the scattering cross sections of existing charged defects [82]. The increase in electron density Δn is directly proportional to the photoexcitation rate *G* [82]

$$\Delta n = G\tau_e. \tag{2.10}$$

Here τ_e corresponds to the electron lifetime, which is defined as the average time during which the charge carriers contribute to the conductivity [82]. Charge carriers stop participating in conductivity after recombination or after extraction under applied bias without replenishment from the opposite electrode. The lifetime may be also interrupted by the trapping of charge carriers and restored after the de-trapping. Neglecting changes in mobility under illumination and dark free carrier density n_0 compared to Δn, we get for the mobility-lifetime product

$$\frac{\Delta\sigma}{Ge} = \mu_e\tau_{e.} \tag{2.11}$$

The mobility-lifetime product thus represents a quantity of the sensitivity to photoexcitation. Similar relationships also apply to holes.

2.2 Modified Hecht equation

Consider that a monochromatic light is incident on a negatively charged electrode of a homogeneous semiconductor of thickness L and that the internal electric field E is perpendicular to the surface of the contacts. Then it is enough to consider only a one-dimensional current in the direction of the x-axis and the continuity equation for electrons in the equilibrium state may be used [6], [82]:

$$\mathrm{G(x)} - \frac{\mathrm{n(x)}}{\tau_e(\mathrm{x})} - \mu_e \mathrm{n(x)}\frac{\mathrm{dE(x)}}{\mathrm{dx}} - \mu_e \mathrm{E(x)}\frac{\mathrm{dn(x)}}{\mathrm{dx}} + \mathrm{D_e}\frac{\mathrm{d^2n(x)}}{\mathrm{dx^2}} = 0. \tag{2.12}$$

Here G(x) represents the number of photo-generated electrons per second in the volume unit, D_e Einstein electron diffusion coefficient, μ_e electron mobility, and τ_e electron lifetime. For negligible space charge and hence homogenous electric field profile, the third term of eq. (2.12) may be skipped. The diffusion currents, which are represented by the fifth term in eq. (2.12), may be also neglected compared to the

drift currents under applied electric field. The continuity equation may be then simplified as:

$$G(x) - \frac{n(x)}{\tau_e} - \mu_e E(x) \frac{dn(x)}{dx} = 0. \quad (2.13)$$

2.2.1 Below-bandgap illumination

For the photon energy lower than the bandgap ($h\nu < E_g$), electron-hole pairs may be generated within the whole volume of the semiconductor and one may assume a uniform carrier generation $G \neq G(x)$. The total current density is given by the contribution of electrons and holes, $j = j_e + j_h$, while analogous relations apply to electron and hole current density. The electron current density is given as [83]:

$$j_e = e\mu_e \frac{E}{L} \int_0^L n dx = eG\mu_e\tau_e \left(1 - \frac{\mu_e\tau_e E}{L}\right)\left[1 - \exp\left(-\frac{L}{\mu_e\tau_e E}\right)\right]. \quad (2.14)$$

2.2.2 Above-bandgap illumination

For the photon energy of incident light higher than the bandgap ($h\nu > E_g$), electron-hole pairs are generated in the close vicinity of the illuminated cathode. The total photo-current density consists only of the electron current density. Holes immediately recombine at the illuminated cathode. The generation velocity G at the surface is given by the sum of the number of carriers leaving the surface per second and the number of carriers recombining per second in unit area [83]:

$$G(0) = \mu_e E n(0) + n(0) s_e, \quad (2.15)$$

where s_e corresponds to the surface recombination velocity. As seen from eq. (2.15), the concentration of electrons under an illuminated cathode fulfils the following boundary condition:

$$n(0) = \frac{G}{\mu_e E + s_e}. \quad (2.16)$$

Considering that G(x) = 0 for x >0 in the case of above-bandgap light and boundary condition (2.16), the solution of continuity eq. (2.13), takes the following form:

$$n(x) = \frac{G}{\mu_e E + s_e} \exp\left(-\frac{x}{\mu_e\tau_e E}\right). \quad (2.17)$$

Electron current density is then according to the Ohm´s law [83]:

$$j_e = \frac{e\mu_e E}{L}\int_0^L n dx = \frac{eGs_e}{1+\frac{s_e}{\mu_e E}}\frac{\mu_e\tau_e E}{L}\left[1-\exp\left(-\frac{L}{\mu_e\tau_e E}\right)\right]. \quad (2.18)$$

Introducing constant

$$J_0 = eGs_e/S, \quad (2.19)$$

where S represents the surface of illuminated area, we get Modified Hecht equation:

$$J = \frac{J_0}{1+\frac{s_e}{\mu_e E}}\frac{\mu_e\tau_e E}{L}\left[1-\exp\left(-\frac{L}{\mu_e\tau_e E}\right)\right]. \quad (2.20)$$

The equation (2.20), also known as Many´s equation [83], represents the most used approach to fit the dependence of photocurrent *J* on internal electric field *E*. As follows from eq. (2.20), in case of low fields, satisfying condition $\mu E \ll L/\tau_e$, the photocurrent changes as the square of the applied voltage. For medium fields, lying in the range $(L/\tau_e, s_e)$, the photocurrent depends linearly on the voltage. In the case of strong electric fields, when drift velocity $\mu_e E \gg s_e$, there is no loss of carriers due to recombination and the photocurrent saturates at its maximal value.

2.3 Space-charge limited currents (SCLC)

Let´s assume a non-degenerate semiconductor of thickness L, placed in the dark, on which we apply external voltage V. When the injecting cathode is the only source of free carriers, the conductivity is caused only by injected electrons, which subsequently are collected by the opposite grounded non-injecting electrode. The contribution of holes and edge effects is neglected, which reduces the solution to a one-particle, one-dimensional problem. Furthermore, let´s assume ohmic contacts, no band bending at the metal-semiconductor interface, and negligible diffusion currents.

The trapping of injected carriers on defect level E_t inside the bandgap of the material may lead to the formation of space charge and subsequent screening of the electric field. The created space charge density ρ under internal electric field E is governed by the Poisson equation [82]:

$$\frac{\partial \mathrm{E}}{\partial \mathrm{x}} = \frac{\rho}{\epsilon_0 \epsilon_\mathrm{r}}, \tag{2.21}$$

where ϵ_0 and ϵ_r are vacuum and relative permittivity, respectively. The space charge density expresses the increase in charge of free and trapped electrons after illumination:

$$\rho = -\mathrm{e}(\mathrm{n} - \mathrm{n}_0 + \mathrm{n}_\mathrm{t} - \mathrm{n}_{\mathrm{t}0}). \tag{2.22}$$

Here n_0 and $\mathrm{n}_{\mathrm{t}0}$ represent the initial density of free and trapped electrons prior to the illumination. Using the relation (2.3) for n_t and analogous relation for $\mathrm{n}_{\mathrm{t}0}$, neglecting the concentration of free electrons before illumination compared to n as well as 1 compared to $1/\theta$ (see. eq. (2.4)), the space charge density may be expressed in the following approximation:

$$\rho = -\mathrm{e}(\mathrm{n} - \mathrm{n}_0)\left(1 + \frac{1}{\theta}\right) \cong -\frac{\mathrm{en}}{\theta}. \tag{2.23}$$

By substituting (2.23) into the Poisson's equation (2.21), we get the free electron density

$$\mathrm{n} = -\frac{\epsilon_0 \epsilon_\mathrm{r} \theta}{\mathrm{e}} \frac{\partial \mathrm{E}}{\partial \mathrm{x}}. \tag{2.24}$$

One may obtain the relationship for the current density using the Ohm´s law $\mathrm{j} = -\mathrm{e}\mu_\mathrm{e}\mathrm{nE}$ and a derivative of a composite function [84]

$$\mathrm{j} = \epsilon_0 \epsilon_\mathrm{r} \theta \mu_\mathrm{e} \mathrm{E} \frac{\partial \mathrm{E}}{\partial \mathrm{x}} = \frac{\epsilon_0 \epsilon_\mathrm{r} \theta \mu_\mathrm{e}}{2} \frac{\partial}{\partial \mathrm{x}} (\mathrm{E}^2). \tag{2.25}$$

By integrating (2.25) in the range from 0 to x, we get the relation between the current density j and the local electric field E(x):

$$\mathrm{jx} = \frac{\epsilon_0 \epsilon_\mathrm{r} \theta \mu_\mathrm{e}}{2} [\mathrm{E}^2(\mathrm{x}) - \mathrm{E}^2(0)]. \tag{2.26}$$

In the case of one injecting contact, the large density of injected carriers just below this contact shields the local electric field E to negligible values and the boundary condition E(0)=0 can be considered [84]. The validity of such boundary condition can also be justified by maintaining a constant current density j. It then follows from Ohm's law that a large concentration of carriers n corresponds to a small field E, and conversely.

By solving the quadratic equation (2.26) for the field E(x), we get

$$E(x) = \pm \sqrt{\frac{2jx}{\epsilon_0 \epsilon_r \theta \mu_e}}. \tag{2.27}$$

Here only the solution with negative sign has physical meaning with respect to our sign convention. The dependence of the current on the applied voltage may be obtained by integrating (2.27) from zero to the sample thickness L

$$U = \frac{2}{3} \sqrt{\frac{2j}{\epsilon_0 \epsilon_r \theta \mu_e}} L^{3/2}. \tag{2.28}$$

As follows from (2.27), the current flowing through a semiconductor with one injection contact is proportional to the square of the applied voltage

$$J_{SCLC} = \frac{9}{8} \frac{\epsilon_0 \epsilon_r \theta \mu_e V^2}{L^3}. \tag{2.29}$$

The above dependence represents the single-particle Mott-Gurney law [84], also known by the abbreviation SCLC (space charge limited currents).

2.4 Space-charge limited photocurrents 1 (SCLP1)

In this section, we introduce our simplest analytical model to describe space-charge limited photocurrents, further denoted SCLP1. This model is advantageous for the initial characterization of the most important processes occurring in a sample subjected to above-band-gap illumination and subsequent space charge formation.

Let´s assume a non-degenerate semiconductor with non-injecting contacts and that above-bandgap illumination is incident on its negatively charged transparent electrode. Light is then absorbed just below the surface (for CdZnTe ≈400-700 nm). The photo-generated electron-hole pairs are separated under applied voltage, while holes immediately recombine at the cathode and electrons drift through the semiconductor to the anode. Thus only the electron contribution to the total conductivity can be considered. Analogously to SCLC, we assume straight bands at the metal-semiconductor interface, consider one shallow trap, and neglect the concentration of free charge carriers' n_0 before illumination and diffusion currents. In contrast to SCLC model, both ohmic contacts are assumed to be non-injecting and

the boundary condition E(0)=0 can no longer be used. The solution of the quadratic equation (2.26) for the electric field E(x) then takes the form

$$\mathrm{E(x)} = -\sqrt{\mathrm{E^2(0)} + \frac{2\mathrm{jx}}{\epsilon_0 \epsilon_\mathrm{r} \theta \mu_\mathrm{e}}}. \tag{2.30}$$

Here j represents the current density, x spatial coordinate (x=0 corresponds to illuminated cathode and x=L corresponds to anode) and parameter θ is defined by the equation (2.4).

The boundary condition represented by the electric field just below the illuminated contact E(x=0) in equation (2.30) may be obtained by solving the balance equation describing the surface dynamic equilibrium between the incident light intensity I_l, surface recombination and drift into the bulk

$$\mathrm{I_l} - \mathrm{s_e n(0)} - \frac{\mathrm{j}}{\mathrm{e}} = 0. \tag{2.31}$$

Here s_e corresponds to the surface recombination velocity and n(0) to electron density under illuminated contact. Combining Ohm´s law and balance equation (2.31) yields in

$$\mathrm{E(0)} = -\frac{\mathrm{s_e j}}{\mu_\mathrm{e}(\mathrm{I_l e} - \mathrm{j})}. \tag{2.32}$$

The term connected to the direct or deep-level-mediated interband recombination in the sample's bulk was omitted in eq. (2.31) due to negligible dark currents. Since almost no free holes are present in the semiconductor volume, electrons cannot recombine there and we can assume infinite carrier lifetime τ_e. The trapped carriers are immediately de-trapped and the given trap is subsequently occupied by another carrier. The eq. (2.31) further assumes homogeneous surface irradiation, a constant rate of surface recombination, and that each photon generates exactly one electron-hole pair.

To have results consistent with generally used visualizations, we define the electric current as positive overall in the paper despite the negative electric field applied to the sample. Integrating equation (2.30) through the sample thickness L and using the boundary condition (2.32), we may express the applied voltage V dependent on j

$$V = \frac{\epsilon_0 \epsilon_r \mu_e \theta}{3j} \left\{ \left[\left(\frac{s_e j}{\mu_e (I_l e - j)} \right)^2 + \frac{2jL}{\epsilon_0 \epsilon_r \mu_e \theta} \right]^{\frac{3}{2}} - \left(\frac{s_e j}{\mu_e (I_l e - j)} \right)^3 \right\}. \quad (2.33)$$

The above dependence, further denoted as SCLP1, describes photocurrents limited by the space charge under the assumption of shallow traps and negligibly small dark currents. The disadvantage of the theory is that it gives an inverse dependence V=V(j) than the experiment and an analytical expression for the current density is not possible.

When the drift term (third term) in eq. (2.31) is much less than the other two ones, eq. (2.33) may be converted to eq. (2.29). Let us note that equation (2.33) involves the steady-state current and doesn´t contain any parameter defining the interaction of free electrons with the trap. Consequently, this model cannot be used for determining quantities defining electron trapping/de-trapping such as carrier capture cross-section, lifetime as well as the mobility-lifetime product. On comparing these findings with Many´s equation (2.20), it is evident that the application of eq. (2.29) to the steady-state experiment described by eq. (2.33) in the effort to determine $\mu_e\tau_e$ is unsupported.

A formula similar to equation (2.30) was also derived by du Chatenier [85]. The main difference between du Chatenier´s model and SCLP1 lies in the boundary condition represented by the electric field just below the illuminated contact E(x=0). Chatenier´s balance equation (2.31), which was used in the derivation of the boundary condition, depicts the surface recombination by the term n/τ_e. This term is connected to the direct or deep-level-mediated interband recombination defined by the electron lifetime τ_e. Because both holes and electrons are generated by above-band-gap light absorbed in the region close to the surface, recombination here is possible. However, the term n/τ_e neglects completely the spatial dependence of the hole distribution and τ_e. Especially it doesn´t take into account a larger concentration of photo-generated holes close to the surface as well as a higher defect density at the surface which both increase the recombination rate. Moreover, du Chatenier´s balance equation doesn´t consider the drain of free carriers to the contact. As a consequence of these omissions, the quantity τ_e appearing in du Chatenier´s model

has only the physical meaning of mean lifetime at the surface and it has no straight relation to the carrier lifetime in the bulk. Though it is noted in [85] that τ_e at the surface is considered, it is not accentuated there that τ_e cannot be used as the carrier lifetime in the bulk. The defining of the boundary condition with the help of the surface recombination s_e introduces a significant improvement in the SCLP1 model. In contrast to indeterminate τ_e, the parameter s_e corresponds to the well-defined quantity measurable by manifold techniques.

The SCLP1 model may be also easily generalized to a model of several shallow levels if their occupancy is ruled by the Boltzmann statistics. In such a case the parameter θ may be obtained as

$$\theta = \frac{n}{n + \sum_i n_{ti}}, \tag{2.34}$$

where the summation runs over respective level occupancies n_{ti} and other formulas remain unchanged.

2.5 Space-charge limited photocurrents 2

In the second model called SCLP2, we generalize the previous model SCLP1. In addition to SCLP1 considering only shallow levels, we generally assume the energy of deep trap levels located near the Fermi energy. To describe the occupancy of the deep trap level, the Fermi-Dirac statistics must be used instead of Boltzmann statistics. The concentration of trapped electrons may be expressed as

$$n_t = \frac{N_t}{1 + \exp\left[\frac{E_t - E_F}{k_B T}\right]} = \frac{N_t}{1 + \frac{n_1}{n}}, \tag{2.35}$$

where the parameter n_1 is related to the position of the trap level and is defined as

$$n_1 = N_c \exp[E_t/(k_B T)]. \tag{2.36}$$

For values of the parameter n_1 close to the initial concentration of free electrons n_0, the trap level is positioned close to the Fermi level. Conversely, for n_1 much larger or much smaller than n_0 we approach the previous model from section 2.4 with shallow traps. In addition, we also consider the substantial density of free electrons n_0 supplied by the ohmic cathode contributing to dark currents and trapped electrons, n_{t0}. The dark currents cannot be neglected especially in case of higher voltages, when

they reach in CZT samples approximately 40% of the total current. Using equations (2.22), and (2.35), the Gauss law may be used in the form

$$\frac{\mathrm{dE}}{\mathrm{dx}} = -\frac{\mathrm{e}}{\epsilon_0\epsilon_\mathrm{r}}\left[-\frac{\mathrm{j}}{\mathrm{e}\mu_\mathrm{e}\mathrm{E}} + \frac{\mathrm{N_t}}{1-\frac{\mathrm{n_1 e}\mu_\mathrm{e}\mathrm{E}}{\mathrm{j}}} - \mathrm{n_0} - \frac{\mathrm{N_t n_0}}{\mathrm{n_0}+\mathrm{n_1}}\right]. \tag{2.37}$$

By converting the bracket in eq. (2.37) to a common denominator, we get the second-order polynomial in E(x) in the numerator. If we mark E_1 and E_2 as the roots of the polynomial, eq. (2.37) then attains the form

$$\frac{\mathrm{E}\left(1-\frac{\mathrm{n_1 e}\mu_\mathrm{e}}{\mathrm{j}}E\right)}{(\mathrm{E}-\mathrm{E_1})(\mathrm{E}-\mathrm{E_2})}\mathrm{dE} = -\frac{1}{\epsilon_0\epsilon_\mathrm{r}\mu_e(n_0+n_1)}\mathrm{dx}. \tag{2.38}$$

Corresponding roots E_1 and E_2 are

$$\mathrm{E_{1,2}} = \frac{\mathrm{n_1}+\mathrm{N_t}-\mathrm{D} \pm \sqrt{(\mathrm{D}-\mathrm{n_1}-\mathrm{N_t})^2+4\mathrm{n_1 D}}}{-2\mathrm{AD}} \tag{2.39}$$

where parameters A and D are defined in (2.41). The semi-analytical SCLP2 model may be obtained by applying partial fraction decomposition to the integrand on the left side of eq. (2.38) followed by partial integration. The resulting transcendental equation for internal electric field, corresponding to SCLP2 model is

$$-\mathrm{A}[\mathrm{E(x)}-\mathrm{E(0)}] + \mathrm{B}\ln\left|\frac{\mathrm{E(x)}-\mathrm{E_1}}{\mathrm{E(0)}-\mathrm{E_1}}\right| + \mathrm{C}\ln\left|\frac{\mathrm{E(x)}-\mathrm{E_2}}{\mathrm{E(0)}-\mathrm{E_2}}\right| = \frac{\mathrm{e}}{\epsilon_0\epsilon_\mathrm{r}}\mathrm{ADx}. \tag{2.40}$$

Individual parameters A, B, C, and D, appearing in eq. (2.40) are following:

$$\mathrm{A} \equiv \frac{\mathrm{n_1 e}\mu_\mathrm{e}}{\mathrm{j}}, \qquad \mathrm{B} \equiv \frac{\mathrm{E_1}(1-\mathrm{AE_1})}{\mathrm{E_1}-\mathrm{E_2}},$$
$$\mathrm{C} \equiv \frac{\mathrm{E_2}(1-\mathrm{AE_2})}{\mathrm{E_2}-\mathrm{E_1}}, \quad \mathrm{D} \equiv \mathrm{n_0} + \frac{\mathrm{N_t n_0}}{\mathrm{n_0}+\mathrm{n_1}}. \tag{2.41}$$

The boundary condition for the SCLP2 model,

$$\mathrm{E(0)} = \frac{1}{2\mathrm{e}\mu_\mathrm{e}\mathrm{n_0}} \times \left[\mathrm{e}(\mathrm{I_l}+\mathrm{n_0 s_e}) - \mathrm{j} - \sqrt{4\mathrm{ejn_0 s_e} + (\mathrm{eI_l} - \mathrm{j} + \mathrm{en_0 s_e})^2}\right] \tag{2.42}$$

is attained from the balanced equation involving the dark current j_d and the dark concentration of free electrons n_0

$$I_l - s_e(n-n_0) - \frac{j-j_d}{e} = 0 \tag{2.43}$$

The dependence of the internal field E on the coordinate x cannot be expressed analytically. The electric field profile E(x) is calculated numerically for each x ∈ (0, L) and fixed trap parameters solving eq. (2.40) with given j, obtained from the experiment. The respective voltage V is acquired by the E(x) integration. The whole photocurrent-voltage dependency is obtained by repeating the procedure with different j. Similarly, as in the case of SCLP1, we see that SCLP2 does not involve any parameter defining (de)trapping or the carrier lifetime. Electrons may leave the sample only at contacts; by the surface recombination at the cathode and by drain at the anode.

2.6 Drift-diffusion model

Analytical models SCLP1 and SCLP2 are based on a significant simplification, which could make them useless in general conditions and render the obtained results inaccurate. Especially neglected is the contribution of holes, which may affect the transport characteristics in the high resistivity n-type samples and even more markedly in p-types. The involvement of holes in the calculations disables the utilization of an analytical approach and fully numerical treatment must be engaged. We adopted for this purpose previous codes for the simulation of transient currents solving in parallel drift-diffusion and Poisson's equations in a material with traps [49]. In addition, we refined the boundary condition defining the interface carrier density by involving an interface layer that supressed the surface recombination. Instead of fixed free carrier density directly defined by the metal-semiconductor Schottky barrier we use a dynamical prescription according to [86], [87] and define the free carrier current at the electrodes in the form

$$\begin{aligned} J_e(0) &= -\gamma_e^{(0)} e\left[n_0^{(0)} - n(0)\right], \\ J_h(0) &= \gamma_h^{(0)} e\left[p_0^{(0)} - p(0)\right], \\ J_e(L) &= \gamma_e^{(L)} e\left[n_0^{(L)} - n(L)\right], \\ J_h(L) &= -\gamma_h^{(L)} e\left[p_0^{(L)} - p(L)\right], \end{aligned} \tag{2.44}$$

where $J_{e(h)}(0)$, n_0 $(p_0)^{(0)}$, $J_{e(h)}(L)$, and n_0 $(p_0)^{(L)}$ are the equilibrium electron (hole) current density and dark density of electrons and holes at the cathode (x=0) and

anode (x=L), respectively. Respective γ-factors define the transfer rate through the interface. In addition to [86], and [87], where only limiting cases γ = 0 and γ = ∞ were considered, we use a general γ in the fit of experimental data. Let us note that $n_0(p_0)$ may be different at the cathode and the anode due to possibly unlike band banding at the interfaces.

The improvement of the contact model is indispensable for the right description of the current in a biased sample and the surface recombination at the illumination. The case with γ = 0 suppresses the surface recombination by the drain of the respective carrier to the contact. Simultaneously, it completely disables electric current. Conversely, γ = ∞ induces a large surface recombination of carriers excited by the above-band-gap light in the thin layer < 1μm below the semi-transparent contact. We apply the contact model defining the interface transfer of carriers by the linear functions of the carrier density (2.44) for a description of basic properties of the current-carrying illuminated interface with a general value of the γ-factor.

Drift-diffusion electron and hole equations [49] involving carriers (de)trapping on defect levels described by the Shockley-Read-Hall model were numerically time-integrated. Adaptive Step-size Control of the fourth-order Runge-Kutta method was used for integration. Electrostatic potential and the electric field profile were calculated by solving Poisson's equation at each integration step. The simulation of the steady-state and chopped photoconductivity occurring in the period significantly exceeding the drift time or lifetime of free carriers is done with electrons and holes in a steady-state distribution. This simplification does not notably disturb the obtained results but it significantly speeds up the calculation and allows us to make simulations in a reasonably short time period without putting big demands on the computational resources [49].

The analytical model described in this section will be further marked as the Drift-diffusion model (DDF).

3. Experimental methods

3.1 Laser-induced transient current technique

The laser-induced transient current technique (LTCT) represents, nowadays, a prospective tool for how to non-destructively investigate the bulk properties of semi-insulating materials. It belongs to the group of Time of flight measurements, which were first introduced by Haynes and Schockley [88]. Several sources may be generally used in Time of flight measurements for charge carrier generation, such as X-rays, alpha particles, electrons, or protons, while LTCT particularly uses laser pulses. The advantage of LTCT is the possibility of using oscilloscope triggering bounded directly to the excitation laser pulses which improves signal-to-noise ratio compared to methods with non-synchronized excitation sources. Moreover, an easily tuneable intensity of laser pulses ensures a negligible plasma effect [89], [90] which is created under excessive charge carrier generation and distorts the right data evaluation by screening of applied electric field.

Charge carrier mobility, mobility-lifetime product, and transit time, which is the time taken by charge carriers to travel across a given region of the sample under the influence of a known electric field, are the most frequently measured quantities by LTCT. Other features such as surface recombination velocity, internal electric field, and space charge profile along the sample thickness can be evaluated, by a detailed analysis as well. The main difference compared to steady-state photocurrent measurements is the use of the pulsed radiation source, instead of a continuous illumination.

3.1.1 Principle of laser-induced transient current technique

Assume that we illuminate the cathode side of a planar sample by above-bandgap light, as shown in schematic Fig. 2. Then electron-hole pairs are generated in the near vicinity of the irradiated contact. In case of sufficiently weak irradiation intensity, the light serves only as a probe for material characterization and does not influence the material properties. Under applied bias, holes are almost immediately swept at the

cathode, while photo-generated electrons drift toward the opposite electrode through the sample thickness *L*. According to the Ramo theorem [91], electrons induce by their movement a current transient signal which can be further recorded by an oscilloscope. Analogously, a solely hole signal can be recorded by simply reversing the applied voltage polarity or by irradiating the opposite contact. The possibility of electron and hole signal separation is an important advantage of LTCT measurement [89].

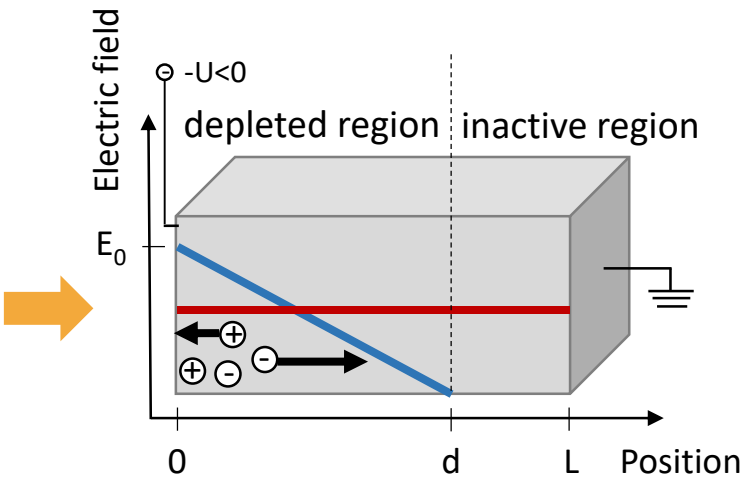

Fig. 2: Scheme of the LTCT. Red and blue lines represent the linear profile of the electric fields in a detector. Blue line profile corresponds to the positive accumulated charge.

In the simplest case of a homogenous electric field, the charge carrier mobility μ is given by the relation

$$\mu = \frac{L^2}{V t_r}, \tag{3.1}$$

as follows from the eq. (2.5) and eq. E = V/ L where *V* is applied bias, *L* sample thickness, and t_r transit time. The amplitude of the current pulse *I(t)* induced by number *n* of carriers drifting across the sample is in ideal case given as [92]

$$\begin{aligned} I(t) &= \frac{ne}{t_r} \qquad 0 \le t \le t_r \\ I(t) &= 0 \qquad\quad t \ge t_r. \end{aligned} \tag{3.2}$$

In real devices, the shape of current waveforms (CWFs), however, differs from the ideal case, given by the equation (3.2), as seen in Fig. 3. Among several phenomena affecting CWF in real devices, the following phenomena are most crucial [92]:

i. inhomogeneous internal electric field distribution within the sample. This is especially typical for Schottky or p-n junction
ii. high density of photo-generated carriers leading to space charge-related effects. Charge carriers can shield the internal electric field
iii. trapping and de-trapping at shallow levels
iv. presence of thermal diffusion
v. surface recombination

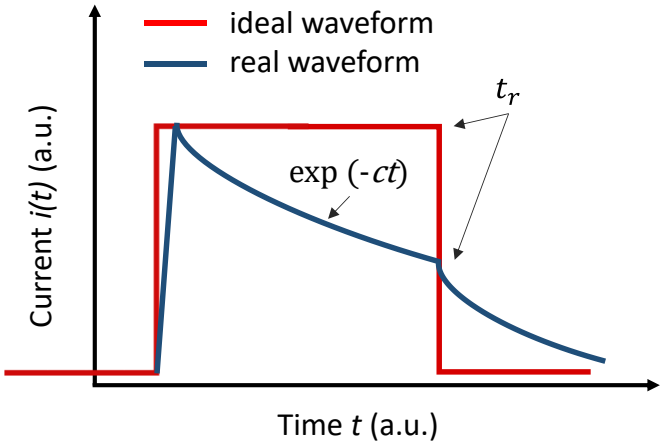

Fig. 3: Transient current waveforms induced by drifting carriers through the sample. An ideal current waveform is depicted by a red line and a typical current waveform is by a blue line.

3.1.2 Theory of laser-induced transient current technique

For simplicity, let´s assume constant mobility μ_e and constant space charge density ρ_{SC}. The last consideration is well fulfilled in CZT radiation detectors as was previously shown in [89], [93], [94]. Poisson equation then gives a linear dependence of an internal electric field on the distance x from the irradiated electrode:

$$E(x) = E_0 - ax \geq 0 \tag{3.3}$$

where *a* represents the linear slope of the electric field and E_0 is an electric field under the irradiated electrode. The slope of the electric field depends on the sample and contacts quality and is related to the space-charge density N as:

$$a = \frac{eN}{\varepsilon_0 \varepsilon_r} \tag{3.4}$$

where ε_0, ε_r are the vacuum and relative permittivity, respectively. Definition (3.3) guarantees that the electric field E(x) is always non-negative, regardless of the polarity of the applied voltage, the type of collected charge carriers, and the polarity of the space charge. It also takes into account that the formation of a space charge can create an inactive layer with zero electric field under the contact as seen in Fig. 2.

As the carriers generated under the cathode drift to the opposite electrode, some of them are lost due to trapping on trap levels inside the band gap. Considering the loss of carriers due to trapping and by neglecting the possibility of their subsequent release from traps (de-trapping), the transient current can be expressed by an exponential decrease [95]:

$$i(t) \sim e^{-ct}. \tag{3.5}$$

Here the parameter c, given as

$$c = \left(a + \frac{1}{\mu_e \tau_e}\right) \mu_e, \tag{3.6}$$

can be obtained by fitting an exponential decrease of transient currents prior to transit time (Fig. 3). Two situations can occur depending on the value of the slope *a*:

a) $d = L$; the inactive region with zero electric field does not exist within the entire volume of the sample (see red line in Fig. 2). In this case, a transient current signal shows a clear drop, corresponding to the transient time t_r, which occurs when the most of generated electrons reach the opposite anode (see Fig. 3). From knowledge of parameters c, t_r, and $\mu_e \tau_e$, obtained from experiment, the slope of internal electric field, can be numerically solved from the following transcendental equation [89]:

$$ct_r = \left(1 + \frac{1}{a\mu_e \tau_e}\right) \ln\left(\frac{1 + \frac{aL^2}{2V}}{1 - \frac{aL^2}{2V}}\right). \tag{3.7}$$

b) $d < L$; the internal electric field reaches zero value at the distance d from the cathode (see blue line in Fig. 2). In such case t_r is undefined and determination of further charge carrier transport parameters, including internal electric field profile is not possible. Thanks to the independence of μ_e on bias, the μ_e may be obtained from the TCT experiment with higher applied bias when the inactive zone no longer exists. Using obtained μ_e, equations (3.6) and (3.7), one may calculate the linear slope of the electric field.

3.1.3 Transient currents in case of inhomogeneous space charge distribution

For inhomogeneous space charge density induced by injecting contacts or by above-band-gap illumination we have to deal with equations (2.30), and (2.32) defining the internal electric field. According to the Ramo theorem [91], the CWF induced by charge Q moving with velocity v through a planar sample of thickness L can be generally expressed as [89]

$$i(t) = \frac{Q(t)v(t)}{L}. \tag{3.8}$$

The trajectory of an electron excited at the cathode is easily calculated by integrating the kinetic equation $dx/dt = -\mu_e E(x)$, in which E(x), E(0) defined by equations (2.30), (2.32) are used

$$x(t) = \frac{\epsilon_0 \epsilon_r \mu_e \theta}{2j} \left[\left(\frac{jt}{\epsilon_0 \epsilon_r \theta} - E(0) \right)^2 - E^2(0) \right]. \tag{3.9}$$

Time derivation and substituting into (3.8) finally leads to CWF in the form

$$i(t) = \frac{Q(t)\mu_e}{L} \left(\frac{jt}{\epsilon_0 \epsilon_r \theta} - E(0) \right). \tag{3.10}$$

In the case of a good-quality sample, when the carrier lifetime significantly exceeds the transit time, we may consider time-independent $Q(t) = Q_0$, and i(t) attains a linear shape. As it results from equation (3.10), increasing transient current confirms the presence of a negative space charge in the detector, while the decreasing current shape after the onset corresponds to a positive space charge.

3.1.4 Charge collection efficiency determined by L-TCT

Charge collection efficiency, CCE, is an important quantity, which can be measured by L-TCT and used to determine mobility-lifetime product. In the case of a constant electric field, CCE follows the Hecht equation [96]:

$$\mathrm{CCE} = \frac{\mathrm{Q_m}}{\mathrm{Q_0}} = \left\{\frac{\mu_h \tau_h \mathrm{E}}{\mathrm{L}}\left[1 - \exp\left(-\frac{\mathrm{x_i}}{\mu_h \tau_h \mathrm{E}}\right)\right] + \frac{\mu_e \tau_e \mathrm{E}}{\mathrm{L}}\left[1 - \exp\left(\frac{\mathrm{x_i} - \mathrm{L}}{\mu_e \tau_e \mathrm{E}}\right)\right]\right\}, \tag{3.11}$$

where Q_m is the collected charge, Q_0 is the photo-generated charge, $\mu_{h,e}$ is the mobility of holes/ electrons, $\tau_{h,e}$ is the lifetime of holes/electrons, E is the electric field intensity, L is the width of the sample and x_i corresponds to the position inside the sample where the incident light is absorbed.

If the electron-hole pairs are generated in a near vicinity of the irradiated cathode, which can be a case of above-bandgap light or α particle absorption, the x_i can be set as zero and the Hecht equation (3.11) can be simplified as:

$$\mathrm{CCE} = \frac{\mu_e \tau_e \mathrm{V}}{\mathrm{L}^2}\left[1 - \exp\left(\frac{-\mathrm{L}^2}{\mu_e \tau_e \mathrm{V}}\right)\right]. \tag{3.12}$$

By fitting the CCE dependency on the applied bias V using (3.12) for a given width of the sample, one can obtain the μτ product. Mobility-lifetime product may be also determined via the Hecht equation from α-TCT measurement, where alpha particle excitation is used instead of above-bandgap illumination. The plasma effect combined with an indistinct oscilloscope trigger due to a non-synchronised α-source, however, leads to a lower accuracy in the evaluated mobility (an estimated error is 3%). In contrast, excitation using above-bandgap light is absorbed closer to the surface, within the depth of a few hundred nm (~0.36 μm in the case of CZT). As a consequence, surface-related processes, such as surface photo-voltage and surface recombination may distort the determined μτ product. These effects are involved in a modified Hecht equation, according to (2.20) [97]

$$\mathrm{CCE} = \frac{\mathrm{Q}}{Q_0} = \frac{1}{1 + \frac{s_e L}{\mu_e V}} \frac{\mu_e \tau_e \mathrm{V}}{\mathrm{L}^2}\left[1 - \exp\left(\frac{-\mathrm{L}^2}{\mu_e \tau_e \mathrm{V}}\right)\right]. \tag{3.13}$$

Moreover, electronics used in the signal processing in L-TCT affect the shape of measured CWF, and therefore a deconvolution is necessary.

3.1.5 TCT experimental set-up

3.1.5.1 L-TCT measurement under DC bias

Laser-induced transient currents using DC voltage are excited from the cathode side by probing laser pulses with 2 ns width, 100 Hz repetition frequency, and above-bandgap wavelength (Fig. 4).

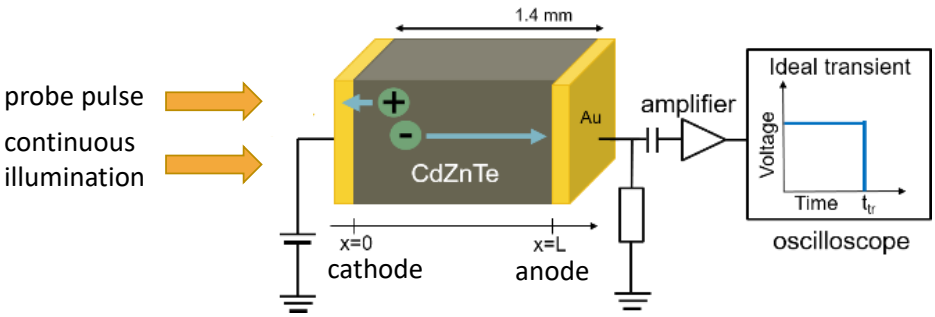

Fig. 4: L-TCT experimental setup with illumination from cathode side by probe laser pulses. Continuous illumination may be optionally used to study the influence of space charge.

The wavelengths of 662 nm and 514 nm were used in the case of measurements on CdZnTe and MAPI, respectively. Acquired CWFs are amplified by a high-frequency bipolar 3-GHz Miteq AM-1607-3000R amplifier, with a signal conversion of 6.85 mV/μA into a voltage pulse, and then are recorded using a 4-GHz digital LeCroy oscilloscope on the 50 Ω dc input resistance [98]. In all measurements, we chose such intensity and repetition frequency of probe laser pulses that the plasma effect [94] was negligible and laser pulses did not influence CWF shape. The experimental setup is shown in Fig. 5.

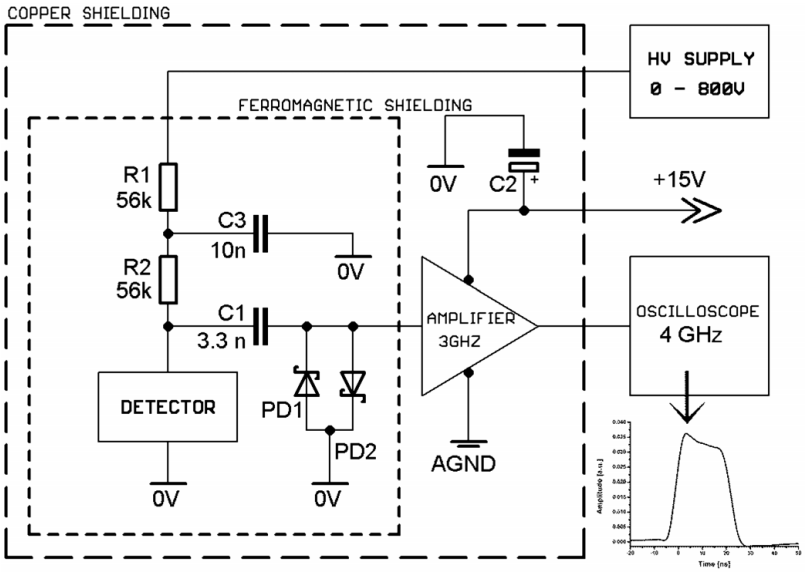

Fig. 5: Detailed transient current experimental setup with a typical transient current output pulse in the inset graph

To investigate the influence of space charge, L-TCT was measured not only in the dark by weak probe laser pulses, but also under additional continuous above bandgap illumination (see Fig. 4). For continuous illumination of the cathode, we used LED of 690 nm wavelength and 4 $\mu W.cm^{-2}$ intensity.

3.1.5.2 L-TCT measurement under pulsed bias

We used a pulsed bias regime of L-TCT to prevent ion migration in perovskite samples. The pulsing bias parameters, such as bias amplitude, bias width, period, and delay time, representing the time between the rising edges of the applied voltage pulse and the probing laser pulse, are shown in Fig. 6. Unless otherwise stated, used bias pulse has a frequency of 5 Hz, width of 1 ms and the 100 µs delay time between the bias onset and laser probe pulse was used.

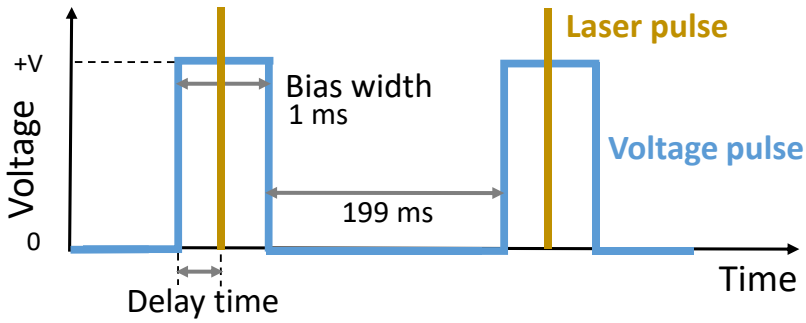

Fig. 6: The scheme of applied bias pulse (green line) and the probe laser pulse (yellow line) to the perovskite sample used during L-TCT measurements.

After applying a bias pulse to the perovskite sample a RLC phenomenon occurs in the circuit, thanks to the sample capacity of 2 pF and resistance of 58.5 MΩ. The voltage evolution recorded on the oscilloscope after applying a bias pulse is purely connected with the RLC phenomenon, as can be seen in Fig. 7, where we compare dark current responses of the perovskite sample and phantom sample to the 1 ms applied bias pulse of 80 V. The used phantom consists of a capacitor with capacity 2 pF and resistor with resistance of 50 MΩ. Recorded dark current responses of perovskite and phantom samples to applied bias pulse are almost the same, while only small deviations arise from small variations in capacity and resistance. The presented L-TCT waveforms in section 5 were obtained by subtracting the dark current response at a given bias pulse from the current response recorded after applying simultaneously bias pulse and laser pulse with a given delay time.

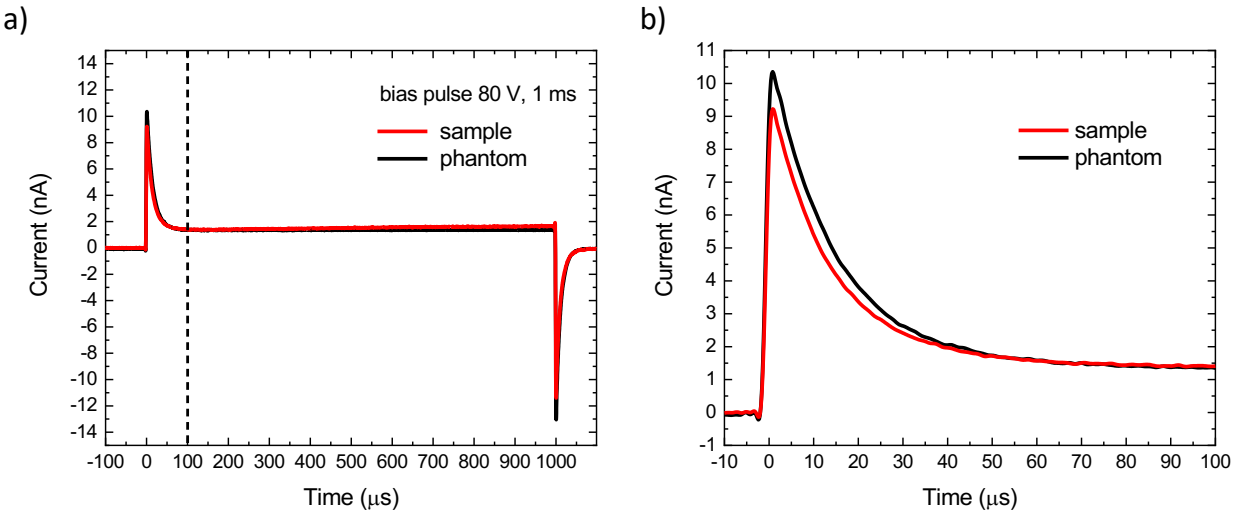

Fig. 7: a) Dark current response of perovskite sample after applying a 1 ms bias pulse of 80 V, compared to dark current response of phantom sample, consisting of 2 pF capacitor and 50 MΩ resistor. The dashed line marks the time when the L-TCT current waveform was measured. b) Detail of dark current responses.

3.2 Photocurrent-voltage characteristics

Photocurrent-voltage (PV) characteristics of CdZnTe crystals under continuous illumination are measured by a laser diode powered by a Tektronix AFG 3252 arbitrary waveform generator. The wavelength of incident light is 690 nm (hν ≈1.87 eV) with an intensity of 4 μW/cm^2. A homogeneously irradiated area of

3 mm^2 is used as a compromise between homogenous illumination of the whole sample and an effort not to illuminate the edges of the sample to avoid extra leakage current. A smaller illumination spot could lead to lateral broadening of the current due to diffusion, and the one-dimensional (1D) approximation used in our theoretical models may not be sufficient. To probe local properties with a small illumination spot, one should use a three-dimensional model instead of a 1D approximation. Current through the sample is measured indirectly on a 1 MΩ load resistor. Since we irradiate the cathode side of the samples with above-band-gap light, only electrons contribute to the measured signal. The final photocurrent in CdZnTe at a certain DC bias is determined as the difference between the current under illumination and dark current. In this way, the leakage current is extracted from the measurements and does not influence the presented data. The dark currents in CdZnTe samples show after applying a DC bias a bi-exponential decay that lasts several minutes until the values stabilize [99]. The initial steep decline of the dark currents probably occurs as a consequence of bias-induced shallow trap de-trapping while the later slower decline may be attributed to the de-trapping of deep levels. Therefore, dark currents were recorded after a certain time, which was necessary for their stabilization.

PV characteristics of perovskite single crystals were measured in a pulsed bias regime while the parameters of the used bias pulse were the same as in the case of L-TCT measurement (see Fig. 6). We first recorded by oscilloscope a dark current response to bias pulse (Fig. 7) and then current response under anode continuous LD illumination with the above-bandgap wavelength of 465 nm and intensity of 450 $\mu W.cm^{-2}$. The presented photocurrents in section 5 were obtained by subtracting the dark current response and current response under continuous illumination at the time of 6 µs. The time 6 µs is short enough that memory effects, visible mainly at the end of the applied bias pulse, do not distort the evaluated photocurrent.

3.3 Fourier-transform photocurrent spectroscopy

The Fourier-transform photocurrent spectroscopy (FTPS) represents a fast and highly sensitive method to probe the deep defect levels in semiconducting materials. The foundations of FTPS were first laid in 1997 [100] and later by work [101]. The basis of the method lies in the replacement of the monochromator with

an FTIR (Fourier Transform Infrared) spectrophotometer, which allows to measure all the wavelengths at the same moment. Light of a given wavelength is not physically isolated during measurement but only labelled. The photocurrent spectral distribution is subsequently obtained after mathematic decoding. The measured FTPS signal is given by photo-carriers (both electrons and holes) generated in the absorber and subsequently collected by the external electrodes under applied or built-in bias. Photocurrent spectra are very complex as various factors may interfere in resulting spectra, such as lifetime and mobility distribution, influence of deep and shallow defects, material morphology, optical absorption coefficient, refraction index, distribution of generated free carriers, etc.

An advantage of Fourier transform spectrometers working as the light source is two orders higher light power due to an absence of an entrance slit compared to dispersive spectrometers, such as monochromators. Simultaneous processing over the whole frequency domain improves the measurement speed and also the signal-to-noise ratio. On the contrary, a problematic feature of FTPS lies in the necessity of electrical contact preparation. The method is restricted only to semiconductors, while conductors and insulators cannot be measured. The method has been, however, successfully applied to non-crystalline semiconductors, such as amorphous silicon [102], [103].

3.3.1 Principle of Fourier-transform interferometer

The most common Fourier-Transform spectrometers are based on Michelson's interferometer, which consists of a light source, a beam splitter, two mirrors set at right angles, and a detector (see Fig. 8). The light approaches the beam splitter at an angle of incidence of 45 degrees and is partly transmitted and partly reflected into two beams of approximately equal intensity. The reflected beam 1 and transmitted beam 2 are incident at normal incidence to mirror 1 and mirror 2. After their reflection on the mirrors and passing beam splitter both beams superpose at the detector and produce an interference pattern.

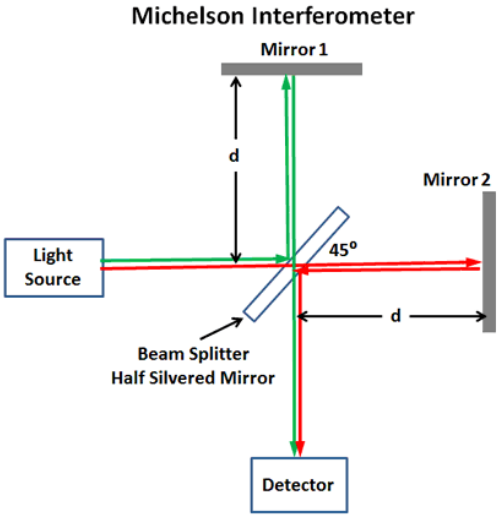

Fig. 8: The principle of Michelson´s interferometer.

In the case of a Fourier transform spectrometer, one of the mirrors is additionally movable compared to the Michelson interferometer. Suppose one mirror moves linearly with velocity u, then the optical path difference, referred also as retardation, is given as $\Delta = u(t - t_0)$. The dependence of the intensity of superposed light *I* on time (or mirror position) is known as an interferogram. To obtain an interferogram, the detector signal is recorded as a function of retardation, by making measurements of the signal at many discrete positions of the moving mirror. The interferogram intensity for a monochromatic source changes in time *t* as the cosine function [104]

$$I(\Delta) = \frac{1}{2} I_0[1 + \cos(2\pi\sigma\Delta)]. \tag{3.14}$$

Here Δ is retardation, σ is the wavenumber which is defined as the inverse of the wavelength λ and I_0 is the intensity at zero retardation $\Delta = 0$. For a polychromatic light source with the spectral intensity of the light source $I(\sigma)$, the total intensity of superposed light $I(\Delta)$ can be obtained as a superposition of sinusoidal waves for light at all wavenumbers σ [104]

$$I(\Delta) = \frac{1}{2} \int_0^\infty I(\sigma)\,[1 + \cos(2\pi\sigma\Delta)]\mathrm{d}\sigma. \tag{3.15}$$

The overall signal in eq. (3.15) is given by the sum of a constant, or “DC” part, and an alternating, or “AC” part

$$I_{DC}(\Delta) = \frac{1}{2}\int_0^\infty \mathrm{I}(\sigma)\,\mathrm{d}\sigma = \mathrm{I}_0,$$
$$I_{AC}(\Delta) = \frac{1}{2}\int_0^\infty \mathrm{I}(\sigma)\cos(2\pi\sigma\Delta)\,\mathrm{d}\sigma. \tag{3.16}$$

Since the DC part is not registered by the Fourier analysis, let´s further consider only an AC part. Considering that $\mathrm{I}(\sigma)$ is a real even function, the overall signal at the detector may be expressed by adding the imaginary odd part given by the sine function which will vanish after the integral

$$I(\Delta) = \tfrac{1}{2}\textstyle\int_{-\infty}^{\infty} \mathrm{I}(\sigma)\,[\cos(2\pi\sigma\Delta) + i\sin((2\pi\sigma\Delta))]\mathrm{d}\sigma. \tag{3.17}$$

By applying Euler´s equation to eq. (3.17), the interferogram may be written as

$$I(\Delta) = \frac{1}{2}\int_{-\infty}^{\infty} I(\sigma)\, e^{i\pi\sigma\Delta}\, d\sigma. \tag{3.18}$$

Eq. (3.18) implies that the intensity $\mathrm{I}(\Delta)$ of the recombined beam as a function of the retardation is the Fourier transform of the intensity of the light source *I(σ),* as a function of the wavenumber. The name Fourier transform spectrometer originates therefore in the relationship $\mathrm{I}(\Delta) = \mathrm{F}\{\mathrm{I}(\sigma)\}$. The intensity as a function of wavenumber *I(σ)* can be thus obtained from the measured interferogram by an inverse Fourier transformation

$$I(\sigma) = 2\int_{-\infty}^{\infty} I(\Delta)\, e^{-i\pi\sigma\Delta}\, d\Delta. \tag{3.19}$$

The interferogram of ideal monochromatic light compared to the interferogram of non-ideal monochromatic or polychromatic light is shown in Fig. 9a). Due to the finite coherence of non-ideal monochromatic or polychromatic light, the visibility of the interference is reduced for longer delay times, as there is no correlation between the peaks of the first interfering wave and the second time-delayed version at longer times. Interference is sometimes constructive and sometimes destructive.

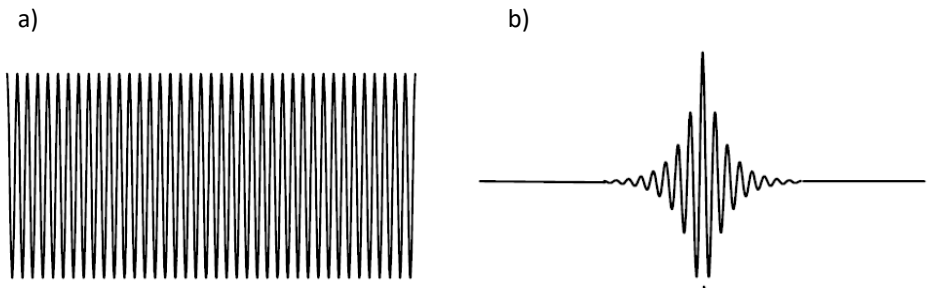

Fig. 9*:* The interferogram of a) an ideal monochromatic light with delta-function spectral distribution and of b) non-ideal monochromatic or polychromatic light.

In the case of photocurrent measurements, the FT interferometer is used as a source of incident light to the measured sample which is outside of the FT interferometer. Here, the measured sample directly serves as an external detector. The interferogram is not recorded for an infinite retardation Δ, as suggested in equation (3.19), but there is a finite retardation *L*. This can be equivalently written in a way that the interferogram is truncated by the unit rectangular window function $\prod$, describing the interval [-L, +L] of mirror motion

$$I(\sigma) = 2\int_{-\infty}^{\infty} \prod\left(\frac{\Delta}{2L}\right) I(\Delta)\, e^{-i\pi\sigma\Delta}\, d\Delta. \tag{3.20}$$

As the Fourier transform of a rectangular function is a sinc function, the real spectrum is convolved with an instrument resolution function $sinc\,(2L\sigma)$. The spectral resolution of the FT interferometer then depends on the maximum distance *L* of the movable mirror

$$\delta\sigma = \frac{1}{2L}. \tag{3.21}$$

3.3.2 FTPS experiment

The basic FTPS set-up consists of an FTIR spectrophotometer, low-noise current preamplifier, appropriate optical filters, sample holder, external focusing mirror, external A/D converter, and external light source, as can be seen in Fig. 10.

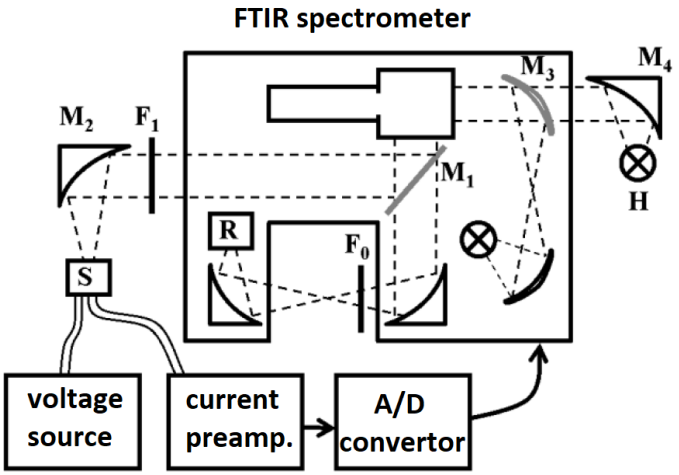

Fig. 10: FTPS setup. Here S stands for sample, M_1 is moving mirror, M_3 rotating mirror, M_2 and M_4 external focusing mirrors, F_0, F_1 filters and H external light source. R is reference measured without sample and with filter F_0.

FTPS measurement records more interferogram scans to increase the signal-to-noise ratio, while usually few hundred scans are necessary. Individual scans are corrected for the phase and summed together. The time necessary to record one scan depends on mirror velocity and maximal retardation. For example, one scan with a typical mirror velocity of 0.16 cm/s and resolution of 32 cm^{-1} takes ~ 1 s.

Here, the FTPS measurements were performed with a Thermo Nicolet 8700 Fourier-Transform Infrared spectrometer from Thermo Scientific equipped with an 80 W external halogen light source from NARVA. Used FTIR has a thermoelectrically cooled deuterated triglycin sulfate pyro-detector, quartz beam-splitter, spacing of 0.5, and mirror velocity of 0.1581 cm/s. For solar cells, an SR570 current preamplifier from Stanford Research Systems was used in low noise mode with 10 µA V^{-1} – 200 nA V^{-1} pre-amplification and no external voltage was applied to the devices. The spectral range was divided into three partly overlapping measurements separated by long-pass colour filters to extend the dynamic range. The first measurement was made using only a mesh filter to reduce the illumination intensity 30 times. The following two measurements were performed with long-pass glass filters from Quantum Design at cut-off wavelengths of 780 nm and 800 nm. All measurements were taken in a cryostat with optical windows in a nitrogen atmosphere at room temperature to minimize degradation due to humidity and oxygen [105].

The measured perovskite samples were prepared in two ways:

a) Thin films on a transparent substrate with two parallel contacts on the top of the measured sample with a spacing of 1 mm. To measure FTPS an external bias of 60 V was applied.
b) Solar cells. These may be measured without any applied external voltage as separation and subsequent collection of photo-generated carriers is driven by selective electron and hole transport layers.

3.4 Other experimental methods

3.4.1 Photothermal deflection spectroscopy

Upon the absorption of incident light by a studied semiconductor, a part of or all excitation energy is transformed into thermal energy. This principle is used in the Photothermal deflection spectroscopy (PDS). The measured sample, placed in a cuvette, is immersed in a transparent liquid whose refraction index strongly depends on temperature. The heat generated by sample light absorption increases also the temperature in a thin layer of liquid that is adjacent to the sample surface. When a second probe beam, parallel to the sample surface, passes through this region with an absorption-induced gradient of refraction index, it is deflected. The angular deflection is recorded by a four-quadrant photodiode and may be related to the optical absorption of the sample.

The used PDS setup records simultaneously transmittance, reflectance, and absorptance spectra of the measured sample, while the sensitivity of absorptance measurement ranges in four orders of magnitude. Fluorinert FC72 was used as a liquid with refraction index dependency. A monochromator equipped with a 150 W xenon lamp and a mechanical chopper at a frequency of 12 Hz was used as a light source with a spectral range of 250-1700 nm. A lock-in amplifier referenced to the chopper frequency was used to record the signal which was further normalized to the incident light intensity by a spectrally calibrated detector. The optical absorptance was normalized on the absorptance of the black sample.

3.4.2 Photoluminescence spectra measurements

Photoluminescence (PL) measurements were performed by using a Cary Eclipse Fluorescent Spectrophotometer from Agilent with an additional xenon lamp adjusted

for one-sun illumination for the light-soaking process. Samples were kept in the DN2 cryostat chamber from Oxford Instruments equipped with electrical contacts and filled with nitrogen at room temperature to minimize the effect of ambient air atmosphere. The excitation wavelength was set to 440 nm and the PL signal was collected in the range of 550 – 950 nm.

3.4.3 X-ray diffraction measurements

The powder patterns were collected using a Rigaku Smartlab diffractometer equipped with a rotating 9kW Cu anode, primary and secondary Soller slits (5 deg), and a 1D detector. The measurements were carried out in Bragg-Brentano geometry using Johansson primary Kα1 monochromator (λ = 0.15406 nm). To avoid the degradation of the perovskite layer in the ambient air, the new pristine sample was cut into several pieces and they were separately stored and illuminated in a capsule filled with nitrogen before the experiment in an ambient atmosphere. Immediately after illumination, the sample was aligned in the diffractometer and measured. To ensure that the collected powder pattern is not affected by the sample degradation, the diffraction peaks at 28.2 deg and 32.3 deg were measured in static mode (5 min) before and after the main data collection by Bragg-Brentano θ-2θ scan (30 min).

3.5 Sample preparation

3.5.1 CdZnTe planar detectors

$Cd_{0.85}Zn_{0.15}Te$ of n-type conductivity was fabricated by EV Products using the High-Pressure Bridgman Growth method. The obtained multigrain wafer was further processed with a 600-grit SiC abrasive to highlight the boundaries of the individual grains. Square-shaped monocrystalline samples of dimensions $5 \times 5 \times 2$ mm^3 were cut from wafers with a wire saw. To remove surface damage, the individual sides of the samples were roughly polished with SiC abrasive 1000 and then finely with SiC abrasive 1200. Further improvement of the surface properties was achieved by 2 min chemical etching of the samples in a 3% solution of bromine in methanol. Samples were subsequently rinsed in methanol. Before preparing metal contacts, all surfaces except the two largest opposite surfaces were covered with photoresist and left in the oven at 60 °C for a few minutes. The entire sample was immersed in a 1% $AuCl_3$ aqueous solution for one minute, causing gold to precipitate on the areas not covered

with photoresist. The samples were cleaned in distilled water from an $AuCl_3$ solution and the photoresist was removed in an acetone bath. The planar detector was then glued with photoresist to a non-conductive holder with the gold contacts. The sample and holder contacts were connected by silver wires using graphite paste. The average specific electrical resistance of measured samples, determined from the VA characteristics, is 2.7×10^{10} Ω·cm.

3.5.2 Materials used in perovskite fabrication

Lead iodide (PbI_2) was purchased from TCI Chemicals. Titanium diisopropoxide bis(acetylacetonate) (75 wt% in isopropanol), formamidium iodide (FAI), cesium iodide (CsI), lead bromide ($PbBr_2$), acetonitrile, lithium bis(trifluoromethanesulfonyl) imide (Li-TFSI), chlorobenzene, N,N-dimethylformamide (DMF), dimethyl sulfoxide (DMSO), 4-tert-butyl pyridine, were purchased from Sigma-Aldrich. Titanium dioxide paste (30 NRD) was purchased from Greatcellsolar and 2,2′,7,7′-tetrakis[N,Ndi-(4-methoxyphenyl)amino]-9,9′-spirobifluorene (spiro-MeOTAD) was purchased from Lumtec. All the chemicals were used as received without further purification. Perovskite thin films were deposited on pre-patterned fluorine-doped tin oxide (FTO) coated glass substrates (10 Ω sq^{-1}), purchased from Solaronix.

3.5.3 Perovskite single crystal preparation

MAPI and MAPB single crystals were synthetized by inverse temperature crystallization (ITC) method with N,N-Dimethylformamide (DMF) solution as solvent [106]–[108]. Gold contacts were deposited by thermal evaporation onto both largest sides of the sample with dimensions 4x4x2 mm^3, similarly as in the case of CdZnTe.

3.5.4 Perovskite solar cell preparation

Solar cells were prepared on fluorine-doped tin oxide (FTO) substrates, on which 30 nm-thick compact TiO_2 was deposited as the electron transport layer (ETL) by spray pyrolysis at 450 °C. Substrates were then sintered at 500 °C for 30 min and left to cool down slowly to room temperature. A 150 nm thick mesoporous TiO_2 layer was deposited by spin coating at 4000 rpm for 20 s using a diluted 30 nm TiO_2 nanoparticle paste in anhydrous ethanol. After spin coating, the substrates were

immediately dried on a hot plate at 100 °C for 10 min and then sintered at 500 °C for 60 min. The perovskite films were deposited from a precursor solution which was prepared by dissolving FAI (0.143 g), CsI (0.044 g), PbI_2 (0.184 g), $PbBr_2$ (0.220 g) in 1×10^{-3} L of solvent of DMF: DMSO = 4: 1 under constant stirring at 70 °C. The perovskite solution was spin-coated on the substrate at 1000 rpm for 10 s and 5000 rpm for 30 s. The antisolvent, chlorobenzene (150×10^{-6} L), was dropped on the spinning substrate 10 s before the end of the second step. The samples were subsequently annealed at 100 °C for 30 min in a nitrogen-filled glovebox. The hole transport layer (HTL) layer was prepared by spin-coating 50×10^{-6} L of a spiro-MeOTAD solution at 4000 rpm for 30 s on top of the perovskite layer. The spiro-MeOTAD solution was prepared by dissolving 2,2′,7,7′-tetrakis[N,Ndi-(4-methoxyphenyl)amino]-9,9′-spirobifluorene in chlorobenzene (72.3 g L^{-1}) with the addition of 28.8×10^{-6} L of 4-tert-butyl pyridine and 17.5×10^{-6} L of Li-TFSI solution in 1×10^{-3} L of acetonitrile. Finally, the 80 nm-thick Au top electrode was thermally evaporated in a high vacuum.

4. Results: Space-charge limited photocurrents in CdZnTe

Steady-state photocurrent-voltage characteristics are often used to evaluate important transport properties of semiconductors such as the carrier mobility-lifetime product μτ. The most used theory to fit obtained data is represented by Many´s equation (2.20) which neglects the impact of a space charge. This section aims to compare our derived theoretical models with the well-known Many´s equation.

4.1 Photocurrent

We measured PV characteristics under the continuous regime of cathode illumination. Experimental data for CdZnTe crystal, marked further as sample *A*, together with fits by Many´s equation, SCLP1 and DDF models are shown in Fig. 11. We can see that the measured photocurrent vs voltage curve may be split respectively to the regions of nearly linear rise up to the voltage ~200 V and saturation above 200 V. In the linear region, the space charge induced by the photo-electrons captured in bulk trap levels significantly screens the voltage near the cathode and only part of photo-electrons may pass to the anode while a lot of them disappear near the cathode due to the surface recombination. At the photocurrent saturation, the screening of the electric field near the cathode is suppressed and most of the photo-electrons are collected. The maximum photocurrent at the saturation is limited by the intensity of illumination $j = eI_l$. For the chosen sample A, the photocurrent saturation is well-defined. However, in some samples, we observe unsaturated photocurrent even at high applied biases. More details together with effects leading to unsaturated photocurrents will be discussed in section 4.5.

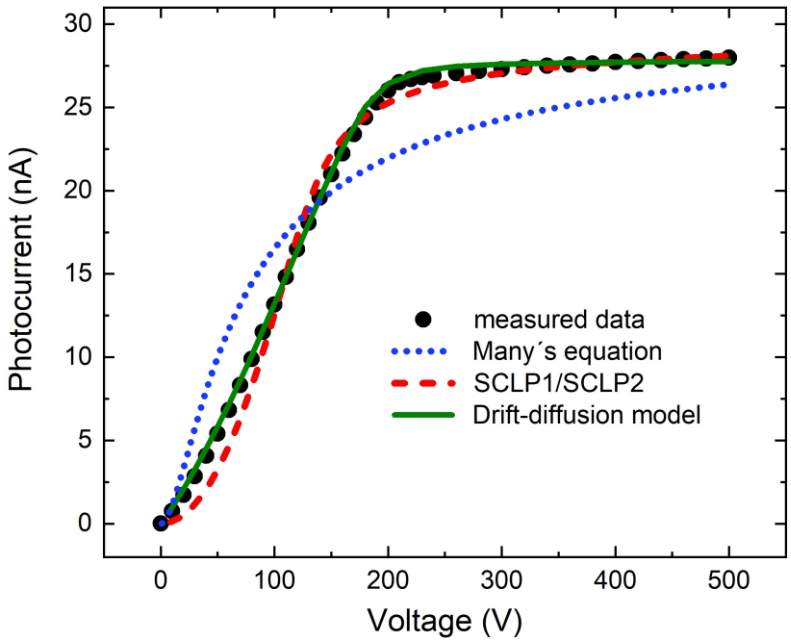

Fig. 11: PV characteristic of sample *A* gained under continuous laser diode illumination with the wavelength of 690 nm, measured in the configuration for collecting electrons only. Measured data are fitted according to the Many´s equation (dotted line), SCLP1/ SCLP2 models (dashed line) and DDF model (green line), respectively.

For sample *A* (see Fig. 11), we may clearly observe a much better agreement of SCLP1 with the experiment compared to Many's fit. A similar disaccord of the Many's fit with the experiment may be identified also in works [51], [52]. Fit parameters obtained from Many´s equation are s_e/μ_e = 140 V·cm^{-1} and $\mu_e\tau_e$ = 2.3 × 10^{-4} cm^2·V^{-1}, which is a five times lower value than the $\mu_e\tau_e$ obtained from alpha spectroscopy.

The fit by the SCLP1 model under the assumption of fixed mobility μ_e = 1057 cm^2·V^{-1}·s^{-1} for CdZnTe [49] gives the surface recombination velocity s_e = 170 000 cm·s^{-1} and $\theta = 5 \times 10^{-5}$. SCLP2 model considering experimentally determined $n_0 = 7.8 \times 10^4$ cm^{-3} leads to an almost identical fit as SCLP1, since the best results for sample *A* are obtained in the presence of a shallow trap with $E_t < 0.54$ eV at which both models coincide.

For the explicit illustration of the effect of various parameters on the photocurrent, we plot in Fig. 12 the SCLP1 fit together with the curves with changed parameters θ, I_l, and s_e, respectively. Initial fitting parameters corresponding to the

black curve remained the same as in Fig. 11. In the case of reduced θ the larger screening of the electric field induced by the respective deep level implies a slower onset of the PV characteristics and delayed saturation. Reduced I_l is represented by correspondingly reduced saturation current. Increased s_e makes the transfer between increasing and saturated parts of the PV characteristics more gradual and the curve is similar to the Many´s equation model. It is seen that the parabolic shape of the PV characteristics at low voltages persists in all situations.

An illustration of the difference between the SCLP1 and SCLP2 models is shown in Fig. 13, where the degenerate Fermi-Dirac statistics were enforced to the SCLP2 model setting $n_1 = n_0$. The parameters of the SCLP1 model remained the same as for the black curve in Fig. 12, while parameters for the SCLP2 model were $\theta = 7 \times 10^{-7}$, $s_e = 170\,000$ cm·s^{-1}, $I_l = 2.6 \times 10^{12}$ cm^{-2}·s^{-1}, $n_1 = n_0 = 7.8 \times 10^4$ cm^{-3}. It is seen that the degenerate level occupancy results even in a slower photocurrent rise which corresponds to the larger polynomial exponent than the 2nd power resulting in SCLP1. Such slow photocurrent rise related to the presence of a deep level was observed in the work [50]. From the shape of PV rise at low voltages presented in Fig. 13 one can estimate whether shallow or deep levels prevail in the material. The accuracy of the estimation may be, however, limited by the participation of holes in the space charge formation.

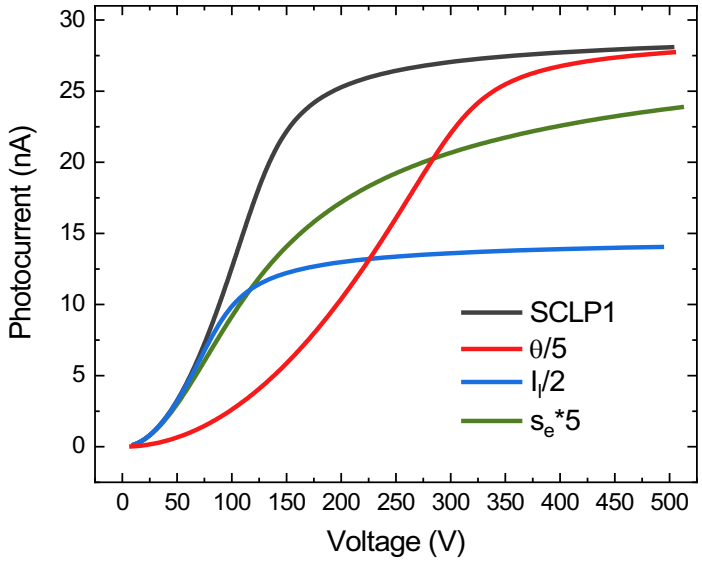

Fig. 12: The influence of change of θ (red line), light intensity I_l (blue line) and surface recombination velocity s_e (green line) on the shape of PV characteristics (black line) calculated by the SCLP1 model.

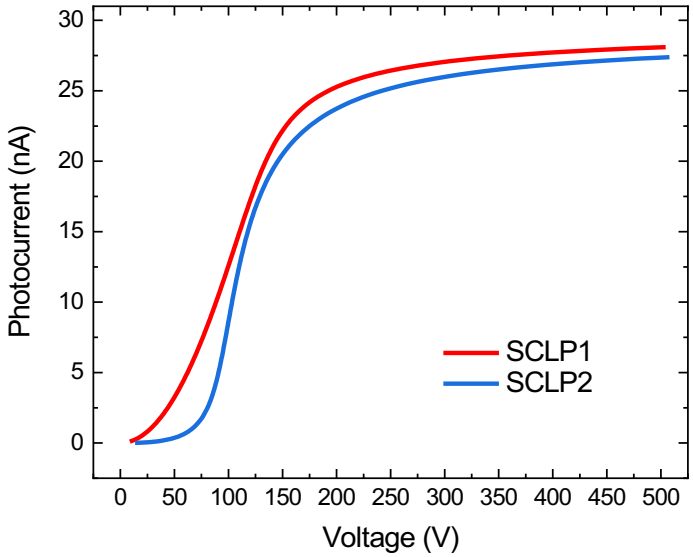

Fig. 13: Comparison of SCLP1 model (red line) and SCLP2 model with defect level on Fermi energy (blue line).

Although the SCLP1 and SCLP2 models fit the experiment in Fig. 11 pretty well, we see a distinct deviation mainly at low biasing in the region of incomplete carrier collection manifesting in the convex bending of SCLP curves. The measured photocurrent has a linear behaviour rather than the parabolic shape gained from the SCLP models. This deviation may be interpreted as a consequence of simplifications used in the derivation of the SCLP models. Based on this consideration we engaged the DDF model described in Section 2.6 and searched for a convenient defect and contact properties, which describe experimental data and which are consistent with the mobility-lifetime product determined from the alpha-spectroscopy.

In Fig. 14 we can see the measurement of PV characteristics at three different excitation intensities (4 µW/cm^2, 2.3 µW/cm^2, and 1.4 µW/cm^2) along with a fit according to the DDF model in which three defect levels and flat bands at metal-semiconductor interface were assumed. The levels are characterized by concentration N_t, energy E_t, and by capture cross-sections of electrons and holes σ_e and σ_h listed in Table 1.

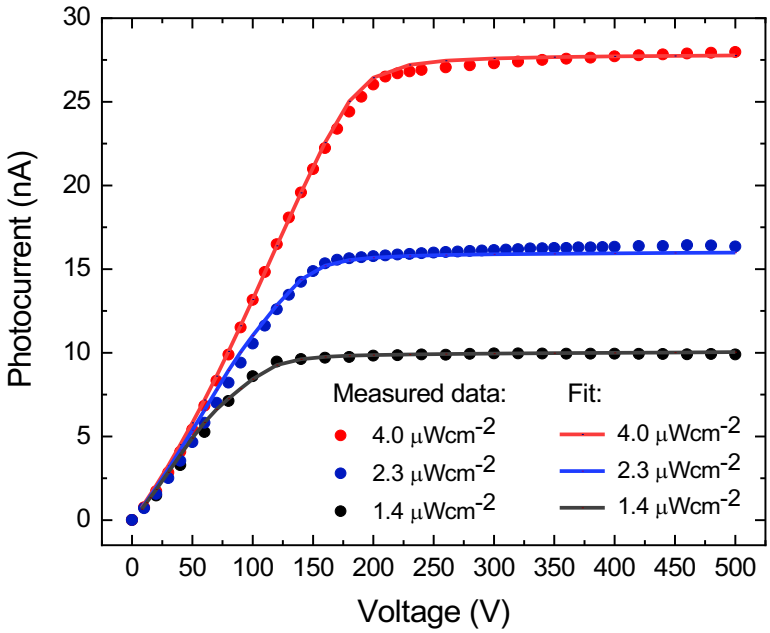

Fig. 14: PV characteristics measured on sample *A* at different light intensities with the wavelength of 690 nm. Measured data are fitted according to the DDF model with parameters listed in Table 1.

Energy level	N_t (cm^{-3})	E_t (eV)	σ_e (cm^2)	σ_h (cm^2)
1	3×10^{11}	0.66	2×10^{-14}	1.0×10^{-14}
2	9×10^{11}	0.85	3×10^{-16}	2.5×10^{-15}
3	2×10^{12}	0.50	1×10^{-14}	0

Table 1: Fitting parameters of defect levels using the DDF model to describe experimental data plotted in Fig. 11 and Fig. 14 .

The energy levels 1 and 2 are important in the fit of the photoconductivity while level 3 was added to fit the appropriate lifetime evaluated from the alpha-spectroscopy. The position of Fermi energy (E_F) used in the DDF model, was set to the midgap region, 0.76 eV below the conduction band. The chosen E_F is consistent with the measured resistivity of the material. Other material parameters are the bandgap energy E_g = 1.57 eV [14] and the hole mobility μ_h = 77 $cm^2 \cdot V \cdot s^{-1}$ [109]. The absorption coefficient corresponding to the photon energy of 1.87 eV was deduced according to [110] as α = 25 000 cm^{-1}. The transfer rate defining the transfer of electrons through

the cathode $\gamma_e^{(0)} = 5 \times 10^4$ cm·s^{-1} was obtained by the fit. Other transfer rates $\gamma_h^{(0)}$, $\gamma_e^{(L)}$, $\gamma_e^{(0)}$ did not influence the fit markedly and they were not fitted. They were fixed at a high value of 10^7 cm·s^{-1}, which affords the surface density of respective free carriers defined directly by the Schottky barrier.

Important characteristics of the fit are outlined in Fig. 15, where the electric field and space charge density (Fig. 15a), level occupancy (Fig. 15b), and free carrier density (Fig. 15c) profiles calculated at the 30 V are shown. Photo-excited electrons are primarily trapped on level 1 forming a negative space charge in the bulk of the sample. As a consequence, the electric field is screened near the cathode and is increasing towards the anode, which is depicted as a red line in Fig. 15a.

The important feature distinct from the predictions of SCLP models is the shoulder clearly seen at the position x ≈ 0.5 mm in all profiles. The reason for this artefact lies in the injection of holes from the anode and their participation in the space charge formation. While the density of anode-injected holes is low in the region x ∈ (0.5, 1.4) mm due to a higher electric field, it increases near the cathode for x < 0.5 mm due to the lowered electric field. Consequently, the enhanced hole trapping close to the cathode, mainly on level 2, results in a significant compensation of the negative space charge formed by the photo-generated electrons in the sample for x < 0.5 mm. The width of this compensated region is dependent on the applied voltage and enlarges with the decreasing voltage. Since the deep electron trap level 1 is significantly filled by trapped electrons, the free electron lifetime increases and the electrons may pass the compensated region without strong trapping or recombination. The photocurrent then exceeds the parabolic-like theoretical prediction of the SCLP models and attains a nearly linear shape at low voltages. The linear growth of photocurrent at the low voltages observed in other works [51], [52], [54], [56], [63], [65], [66], [111] may be also assigned to the above-described phenomena in which injected holes from anode participate in the charge transport.

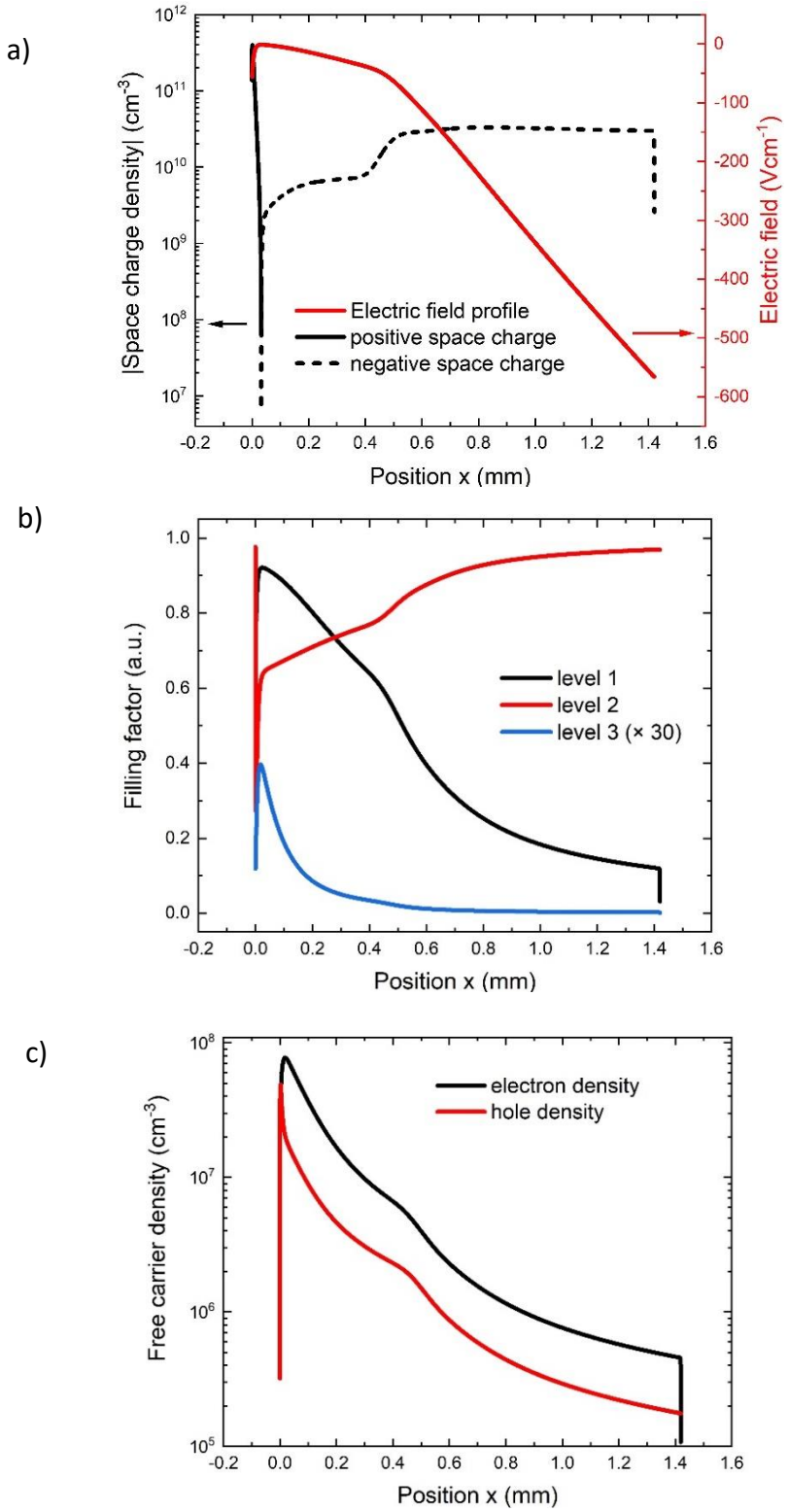

Fig. 15: (a) Absolute value of the space charge density normalized by the elementary charge and electric field profile, (b) Profile of the occupancy of defect levels defined in Table 1 (blue line was multiplied by a factor of 30), and (c) Profile of the free electron and hole density calculated by the DDF model for the 30 V voltage and illumination intensity 2.3 μW·cm^{-2} with fit parameters listed in Table 1.

The positive space charge formed close to the cathode up to the depth x ~ 3 µm, see Fig. 15a and Fig. 15b, is caused by the trapping of photo-excited holes on level 2. This effect results in the enhancement of the electric field near the cathode and increases the injection of electrons from the contact. In the investigated sample A the injecting electrons are significantly damped by the low transfer rate $\gamma_e^{(0)}$. Larger $\gamma_e^{(0)}$would lead to the emphasized photoconductive gain [112] and no saturated photocurrent could be seen.

Though the number of parameters defining the fit looks pretty large, a simplification of the model and reduction of the number of parameters, for example by joining levels 1 and 2 to an appropriate single level was not successful. It is also worth mentioning that a similar model with two midgap levels was successfully applied in the explanation of the depolarization of the CdZnTe radiation detector by the above-band-gap light [113]. In summary, the presented model with two levels positioned near the Fermi energy and another shallower electron trap conveniently depicts important features of the charge dynamics in the sample and consistently complies with all experimental results.

4.2 Transient current measurement

We further compared the L-TCT signal of sample *A* measured both in the dark and at the steady-state cathode illumination to prove the existence of space charge in CZT. First, we illuminated the cathode of the sample only by probing laser pulses. Laser intensity and frequency were low enough so that the illumination did not influence the properties of the sample but served only for the characterization of the internal electric field. Formation of the space charge originating from trapped photo-generated carriers was in this case eliminated.

Examples of CWFs collected at different voltages 30 V, 100 V, and 300 V are plotted in Fig. 16(a)-(c), respectively, by black curves labelled ‘without LED’. The dotted lines represent the fit using the DDF model with parameters listed in Table 1.

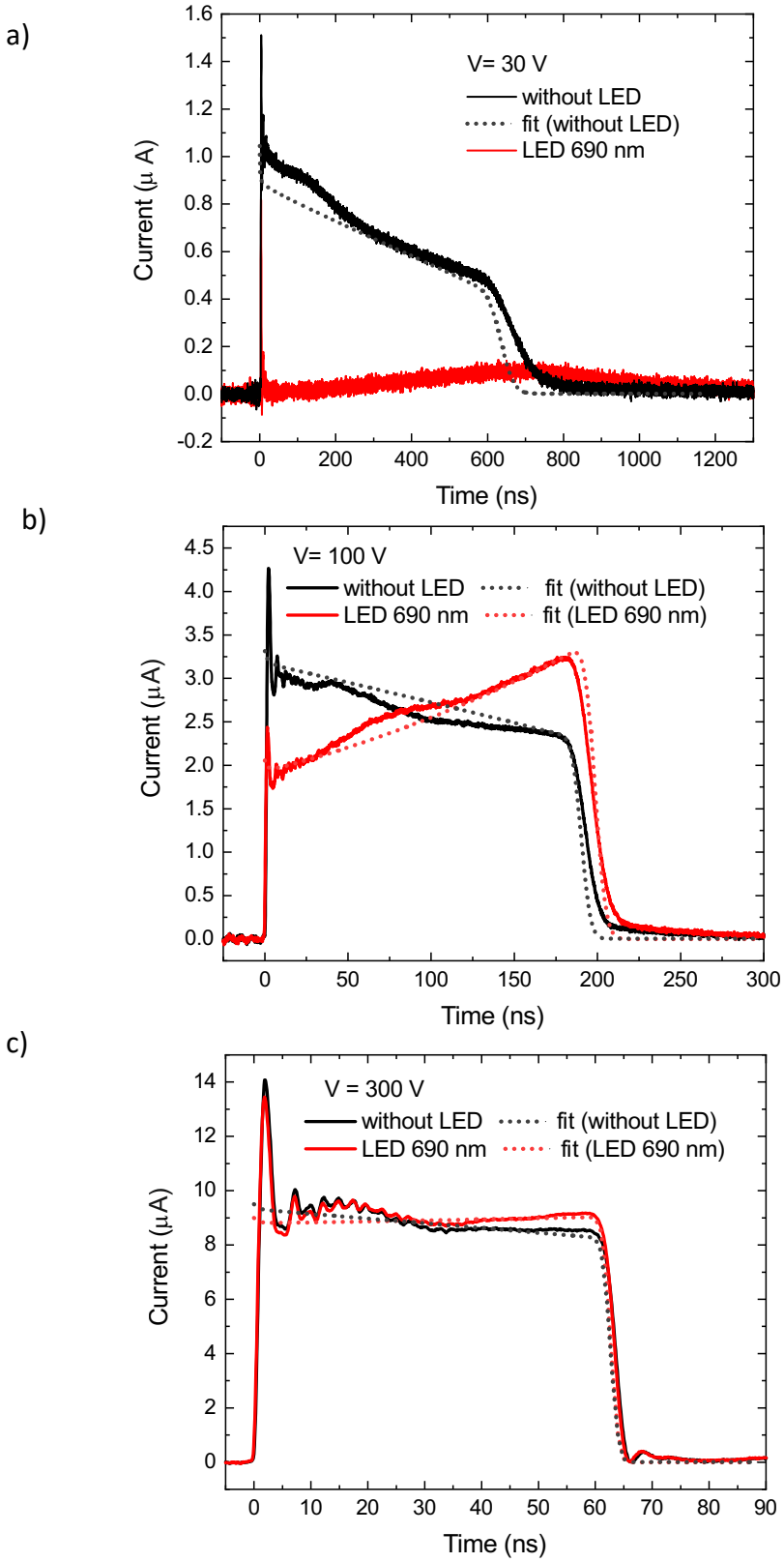

Fig. 16: (a)- (c) Current waveforms measured on sample *A* by L-TCT using laser pulses only (black line) and with additional continuous LED illumination 690 nm (red line) for voltage a) 30 V, b) 100 V and c) 300 V. Dotted lines represent the fit using DDF model with parameters listed in Table 1.

The descending CWF apparent at all voltages is dominantly induced by the finite electron lifetime τ_e = 1.2 μs. The same τ_e was also derived from the alpha-spectroscopy measurement and it is consistent with fitting parameters defining defect level 3. The descending CWF at 30 V has a damping factor c higher than it could be explained only by determined $\mu\tau$, which proves the weak positive charging of the biased sample [89]. The positive space charge appearing in this setup could be created due to the variation of carrier density induced by slightly blocking the cathode or injecting anode gold contacts. Such an effect is often observed in Au/n-CdZnTe/Au radiation detectors [90]. Weak undulations in the waveforms are partly caused by the sample inhomogeneity and also by the electronics used [90].

In the second regime, the cathode was simultaneously illuminated by the above-described probing pulses and by a continuous LED with a wavelength of 690 nm. In this case, we simulated the conditions, which occur in the sample during continuous photocurrent measurements. Since the L-TCT records only deviations from the steady-state, the generated greater amount of charge carriers in the case of additional continuous illumination should not contribute to the total current pulse. The principal effect of the cathode illumination on the transient current profile is clearly demonstrated in Fig. 16(a)-(c) by red waveforms labelled 'LED 690 nm'. The variations of CWFs at the steady-state cathode illumination are caused by the warping of the electric field induced by the negative space charge appearing due to the photo-carrier trapping. The significantly suppressed electric field at low biasing results in a strong surface recombination and reduced collected charge. This phenomenon can be seen in Fig. 16(a) since the area under the CWF corresponds to the collected charge. By increasing voltage, the electric field near the cathode grows in parallel as the screening fades away, surface recombination attenuates and the waveforms attain their undisturbed shape as is apparent in Fig. 16(c). The crossing between the screened and unscreened cathode is ideally illustrated by the CWF in Fig. 16(b) where the waveform though significantly tilted reveals features similar to the regular shape. Ascending CWF is consistent with the negative space charge created by trapped photo-generated electrons under continuous illumination, which induces the ascending transient current, in which the CWF damping due to lifetime is overcome. Moreover, the charge collection efficiencies at 100 V and 300 V biasing

were higher in the case of continuous illumination than in the dark. We interpret this effect as the result of the filling of electron traps by electrons created by steady excitation.

4.3 Many's equation

Many´s equation (2.20) is routinely used in the evaluation of the mobility-lifetime product and surface recombination. However, it is seen in Fig. 11 that the fit with eq. (2.20) neither approximates the experiment satisfactorily nor gives $\mu_e\tau_e$ evaluated with the alpha spectroscopy. The reason primarily consists in the experimental conditions, when the space charge formation significantly violated the homogeneous electric field in the sample presumed in the derivation of eq. (2.20). To assess this eventuality we perform the simulation with the DDF model using the defect structure given in Table 1 and taking a very low excitation intensity I = 2.5×10^9 photons per cm^2 per second, which is 1000× less than the maximum intensity used in Fig. 14. The photo-induced space charge formation was then significantly suppressed. Such measurement of the photoconductivity is limited only to samples with low noise so that a good quality signal could be retrieved. The calculations were done in the dynamic regime of the photoconductivity measurements as can be seen in Fig. 17(a). Both voltage and light were switched on at t = 0 on the sample in the equilibrium and the current was obtained after a respective period t_d of steady illumination and biasing. Dark current was calculated in the same way but without switching on the light. This approach ensures the well-defined setting of the sample evolution without inevitable memory effects, which should be anticipated in a real chopped experiment. The photocurrent was obtained by the differentiation of the values. The results are shown in Fig. 17(b) where the PV characteristics for different t_d are plotted. We also add the relevant graphs of Many's function (2.20) with the correct $\mu_e\tau_e = 1.2\times10^{-3}$ cm^2/V (dotted line) and different $\mu_e\tau_e = 5.2\times10^{-3}$ cm^2/V (dashed line).

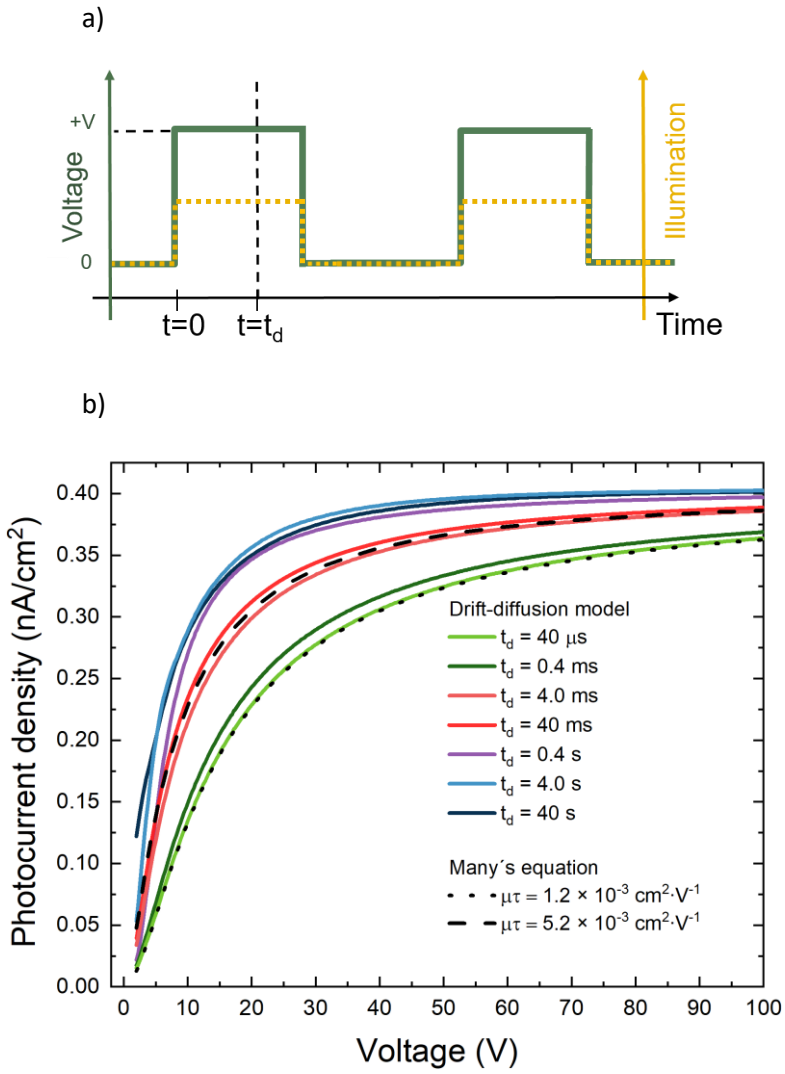

Fig. 17: a) Time scheme of chopped experiment b) DDF model of PV characteristics obtained in a chopped regime of illumination with different period t_d of illumination and biasing (full lines) and their comparison with Many´s equation (dashed and dotted line) with various mobility life-time products.

We may see that exact $\mu_e\tau_e$ may be obtained in the short-pulse setup when t_d < 40 µs. This finding is consistent with the L-TCT measured at the pulsed voltage [114], where exact $\mu_e\tau_e$ unaffected by the polarization may be determined.

Extending t_d to about 1 ms shows a continuous deviation from the correct curve to significantly larger $\mu_e\tau_e = 5.2\times10^{-3}$ cm^2/V. The reason for this shift consists of the de-trapping properties of level 3, see Table 1, acting as the electron trap. The de-trapping time of this level is 1 ms. Using t_d similar to or larger than the de-trapping time allows trapped carriers to come into equilibrium with free electrons in the conduction band and the level becomes invisible in time-resolved experiments.

Omitting level 3, the remaining levels 1 and 2 define $\mu_e\tau_e = 5.2\times10^{-3}$ cm^2/V and a comparison of calculated profiles with the respective (dashed) curve perfectly agrees with this expectation.

A further increase of t_d to $t_d > 0.1$ s shows a continuous deflection of the curve especially at low voltage, which can be interpreted as a further improvement of $\mu_e\tau_e$. Such an interpretation is, however, incorrect. The correct explanation consists of (i) the charging of deep levels due to electron depletion induced by blocking cathode defined by low $\gamma_e^{(0)}$and (ii) the trapping of photo-holes near the cathode. While item (i) induces the positive space charge within the bulk of the sample, process (ii) entails the formation of a large positive space charge in a thin layer in the cathode. The activity of both processes leads to an enhancement of the electric field near the cathode and an increase of the photocurrent, so-called photoconductive gain.

To conclude, the validity of Many´s equation (2.20) is, in practice, limited mainly by three factors. The first is a negative space charge from trapped photo-electrons which leads to an inhomogeneous electric field profile. The use of Many´s equation (2.20) then leads to a significantly lower value of $\mu_e\tau_e$ compared with that of its real value. The second factor corresponds to the case of an experiment in which the period t_d is similar to or larger than the detrapping time of the shallow level. In this case, the shallow level is not reflected in the PV measurement. As mentioned in section 4.1, level 3 does not strongly influence the fitted shape of the PV curves in Fig. 14, where only energy levels 1 and 2 are important in the fit of the photoconductivity. Level 3 is here added according to the knowledge of the lifetime obtained from alpha spectroscopy. The third frequent phenomenon limiting the relevance of Many's Eq. (2.20) is a positive space charge in the vicinity of the cathode, which may lead to photoconductive gain. The use of Many's Eq. (2.20), in the case of the last two phenomena, leads to a significantly higher value of $\mu_e\tau_e$ than that recorded in reality.

4.4 Space-charge density

Previous studies [50]–[52], [54], [56], [55], [57]–[62], [64], [67]–[69], [115], [116], measured the steady-state PV characteristics to evaluate the mobility-lifetime product. However, as we demonstrate in this paper, even for a chopped regime of

illumination, with a different period, t_d, of illumination and biasing, correct evaluation of the carrier lifetime is restricted to a sufficiently short period of t_d. Such a short t_d puts additional demands on laboratory equipment and practically negates the convenience of photoconductivity measurements, which profit from their simplicity. Many's Eq. (2.20) and du Chatenier's model, therefore, do not allow researchers to credibly determine the mobility-lifetime product or other dynamic parameters. Here, the following question arises: what is the practical use of steady-state or chopped PV characteristics when one of the most crucial material parameters, the carrier lifetime, cannot be determined?

Recent progress in the development of radiation detectors is reflected mainly in a significant increase in a carrier lifetime. In CdZnTe, the mobility-lifetime product and electron lifetime exceed 0.1 cm^2/V and 100 μs, respectively [117]. Contrary to the mastered sufficiently long lifetime, the charging of detectors remains an issue. Even weak charging at a level of 10^9 cm^{-3} may disable thick detectors, especially those of several centimetres thick, from application. Suppression of space-charge formation in biased semiconductor radiation detectors thus represents an important challenge for further progress in high-quality detector research. The space charge leads to an inhomogeneous electric field distribution inside the material, and it can even induce the appearance of an inactive layer where the electric field falls to almost zero.

As follows from the analysis above, in contrast to the carrier lifetime, which is barely accessible from photoconductivity measurements, space-charge formation in illuminated detectors may be conveniently studied. Previously defined models, SCLP1, SCLP2, and DDF, may be used for the determination of the space-charge distribution within the sample.

Average space-charge density $\langle\rho\rangle$, depicting the space charge distribution, can be easily determined by the integration of Gauss's law:

$$\langle\rho\rangle = \frac{\epsilon_0\epsilon_r}{eL}\,[E(L) - E(0)]. \tag{4.1}$$

Electric field values E(L), and E(0) corresponding to the SCLP1 model may be simply obtained from equations (2.30) and (2.32), respectively. In the case of SCLP2 and DDF models, both quantities are obtained simultaneously upon fitting.

First, we calculate ⟨ρ⟩, from the DDF model using the fit of PV measurements plotted in Fig. 14. The resulting ⟨ρ⟩, depending on applied voltage, is shown in Fig. 18 by dotted lines. We observe the typical ascending-descending profile of ⟨ρ⟩ versus applied voltage. The growth of ⟨ρ⟩ at low voltage is mediated by the increasing electric field, which promotes penetration of the space charge from the highly excited surface layer to the sample's interior. The descending part of ⟨ρ⟩ appears upon exhaustion of the surface source, when space-charge-induced screening is overcome by the voltage. The electric field increases near the cathode, electrons drift rapidly into the sample's interior, and the mean electron density decreases, which accordingly results in space-charge reduction.

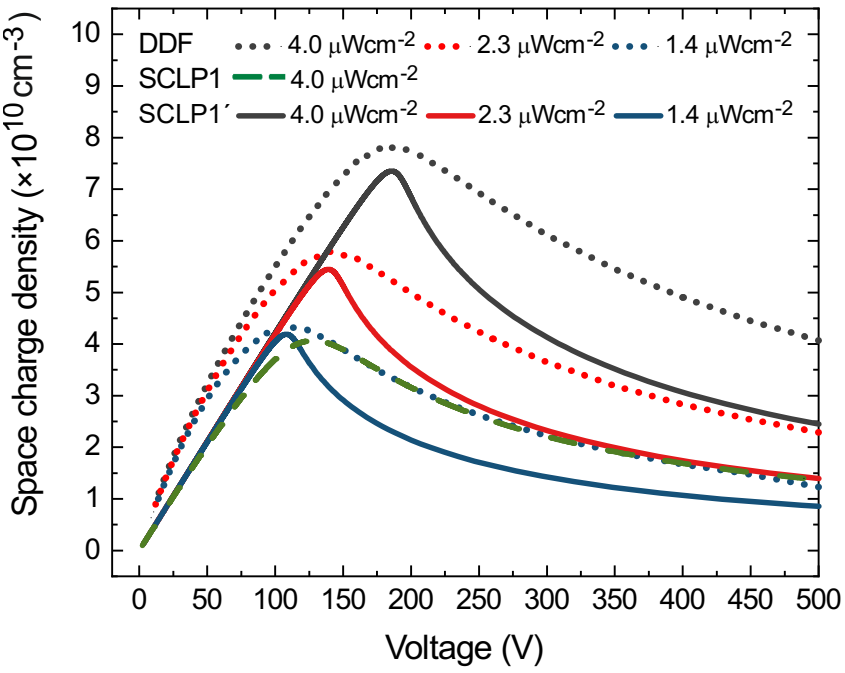

Fig. 18: Average space charge density ⟨ρ⟩ for different illumination intensities. Calculations were done by SCLP1 model (green dashed line) and DDF model with the same fit parameters as in Fig. 11 (dotted lines) and by SCLP1' model with negligible surface recombination (full line).

In the next step, we calculate ⟨ρ⟩, using the SCLP1 fit of the same data. For the sake of clarity, we plot (dashed line) only the curve for the maximum excitation intensity presented in Fig. 11. The SCLP1 fit produces a significantly different curve from that of the DDF model, with a maximum shifted by 50 V towards the lower voltage and reaching about half ⟨ρ⟩ in the maximum. Apparently, one can deduce that the SCLP1 fit is unsuitable for the credible determination of ⟨ρ⟩.

To identify the reason for the discrepancy between the fits of the DDF and SCLP1 models, we concentrate on the shoulder that separates the rising and saturation parts of the PV characteristics. We find that a much better agreement between ⟨ρ⟩ calculated from the SCLPs and DDF models is obtained by using a modified SCLP1' fit, which is defined by the position of this shoulder, where only parameter θ is fitted and *s* is fixed to be very low. The reason for this improvement involves the systematic error embodied in the two-parametric (θ, *s*) fit of the PV experiment in its ascending part by the oversimplified SCLP1 model. The effort to fit a nearly linear course of the PV curve by the implicitly parabolic-like profile of the SCLP1 model leads to a higher value of s_e and consequently, to a less sharp shoulder in the PV curve. Due to this feature, ⟨ρ⟩ derived by the two-parametric fit is lower and its maximum is shifted to lower voltage. Respective ⟨ρ⟩ values calculated with the SCLP1' model are plotted as solid lines in Fig. 18. Good agreement with the DDF model, especially at the maxima, is seen.

Summarizing these achievements, we supply practical advice to researchers for how they may determine, easily and with acceptable precision, the average space-charge density from the SCLP1 model. First, one has to determine, as precisely as possible, the position of the shoulder in the PV characteristic, which is defined by voltage V_S and photocurrent density j_S. The parameter θ is then calculated, according to eq. (2.29), as

$$\theta = \frac{8}{9}\frac{L^3 j_S}{\varepsilon_0 \varepsilon_s \mu_e V_S^2}. \tag{4.2}$$

Other quantities, i.e., electric field and space charge, are then calculated from (2.30) and (4.1), when the boundary condition in (2.32), with low s, typically 10^4 cm/s, is used. Taking the critical fitted point in the photoconductivity shoulder is an optimum

option, since it corresponds to the sample with a minimized effect of holes, compensating for the space charge at low voltage and, simultaneously, reduced surface recombination due to the drain of electrons induced by enhanced voltage. In contrast to $\theta = 5\times10^{-5}$ determined by the SCLP1 fit in Fig. 11, the improved approach affords $\theta = 2.7\times10^{-5}$.

The advantage of this procedure, in contrast to the obvious SCLC technique, lies in the versatility of the SCLP methods applicable to materials equipped with different contacts, either blocking or injecting. Sufficiently intensive illumination overcomes the effect of the contacts and the space charge may be determined independently.

Photoconductivity may also be used in the mapping of the lateral electric field non-uniformity of planar samples, where scanning of the sample's area may be achieved by multiple other techniques. An example of such an investigation is found in [118].

4.5 Unsaturated photocurrent-voltage characteristics

As previously mentioned in section 4.1, we observe different behaviours of photocurrent-voltage characteristics. The comparison of photocurrent-voltage characteristics for samples *A*, *B*, *C* and *D* measured by irradiation of cathode side with laser diode of wavelength 690 nm is shown in Fig. 19. Firstly, the difference lies in the maximum value of photocurrent obtained at the highest applied bias of 500 V. This phenomenon can be explained by generation of different amounts of light-induced charge carriers thanks to the variations in the thickness of prepared gold contacts and hence varying transmission of incident light through contacts. However, more interesting is that the shapes of photocurrent-voltage characteristics vary. Some photocurrent-voltage characteristics saturate, as can be expected due to the finite intensity of the light source, and some do not saturate even at higher biases. The latter behaviour indicating quantum efficiency over 100% is often observed in the metal-semiconductor-metal structures based on a high resistivity semiconductor crystal such as CdTe [119], [120], GaAs [121], GaN [122], Si [123], [124], and NiO [125].

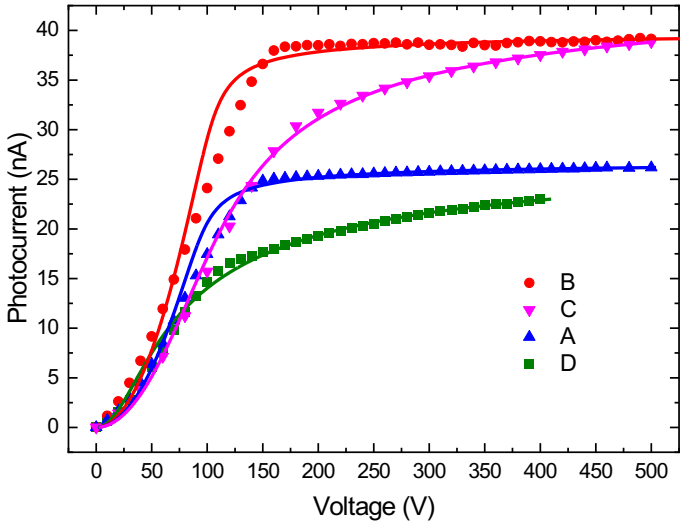

Fig. 19: Comparison of photocurrent-voltage characteristics of samples A, B, C and D measured by laser diode 690 nm in configuration for collecting electrons. Measured data are fitted by SCLP1.

High surface recombination, persisting even at large applied voltages, represents the first possible explanation for such photocurrent unsaturation. Fitting according to the SCLP1 model also supports this idea because it gives higher surface recombination velocities for those samples in which photocurrents do not saturate. Specifically, surface recombination velocities for samples *A*, *B*, *C,* and *D* were respectively 790 $m \cdot s^{-1}$, 760 $m \cdot s^{-1}$, 3 970 $m \cdot s^{-1}$ and 5 600 $m \cdot s^{-1}$.

Another explanation for photocurrent non-saturation can be excessive injection of the electrode under illumination. Therefore, the dark current flowing through an illuminated sample is generally higher than the dark current flowing through the sample in the dark. In such cases, a simple evaluation of photocurrent as a difference between current under illumination and dark current leads to improper values containing not only the contribution of photo-generated carriers but also the contribution of redundant injected carriers. The mechanism by which this anomalous gain occurs may be attributed to the modification of the Schottky barrier by photo-generated charge, especially by residual holes in the vicinity of the metal-semiconductor interface since the holes are usually characterized by lower mobility. Hole trapping near the illuminated cathode may occur either in surface states, in deep traps in the semiconductor bulk material, or a thin insulating layer between the

metal and the semiconductor. Holes that are localised in these states create here positive space charge which will amplify the internal electric field near the cathode. Thanks to that the barrier height and width at the metal-semiconductor interface will be reduced due to the Schottky effect, which leads to additional electron injection from the metal into the semiconductor, either by tunnelling or by thermionic emission. The excess injection of illuminated cathode caused by trapped photo-holes near the cathode, so-called photoconductive gain, has been previously observed in [92], [112], [121], [122].

To determine which physical phenomenon leads to the non-saturation of photocurrent-voltage characteristics, we propose an experimental verification method. The method is based on a comparison of theoretically calculated and measured photocurrent at the bias voltage that is considered to be high enough to collect all photo-generated carriers. A larger measured photocurrent compared to theoretical means that the non-illuminated contact collects excess carriers besides photo-generated ones. It thus proves the photoconductive gain from the injection of the illuminated electrode. A smaller measured photocurrent compared to theoretical means that the surface recombination occurs.

To obtain the theoretical value of photocurrent at a given applied bias (e.g. 500 V) we need to know the number of light-induced photo-carriers. By measuring the power of incident continuous illumination, one can easily evaluate the number of incident above-bandgap photons N_{ci}. The knowledge of N_{ci} alone is, however, not sufficient as it is not sure how many photons get through the prepared gold contacts. The parameter connected to the cathode transmittance may be experimentally obtained by the L-TCT method using probe laser pulses of the same above-bandgap energy as previously used in the continuous regime of illumination. The used probe laser pulses should be weak enough to not affect the sample or contact properties. From the integration of the obtained current waveform at a given bias (e.g. 500 V), we can determine the amount of collected charge. To obtain collected charge one may use also spectra measurements or the transient charge current technique (TCHT). Then simple division of collected charge by an elementary charge e gives us the number N_{pt} of transmitted photons through illuminated gold electrode by single pulse. Subsequently, the number of overall incident photons per single pulse N_{pi} can

be determined by measuring the power of incident pulse irradiation. The ratio of a number of transmitted to incident photons gives as a parameter β which can be understood as a quantum efficiency of photo-carrier formation. The parameter β must be smaller than one. Under consideration that parameter β does not change for a continuous regime of illumination, we can finally calculate the theoretical photocurrent I_t that should flow through the biased detector at the applied continuous illumination as:

$$I_t = e\beta N_{ci} = eN_{ct}. \tag{4.3}$$

Here e, N_{ci}, and N_{ct} represent elementary charge, the number of incident and transmitted photons under given continuous irradiation, respectively. Comparison of theoretical and measured real photocurrent at the same high bias (e.g. 500 V) can then decide whether surface recombination or excess electrode injection occurs in samples with unsaturated photocurrent-voltage characteristics.

To measure the power of incident light we use digital meter console PM100D with photodiode sensor S120C from Thorlabs. The number of incident photons per pulse N_{pi} was then determined from measured average power Pp of pulse irradiation according to the following equation

$$N_{pi} = \frac{P_p}{f_p}\frac{\lambda}{hc} = E_p\frac{\lambda}{hc}. \tag{4.4}$$

Here f_p corresponds to the frequency of laser pulses, E_p to the total energy in a single pulse, and symbols λ, h, and c represent light wavelength, Planck constant, and light speed in vacuum, respectively. For L-TCT measurement of parameter β we use the probe pulse of 2 kHz frequency, 5 ns width, and 690 nm wavelength. Most samples have the coefficient β varying in the range between 1 to 10 %. We verify that the coefficient β is not dependent on probe pulse parameters, specifically on frequency, amplitude, and width, and hence may be legitimately used in the calculation of theoretical photocurrent under continuous illumination according to the eq. (4.3).

We provide the above-described verification method on eight CdZnTe detectors. Their corresponding photocurrent-voltage characteristics are shown in Fig. 20. The calculated theoretical photocurrents according to the eq. (4.3) together with directly measured photocurrent at 500 V are stated in Table 2.

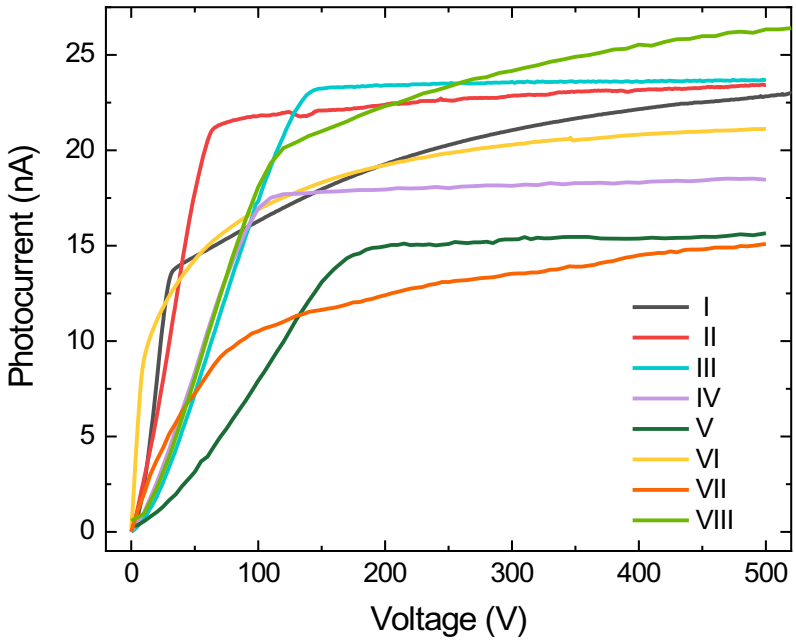

Fig. 20: Photocurrent-voltage characteristics of *CdZnTe* samples I - VIII gained under continuous laser diode illumination with the wavelength 690 nm, measured in the configuration for collecting electrons only.

Note that L-TCT measurements and PV characteristics are done in the same geometrical configuration with the same light source, used once in pulse and then in continuous regime of illumination, and at the same bias of 500 V. As can be seen from Table 2, theoretical photocurrents greater than measured ones are recorded for samples I and II. The non-saturation of PV characteristics may be thus attributed to severe surface recombination persisting even at high biases applied to the sample. This approach hasn´t been yet discussed in previous publications as a possible source of non-saturation. Samples III, IV, and V exhibit saturated PV characteristics, with only a small increase attributed to a slight excess injection of illuminated cathode. The photocurrent non-saturation observed in samples VI, VII, and VIII may be assigned to the cathode injection, according to the smaller theoretical compared to the measured photocurrent. Note that the absolute values $I_{m,\,500V} - I_{t,\,500V}$ in Table 2 are in good agreement with the individual differences between the value of the real photocurrent at 500 V and the real photocurrent at the bias corresponding to the bending of PV characteristics, $I_{m,\,500V} - I_{m,\,bend}$. This confirms the validity of used verification method. The exception applies to sample VIII and IV, where is the most

obvious difference between $I_{m,\,500V} - I_{t,\,500V}$ and $I_{m,\,500V} - I_{m,\,bend}$. Such inconsistency may be explained by the fact that, probably both mechanisms, surface recombination and electrode injection, contribute significantly to the non-saturated shape of PV characteristic.

Sample	I_t (nA)	I_m (nA)	$I_{m,500V} - I_{t,\,500V}$ (nA)	$I_{m,500V} - I_{m,\,bend}$ (nA)	*Gain mechanism*
I	32.37	22.78	-9.59	9.01	Surface recombination
II	26.00	23.14	-2.86	2.00	Surface recombination
III	22.43	22.82	0.39	0.58	Slight injection
IV	17.54	18.42	0.88	1.46	Slight injection
V	14.96	15.47	0.51	0.68	Slight injection
VI	8.76	21.03	12.27	11.97	Cathode injection
VII	11.53	14.81	3.28	4.66	Cathode injection
VIII	23.00	26.30	3.30	6.2	Cathode injection

Table 2: The prevailing effect leading to the non-saturation of photocurrent-voltage characteristics, obtained based on the difference between directly measured photocurrent $I_{m,\,500V}$ at 500 V, and theoretical photocurrent $I_{t,\,500V}$ at 500 V.

4.6 Conclusion: Space-charge limited photocurrents in CdZnTe

We measure steady-state photocurrents on planar (Cd, Zn)Te radiation detectors under above-band-gap illumination and analyse them by analytical and numerical models. Three models, SCLP1, SCLP2, and the drift-diffusion model, describing space-charge-limited photocurrents, are developed and conveniently applied in the fitting of experimental data with much better precision than that obtained in a previous approach using Many's Eq. (2.20). Additionally, we create a

model that describes transient currents in the case of an inhomogeneous space-charge distribution induced by cathode illumination (section 3.1.3). Within the SCLP1/SCLP2 models, we show that degeneracy of deep level leads to a slower photocurrent onset, corresponding to a larger polynomial exponent than that of the second power resulting in SCLP1. We conclude that the shape of the onset can be used as a rough estimation of whether shallow or deep levels dominate the material. Moreover, we propose a simple method for the determination of the average space-charge density from the SCLP1 model at a certain voltage.

The numerical drift-diffusion model explains consistently all experimental data, the PV characteristics at various illumination intensities, and the transient currents measured at different biasing in the sample held both in the dark and with a continuously LED illuminated cathode. Three defect levels, with energies of 0.66, 0.85, and 0.50 eV, are ascribed to the measured sample. The experimentally observed linear onset of the photocurrent at low voltages, which also frequently appears in multiple studies, is explained by the compensation of the negative space charge near the illuminated cathode by trapped injected holes.

Numerical simulations of PV characteristics at low intensities and in the chopped regime show that the validity of Many's eq. (2.20) is, in practice, limited not only by the space charge from trapped photo-generated electrons but also by the photoconductive gain caused by the trapping of photo-generated holes in the vicinity of the cathode. An incorrect determination of the mobility-lifetime product also results from the fact that shallow levels, with de-trapping times shorter than the period of illumination, do not influence PV characteristics.

We explain the non-saturation of PV characteristics, observed in several samples, by persisting surface recombination and excess injection of illuminated cathode due to positive space charge near the cathode. To distinguish between these two phenomena we propose a verification method, which uses L-TCT measurement and proves that both mechanisms can prevail in individual samples.

The collected achievements allowed us to conclude that the measurements of the steady-state photo-current if they are used as a single analytical method, do not enable researchers to credibly evaluate the carrier lifetime as well as other carrier dynamic parameters. The measurement of PV characteristics should be completed

by the independent measurement of mobility-lifetime product such as transient current technique or alpha spectroscopy measurements. The measurement of PV characteristics at various intensities, together with knowledge of the carrier lifetime, then gives a detailed picture of the defect structure of the material using the drift-diffusion model. Certain shallow levels may not be distinguished in the defect structure from PV measurements without considering the lifetime obtained from other experiments.

Most of the above-presented results from chapters 2.4 - 2.6, 3.1.3 and from section 4 were published in the article *Ridzonova et al., Phys. Rev. Applied, 2020* [126].

5. Results: Lead halide perovskites $APbX_3$

Here, we focus on the light-induced changes in perovskites, as the lack of stability under illumination remains an issue for their applications. Specifically, we study the effect of light on charge carrier transport in $CH_3NH_3PbBr_3$ (MAPB) single crystals. We use for this, as previously in CdZnTe, the combination of PV characteristics and L-TCT measurements under steady-state illumination.

5.1 L-TCT measurements on MAPI single crystals under DC bias

For L-TCT measurement, we illuminate the cathode side and thus measure only electron signals. We record the time evolution of transient currents after applying a DC bias of 15 V to the MAPI single crystals, which can be seen in Fig. 21. Interestingly, the measured transient waveforms do not show any distinguishable shoulder corresponding to the transit time. This suggests, that electrons generated near irradiated contact are not able to pass through the whole sample thickness to the opposite contact. This may be a consequence of low electron lifetime or the presence of a dead layer with zero voltage inside the measured sample.

Measured transients in Fig. 21 show strong hysteresis, which means that the exact shape of the waveform is dependent on the time of applied voltage. Such hysteresis effects in perovskites have been previously assigned to ion migration [40]–[42], as perovskites show besides electron and hole conductivity also strong ion conductivity. Applied DC bias may lead to the drift of charged ions toward corresponding electrodes. Here, they can create space charge and lead to the non-homogenous electric field.

At earlier times of applying bias (5 s – 11 s), the transient currents show a steeper decline and lower amount of collected charge, given by an area under CWF, compared to longer times of applied bias. The steeper exponential decline at times 5 – 11 s of applying bias may be according to equations (3.4) - (3.6) connected with both shorter mobility-lifetime product or with positive space charge accumulation under the illuminated cathode. It is not possible to distinguish which process is dominant.

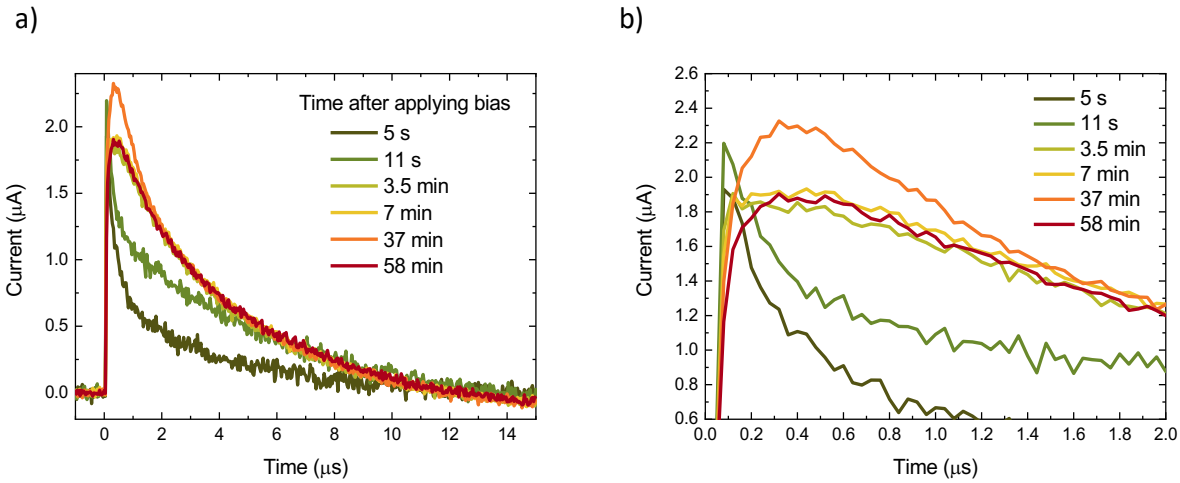

Fig. 21: a) Electron CWFs measured on MAPI single crystal at different times after applying bias 15 V to the sample. b) Detail of measured transient current waveforms from Fig. 21a.

In case of positive space charge, bands at the metal-semiconductor interface are bent upward. At 3.5 minutes after applying voltage, we observe an almost flat transient current waveform up to 0.5 μs. This suggests flat bands at metal-semiconductor interface. Thus at this time, there must be at 3.5 min a very low space charge accumulation under the cathode. This band-bending change is probably caused by the chemical reaction of migrating ions on the interface [3]. Interestingly, after 37 minutes of biasing, the transient current waveform increases up to a transient time of 0.4 μs. This is connected with the negative space charge just below the cathode which corresponds to bands bent downward.

5.2 L-TCT measurements on MAPB single crystals under pulsing bias

The electron L-TCT signals are much weaker compared to the hole signals in perovskite materials [127]. This is a consequence of a significantly lower lifetime of electrons compared to hole lifetime. Therefore, we illuminate here only the anode side of the measured sample by the probe laser pulses and record purely signals of drifting photo-generated holes.

To prevent ion migration, we use a pulsed-bias regime to measure L-TCT on perovskite MAPB single crystals. The scheme of pulsing bias parameters is shown in Fig. 6. One may still object that a pulsing bias regime with only one polarity still

contributes to the drift of ions in the same direction. To show the sufficiency of one polarity bias pulsing in suppressing ion migration we perform L-TCT measurement at a constant frequency of 5 Hz for varying widths of bias pulse of 60 V (see Fig. 22). As seen in Fig. 22, the measurements corresponding to the shorter widths of the bias pulse, ranging from 300 µs to 3 ms, show the same shape, indicating the absence of ion migration. A different shape of CWF appears for widths of bias pulses above 3 ms, which may be ascribed to the bias-induced ion migration. In the case of wider pulses than 3 ms, the hysteresis effects appear and CWF shape starts to depend on the time of applied pulsed bias (see 30 ms and 30 ms later in Fig. 22). Interestingly, at longer times of 30 ms pulse bias application, the charge carrier collection efficiency improves, as manifested in Fig. 22 by the larger area under the later measured CWF. Similar hysteresis behaviour under DC applied bias was observed in MAPI single crystals in Fig. 21.

Note that within the first ~3 µs, the rising edge appears in recorded CWFs Fig. 22. This is caused by the limitation of the used pulse generator which enables us to set ~3 µs as the smallest possible width of the laser probe pulse.

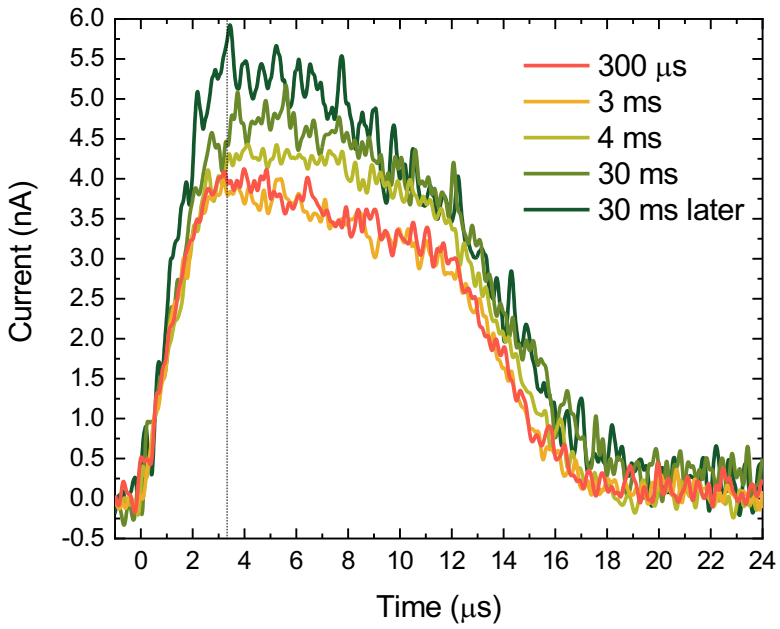

Fig. 22: The dependence of hole CWFs on the width of applied bias pulse in MAPB single crystals. Measured by L-TCT using 60 V pulsing bias with frequency of 5 Hz and delay time of 100 µs.

Based on measurements in Fig. 22, the frequency of 5 Hz and bias pulse width of 1ms is sufficient in suppressing hysteresis effects from ion migration and was therefore selected in all following L-TCT measurements on perovskites.

To estimate effective mobility and mobility-lifetime product, we measure transient currents on MAPB single crystals for different biases on the sample (see Fig. 23a). As expected, the transient time is shortened with increasing applied bias. This is a consequence of the fact that charge carrier drift velocity is directly proportional to the applied electric field. An initial slight increase of CWFs seen mostly at low biases corresponds to the plasma effect. However, to maintain a good signal-to-noise ratio of CWFs, further probe pulse intensity lowering to remove the plasma effect [90] wasn´t appropriate.

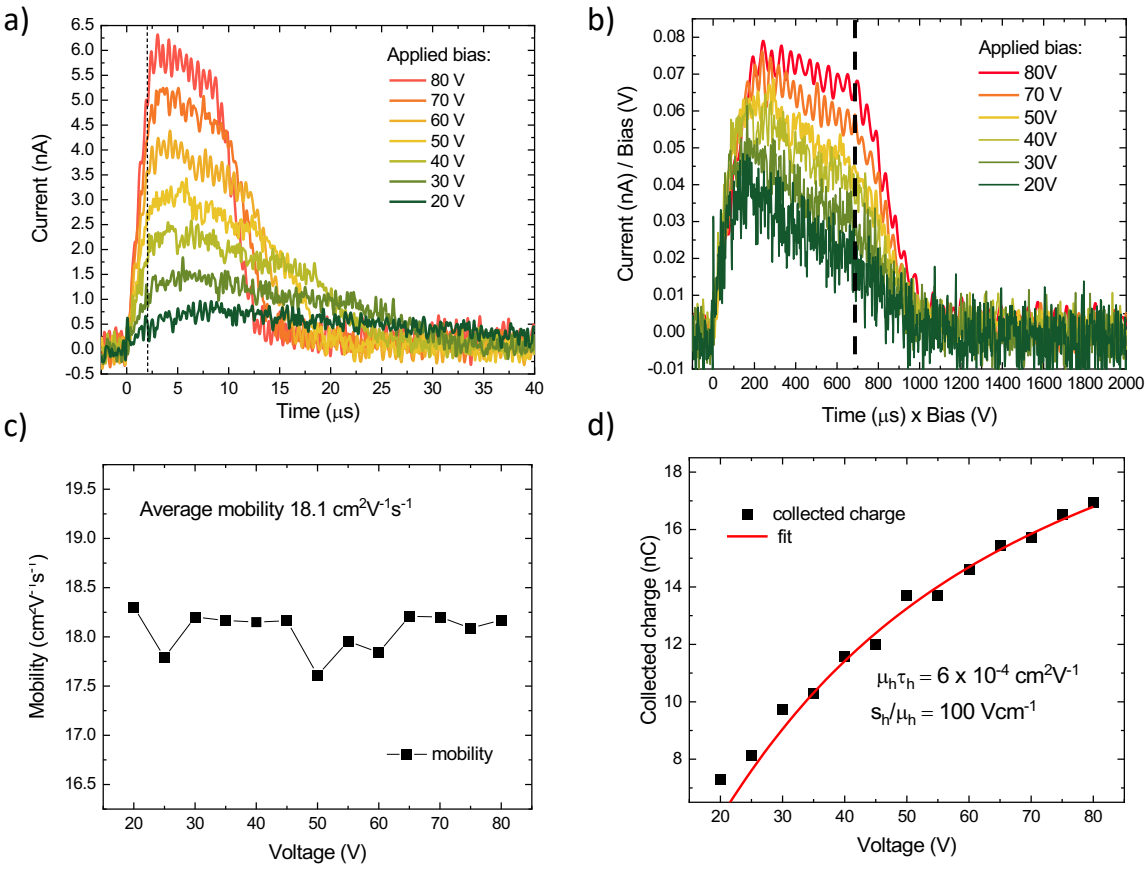

Fig. 23: L-TCT measurement on MAPB single crystals: a) bias dependence of transient currents; b) bias-normalised transient current waveforms; c) mobility calculated according to eq. (3.1), d) charge collection efficiency

From the normalised CWFs, where we multiply the horizontal time axis and divide the vertical current axis by the corresponding bias for each curve, one can deduce whether the internal electric field is distorted by space charge formation. Such a deformed electric field should prolong the transit time to a different extent at different biases. Thus, the individual transit time and bias products, $t_r(U) \cdot U$, should acquire different non-constant values in a semiconductor with considerable space charge. However, in Fig. 23b, the transit time and bias product, $t_r(U) \cdot U$, shows the same constant value, marked with a dashed line. This indicates an almost uniform distribution of internal electric field with no significant deformation by formed space charge. Interestingly, the curves are not exactly at the same height even after dividing the vertical current axis by corresponding bias. This may be explained by strong surface recombination, which competes with charge carrier harvesting and is more significant at lower biases.

Considering a homogenous internal electric field profile, one can easily calculate hole mobility for individual biases according to eq. (3.1). The thickness of the measured sample of 1.6 mm was used in calculations. An average hole mobility is 18 $cm^2V^{-1}s^{-1}$ (Fig. 23c). Fitting bias dependency of CCE, obtained from integration of CWFs, by modified Hecht equation (3.13), one can obtain hole mobility-lifetime product $\mu_h\tau_h$= 6 x 10^{-4} cm^2V^{-1} and s_h/μ_h = 100 $V \cdot cm^{-1}$ (Fig. 23d). The corresponding hole lifetime is $\tau_h = 33$ µs and surface recombination velocity s_h = 1800 $cm \cdot s^{-1}$. A small deviation of the fit by eq. (3.13) at lowest voltages may be given by the memory effect from previous measurements. Nevertheless, the evaluated μ_h= 18 $cm^2V^{-1}s^{-1}$, and $\mu_h\tau_h$= 6 x 10^{-4} cm^2V^{-1} are in good agreement with $\mu_h \sim$ 15 $cm^2V^{-1}s^{-1}$ and $\mu_h\tau_h \sim$ 10 x 10^{-4} cm^2V^{-1} obtained in [128], [129].

5.3 Influence of continuous illumination on MAPB transport

To study the influence of above-bandgap illumination, we perform similar measurements on MAPB single crystal as before on CZT in Fig. 16. We compare the L-TCT signal without additional LED illumination and with continuous LED illumination. Used LED has a wavelength of 465 nm and intensity of 450 $\mu W.cm^{-2}$. Here, probe pulses and continuous LED are incident on the anode side of the measured sample. We thus collect, as in section 5.2, hole signals. Comparison of CWFs for selected biases 30 V and 60 V are shown in Fig. 24. As can be seen from a comparison of the area under individual CWFs with and without illumination, the charge carrier collection efficiency has improved under illumination.

An improved charge carrier collection can be explained by light-induced suppression of surface recombination or by charge carrier lifetime or mobility enhancement. Clear evidence that surface recombination is optimized by continuous illumination may be seen from bias-normalized current waveforms, when we divide both axes, horizontal and vertical, by corresponding biases. As can be seen in Fig. 25a, individual bias-normalised CWFs that were recorded in the dark have significantly different amplitudes. This is a sign of substantial surface recombination. On the contrary, for CWFs obtained under continuous illumination (Fig. 25b), normalized curves more overlap, which indicates that surface recombination is almost completely supressed.

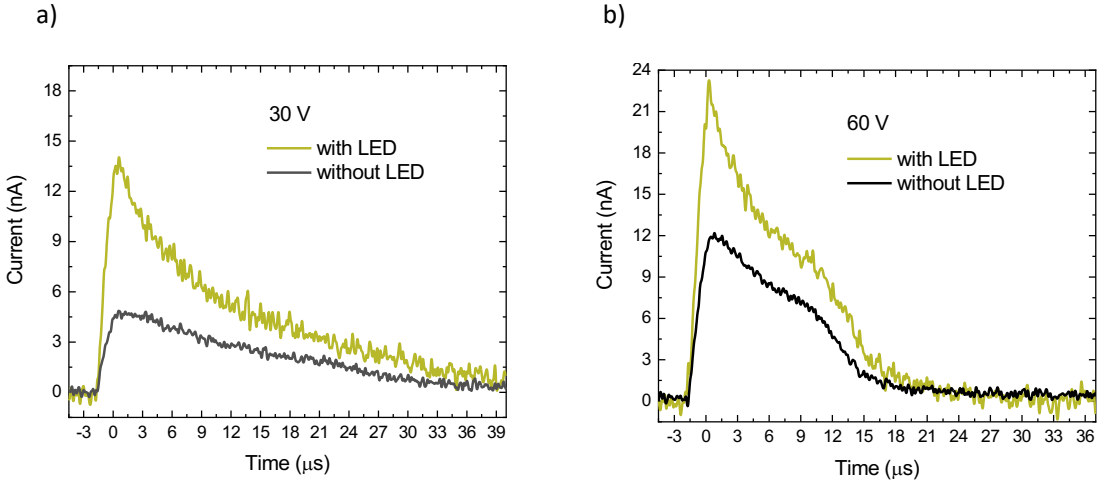

Fig. 24: Hole CWFs measured on MAPB single crystal by L-TCT using laser pulses only (black line) and with additional continuous LED illumination 465 nm (green line) for voltage a) 30 V and b) 60 V.

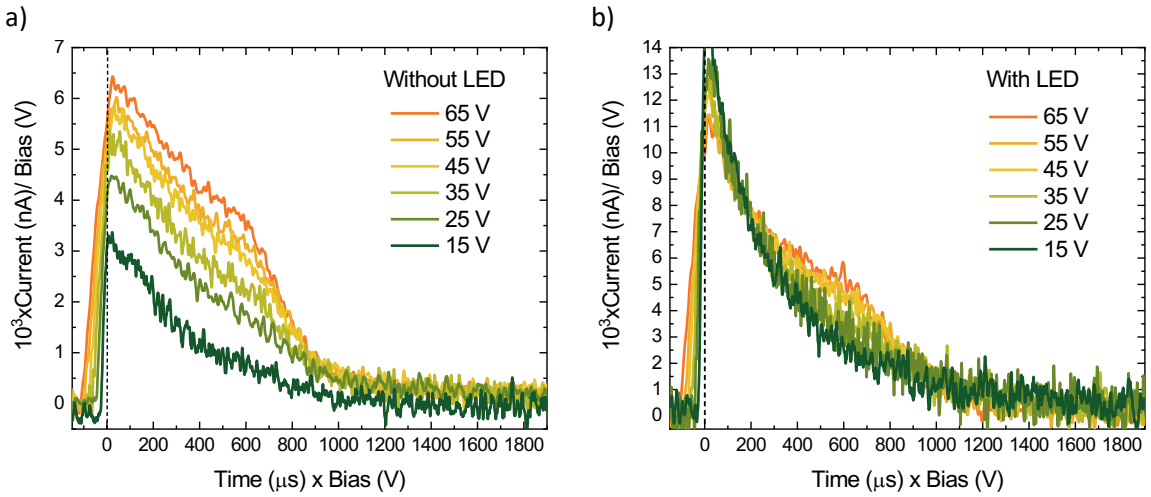

Fig. 25: Bias-normalised hole CWFs measured on MAPB single crystal by L-TCT a) using laser pulses only and b) with an additional continuous LED illumination 465 nm at different applied biases.

Optimization of surface recombination may be explained by the following mechanism shown schematically in Fig. 26. Continuous LED illumination creates electron-hole pairs. Electrons have approximately twenty times shorter lifetime than holes in MAPB perovskites [127]. Photo-generated electrons are therefore most probably trapped near the anode as they are subjected to much stronger trapping compared to holes and photo-generated holes drift toward the cathode. Negative space charge from trapped photo-electrons remains close to the anode and influences the electric field profile as depicted in Fig. 26b by the red line. Close to the illuminated anode, we get a higher electric field, due to which we eliminate surface recombination.

Negative space charge below the illuminated anode may also originate from the accumulation of negatively charged bromine interstitials Br_i^-, which most probably migrate in perovskites due to their low activation energies for the migration [33] and whose formation may be supported by additional LED illumination.

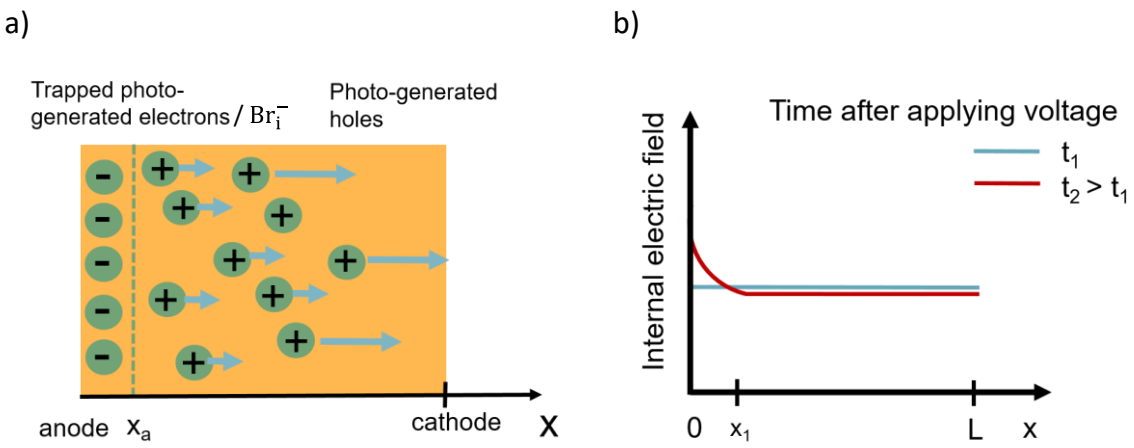

Fig. 26: Scheme of surface recombination optimization phenomena induced by light. a) negative space charge formation and b) change of internal-electric field under illumination. Negative charge below anode may result also from light-induced negatively charged defects.

The exact influence of light on charge carrier transport properties is not so obvious from Fig. 24, as the exponential decay factor *c* of CWFs strongly depends not only on carrier lifetime τ but according to equations (3.4)-(3.6) also on formed space charge. A negative space charge from trapped photo-generated electrons, which is formed close to the anode, contributes to the steeper exponential decline of CWFs after illumination. The effect of a negative space charge may be suppressed after switching off the continuous LED illumination when new photo-generated electrons are not created anymore and previously trapped electrons are released from traps. In Fig. 27, we compare the evolution of CWFs after switching off continuous LED illumination to the CWF measured on fresh sample before any illumination. Interestingly, we observe a milder exponential decay in the previously light-soaked sample than in the fresh sample. Such milder exponential decay accompanied by the improved charge carrier collection efficiency may be explained by hole lifetime improvement under illumination. As seen in Fig. 27, the light-induced improvement in hole lifetime is not permanent. It seems to persist for several minutes, even hours after switching off the illumination. On the contrary, the effect of a negative space charge disappears much quicker, which enables us to observe the real influence of light on transport properties without parasitic space charge influence.

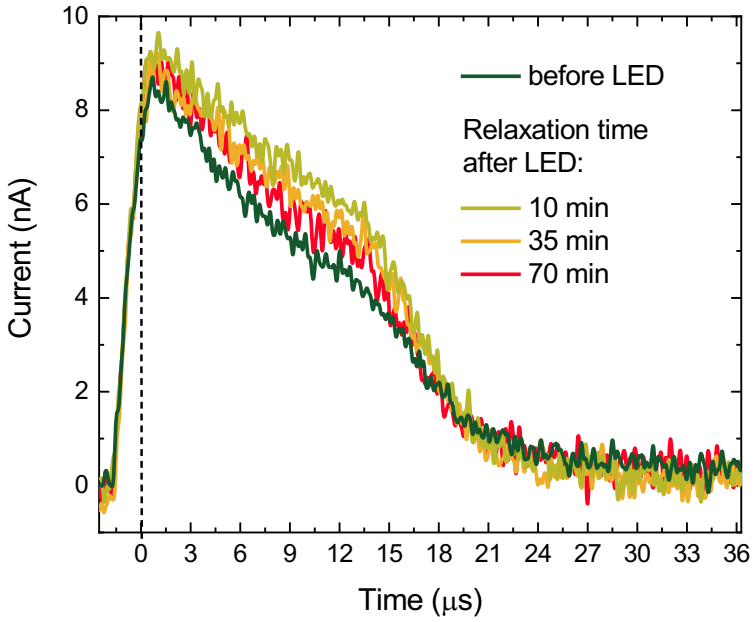

Fig. 27: Evolution of hole CWFs after switching off continuous LED illumination with intensity of 450 μW.cm^{-2}. Measured at pulsed applied bias of 45 V on MAPB single crystal.

An improved hole lifetime under illumination may originate from two mechanisms. The first one is based on hole trapping. As shown in schematic Fig. 28, the perovskite sample contains before illumination a hole trap level E_T below the Fermi energy level. This defect level traps holes and shortens their lifetime. After illumination, the Fermi energy level may be shifted downward, closer to the valence band, so that trap level E_T gets above the new Fermi energy level. As a consequence, holes are not trapped by this trap level E_T anymore and hole lifetime increases.

The second possible mechanism that may lead to the hole lifetime improvement consists of a chemical reaction. The light may produce new positively charged defects, which can passivate hole trap defects and thus increase hole lifetime.

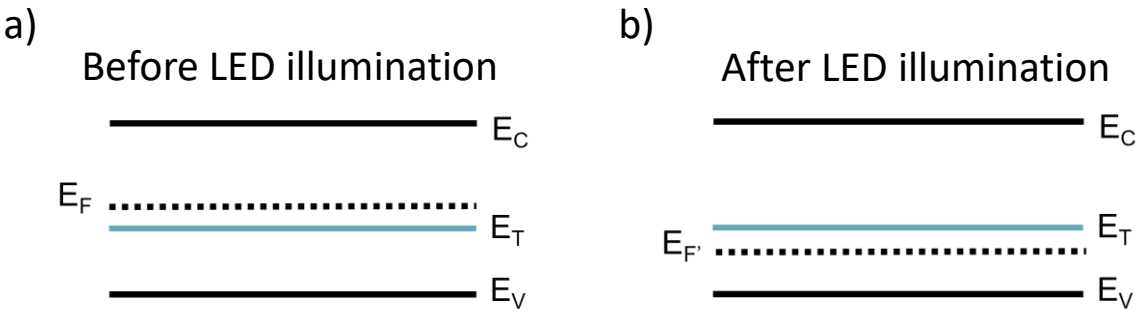

Fig. 28: Mechanism of carrier lifetime optimization phenomena induced by light. a) energy level diagram before LED illumination and b) energy level diagram after LED illumination. E_C denotes conduction band, E_F Fermi energy level, E_T hole trap level and E_V valence band.

We further measure PV characteristics on MAPB single crystals under anode continuous above-bandgap illumination while the pulsed bias regime is used to suppress ion drift under applied bias (see section 3.2). To evaluate photocurrent, a dark current response to bias pulse is first recorded and then subtracted from the current response to bias pulse measured under simultaneous continuous illumination (see Fig. 29). A typical steep decrease in current responses to 1 ms bias pulse within the first ~50 µs is given by RLC phenomenon (see Fig. 7).

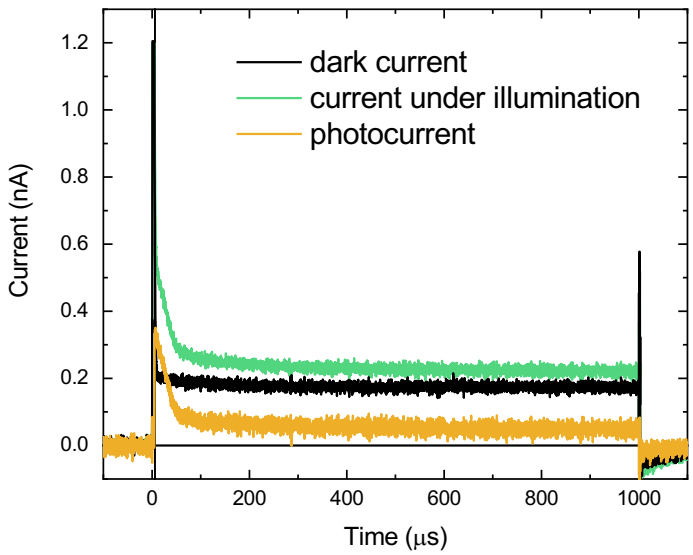

Fig. 29: Evaluation of photocurrent from measured current responses to 20 V bias pulse with 1 ms width and 5 Hz frequency.

As can be further seen in Fig. 30a, the dark current response does not change during the measurement time after applying a series of 1 ms bias pulses with 5 Hz frequency. However, in Fig. 30b we observe several hysteresis in individual current responses under continuous illumination, which were measured at different times after applying 5 Hz bias pulses. The most significant evolution of the current response is visible at longer times (~400 µs) of one applied bias pulse. The rise in current may be explained by the light-induced formation of Frenkel pairs of bromine interstitials Br_i^- and bromine vacancies V_{Br}^+. Br_i^- subsequently migrate under bias pulse to the illuminated anode where they form after ~400 µs negative space charge and thus locally increase the internal electric field (Fig. 26b). Higher electric field near the anode reduces the surface recombination and hence improves carrier collection which is manifested by an increase in currents. During a further 199 ms when applied bias is zero (Fig. 6), the accumulated Br_i^- diffuse back from the anode region to the sample bulk, which returns the surface recombination rate to the previous value. The substantial negative space charge decreasing surface recombination will be again created after ~400 µs of the next bias pulse. As Br_i^- are created by light, the phenomenon will be most visible at longer times of measurement under continuous illumination when the density of light-induced Br_i^- is highest.

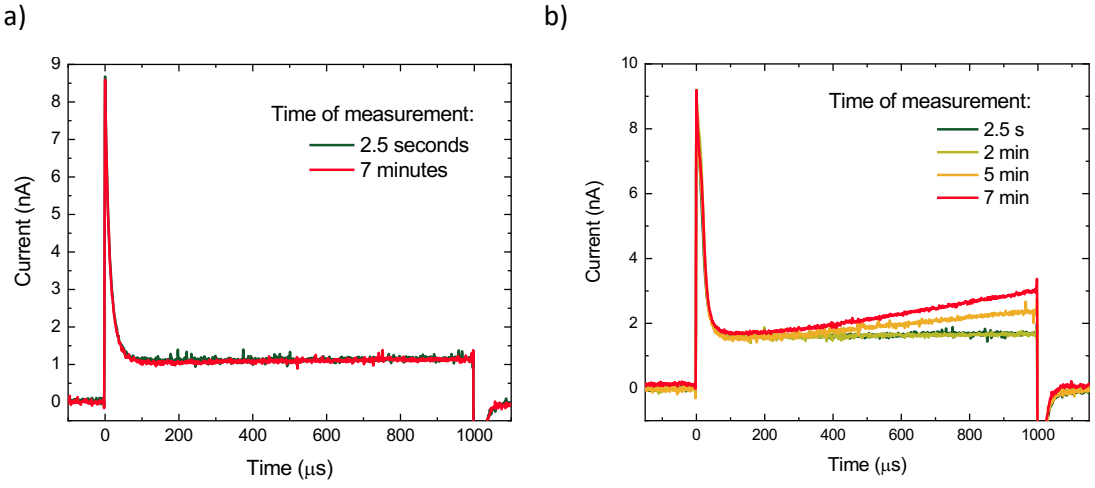

Fig. 30: Current responses to 70 V bias pulse with 1 ms width and 5 Hz frequency. a) Evolution of dark currents upon measurement time after applying bias pulses, b) evolution of currents under continuous above-bandgap illumination upon measurement time after applying bias pulses.

The resulting PV characteristic at varying biases is then given by photocurrent values obtained at one chosen time of applied bias pulse. The previously used models (Many´s, SCLP1, SCLP2, and DDF model) do not consider the contribution of ion conductivity, or ion-induced space charge, and therefore, a detailed analysis of PV characteristic obtained for longer times after applying the bias pulse will not meet the assumptions of models. To exclude the effect of light-induced Br_i^- and its space charge from PV characteristic, we chose an early time of 6 μs after applying the bias pulse for the acquisition of photocurrent values at individual biases. The resulting PV characteristic at 6 μs after applying the bias pulse together with fit by the SCLP1 and Many´s model are in Fig. 31.

A significant discrepancy of SCLP1 fit and measured photocurrents at low voltages may arise from negative space charge from trapped photo-electrons. Such negative space charge enhances the electric field under an illuminated anode, improves charge collection and resulting photocurrents. Used SCLP1 model is a single-particle, thus in the case of anode illumination considers only hole conductivity and corresponding positive space charge. The negative space charge is beyond the SCLP1 model assumptions. Formation of substantial negative space charge is possible even for short times of 6 μs, as electrons are estimated to have 20 times lower lifetimes compared to holes [127] in lead-halide perovskites. This also corresponds well to the measured electron CWF in Fig. 21, where the electron signal almost completely disappears after 6 μs. The effect of negative space charge in Fig. 31 disappears at higher voltages, as a higher electric field reduces the trapping probability of photo-generated electrons. Model SCLP1 thus fit PV characteristic in this high-bias region well. Using fixed μ_h = 18 $cm^2V^{-1}s^{-1}$ which was previously obtained from L-TCT measurement in section 5.2, the SCLP1 fit gives us parameter $\theta = 9 \times 10^{-3}$ and s_h = 200 $cm \cdot s^{-1}$. It is necessary to point out that the SLCP1 model is valid in steady-state conditions. The time of 6 μs, however, may not be sufficient for the formation of stable positive space charge from trapped photo-generated holes, and the correctness of using the SCLP1 model may be thus questionable.

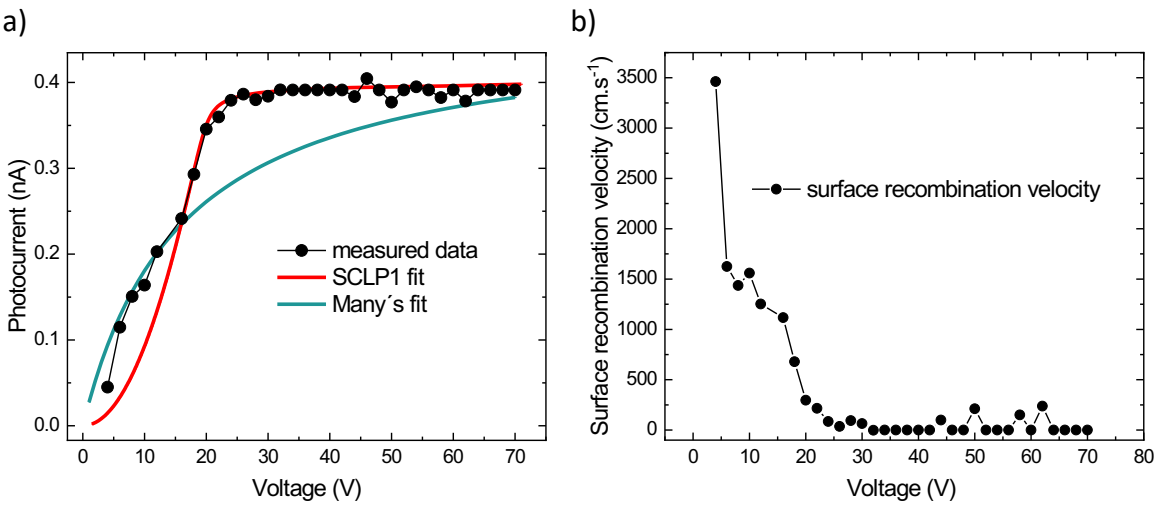

Fig. 31: a) PV characteristic of MAPB single crystal under continuous above-bandgap illumination. Fitted with SCLP1 (red line) and Many´s model (blue line). b) Calculated dependence of surface recombination velocity on bias

The Many´s model, which considers surface recombination and neglects space charge, on the other hand, cannot describe photocurrent saturation as seen in Fig. 31a. The parameters obtained by Many´s fit are $\mu_h\tau_h$= 6 x 10^{-4} cm^2V^{-1} and s_h/μ_h = 10 V·cm^{-1}. The Many´s model assumes constant surface recombination velocity. Therefore, the observed saturation of measured photocurrent may originate in the dependency of surface recombination velocity on the applied bias. We calculated surface recombination velocity for each pair of measured photocurrent-bias according to eq. (2.20) in a limit of the infinite mobility-lifetime product (Fig. 31b). The assumption of infinite mobility-lifetime product is consistent with [126]. In calculations, we used mobility μ_h = 18 $cm^2V^{-1}s^{-1}$ and the maximal photocurrent value (~ 0.4 nA) as J_0. As seen in Fig. 31b, for biases higher than 25 V, the surface recombination velocity drops to zero values. Such bias-dependent suppression of surface recombination explains the saturation of measured photocurrents above 25 V.

5.4 Influence of prolonged illumination on MAPB transport properties

We study the effect of light-soaking on perovskite transport properties by L-TCT. The sequence used for LS measurements is shown in Fig. 32. We illuminate the anode of the sample by laser diode with an above-bandgap wavelength of 465 nm and intensity corresponding to the one sun.

Fig. 33a shows the development of hole transient currents with increasing time of illumination. Since the area under the CWF corresponds to the collected charge, we can conclude that the charge carrier collection increases after light exposure. The increase in charge carrier collection saturates after 120 minutes after illumination. Another interesting feature is the rapid current drop which is most visible on the sample without previous illumination at the start of CWF (see dashed circle). The rapid current drop gradually disappears as we prolong the steady-state illumination time.

To study the reversibility of light-induced changes, we periodically illuminate the sample for 250 min, switch off illumination and after 15 hours of storing the sample in the dark we again record CWF. We repeat this three times. As seen in Fig. 33b, the same shape of CWF is obtained repeatedly, however, it differs from the CWF measured for the first time on the pristine perovskite. Light-induced changes are thus almost reversible. The main difference compared to pristine CWF lies in the disappearance of rapid current drop and the slight improvement of charge carrier collection.

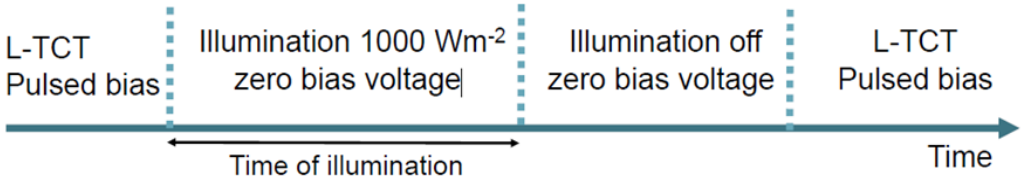

Fig. 32: Sequence used for L-TCT measurements to study the effect of prolonged illumination.

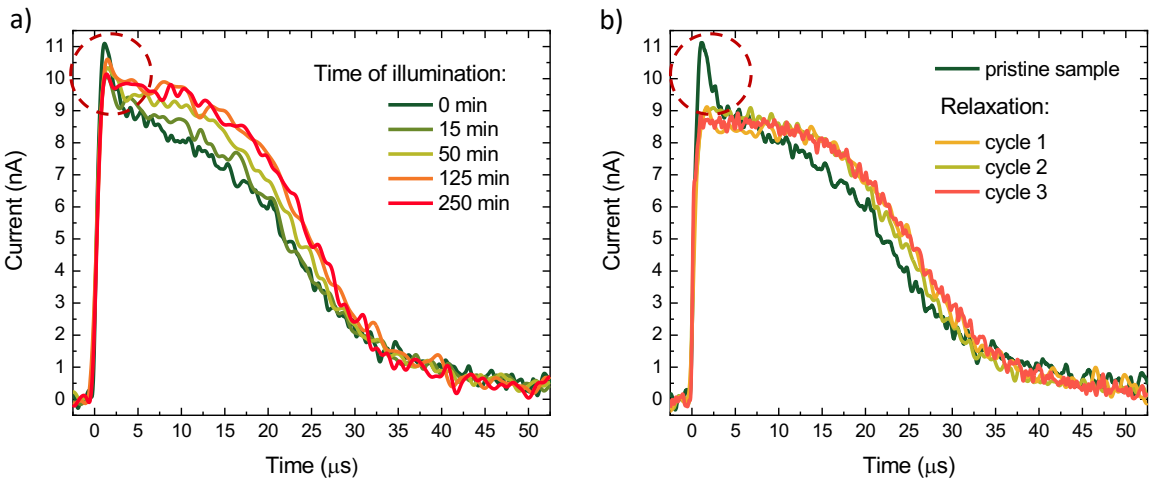

Fig. 33: a) Evolution of hole CWFs under 1 sun illumiantion. b) Relaxation of CWFs after swithing off illumination. Each cycle consists of previous LS for 250 min and subsequent 15 hours relaxation in the dark. Measured on MAPB single crystal at 5 Hz pulsed bias of 10 V and delay time of 300 μs.

To correlate light-induced changes with deep defects evolution, we measure absorptance spectra by photo-thermal deflection spectroscopy (PDS). Used wavelength and intensity of illumination are the same as in the previous L-TCT measurement. As seen in Fig. 34, the absorptance spectra for pristine perovskite are quite similar to the spectra measured after sample storage for 67 hours in air conditions. However, even 10 min of continuous LED illumination leads to a substantial increase in the sub-bandgap region. This corresponds to the formation of deep defect levels under illumination.

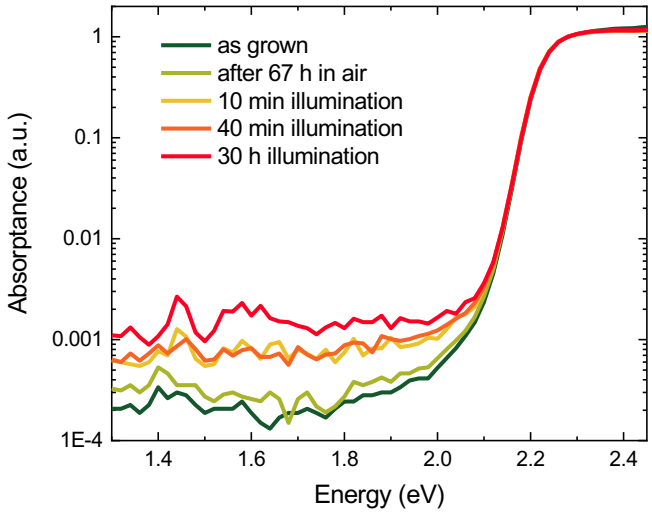

Fig. 34: Evolution of absorptance spectra under 1 sun illumination measured by photo-thermal deflection spectroscopy.

The observed phenomena by L-TCT and PDS, especially the increase in sub-bandgap absorption and the disappearance of rapid transient current drop observed in L-TCT may be explained by the following mechanism. The material may contain complex defect, which under the influence of light disintegrates into other defects. Therefore, the rapid current drop that is connected to this complex trap disappears in CWF under illumination. The complex defect probably acted as a stronger recombination centre compared to new defects. Its extinction therefore prolongs the lifetime of holes, leading to an increased charge carrier collection under illumination. Increased sub-bandgap absorption under illumination observed in PDS is then given by the contribution of new trap levels. Saturation of charge carrier collection efficiency after 125 minutes of illumination is given by finite concentration of complex defect.

An equivalent explanation of a rapid current drop disappearance accompanied by an increase in deep defect density may be explained by the light-induced formation of deep defects which passivate a strong recombination centre corresponding to a rapid current drop. The light-induced deep defects most probably correspond to the Frenkel pairs of bromine interstitials and vacancies due to their low formation energies.

5.5 Conclusion: Lead halide perovskites $APbX_3$

We studied the transport properties of perovskite single crystals with emphasis on light-induced changes. The CWFs of single crystals show strong hysteresis effects under DC bias which we attributed to ion migration under applied bias. To prevent ion migration and subsequent space charge formation causing dead layer, we found suitable bias pulse parameters. Assuming homogenous internal electric field and Hecht equation (3.11) we obtained from L-TCT measurements on MAPB single crystals under pulsed bias regime a mobility-lifetime product of 6×10^{-4} cm^2V^{-1}, hole mobility of 18 $cm^2V^{-1}s^{-1}$ and lifetime of 33 µs. Bias-normalised CWFs suggest strong surface recombination in MAPB perovskites. Further, the effect of continuous above-bandgap illumination on transport properties was studied. Combining L-TCT measurements with and without continuous illumination, we observe a light-induced improvement in charge carrier collection. The improvement was proved to stem from

two effects, reduced surface recombination and increased hole lifetime. The suppression of surface recombination under illumination was attributed to the local increase of internal electric field under illuminated anode due to the negative space charge from trapped photo-electrons or accumulated Br_i^-. The light-induced hole lifetime improvement originates possibly from the shift of the Fermi energy level downward, leaving the previous hole trap level above the new Fermi energy level. Secondly, light-induced hole lifetime improvement may consist of the formation of new defects, which passivate hole trap defects. The evolution of the current response to a 1 ms bias pulse with 5 Hz frequency during the time of measurement under continuous illumination suggests the formation of mobile Frenkel pairs by light. Accumulation of light-induced Br_i^- under an illuminated anode locally increases the electric field and thus improves charge collection at longer times of applied bias. The light-soaking of MAPB leads, similarly as in the case of short-term illumination, to an almost reversible improvement in charge collection efficiency. An observed gradual disappearance of a rapid current drop in CWFs under LS, we attributed to the passivation of a strong recombination centre by new light-induced defects or to the disintegration of a strong recombination centre into new defects. The formation of new light-induced deep defects was proved via PDS by an increase in sub-bandgap absorption under LS.

6. Phase segregation in mixed-halide perovskites

This section focuses on the so-called phase segregation of mixed-halide perovskites into I-rich and Br-rich domains (see section 1.4). We perform this study on $FA_{0.83}Cs_{0.17}Pb(I_{0.6}Br_{0.4})_3$ perovskites, which have a slower phase segregation rate compared to $MAPb(I_xBr_y)_3$ [29], [78], [130]. This enables us to precisely record the evolution of phase segregation, including its onset.

Samples are prepared as solar cells with electron and hole transport layers that enable us to directly measure FTPS spectra without applying external bias. The structure of the measured n-i-p solar cells together with a typically measured J-V curve and average photovoltaic parameters of pristine solar cell are in Fig. 35. Light-soaking of cells was done using a continuous Xe lamp A1020 from AMKO adjusted to 1000 W/m^2 in one of three modes: at open-circuit (OC), short-circuit (SC) or maximum power point (MPP). The LS sequence, used for J-V, PL, and FTPS measurements, is shown in Fig. 35b. All times stated in the thesis are cumulative. Individual measurements between LS times took a maximum of five minutes and were measured directly after switching off the illumination. For each LS sequence, we use a new pristine sample. The used perovskite composition is indirectly confirmed via XRD measurement of lattice parameters (see section 6.3).

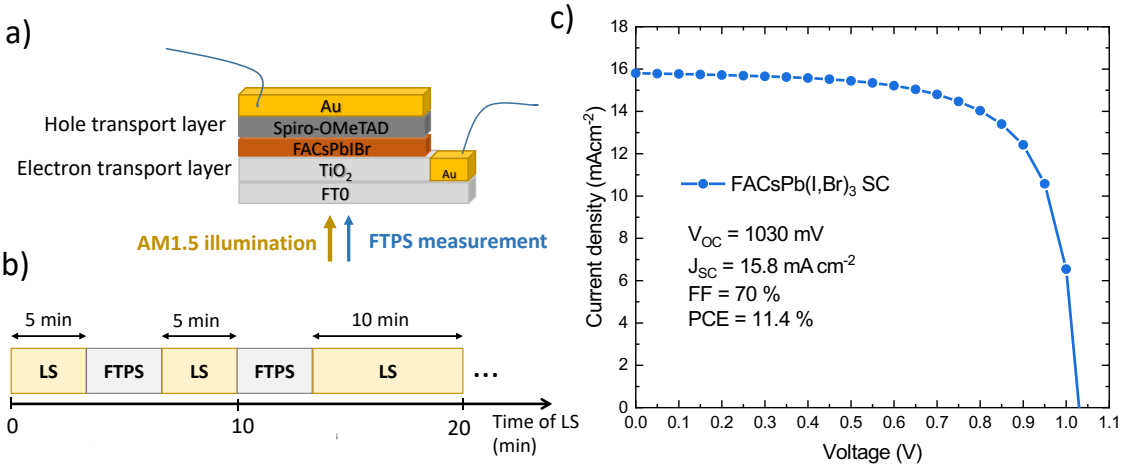

Fig. 35: a) Scheme of studied solar cell device, b) scheme of measurement LS sequence, c) J-V data measured on $FA_{0.83}Cs_{0.17}Pb(I_{0.6}Br_{0.4})_3$ solar cell together with photovoltaic parameters.

6.1 IV characteristics and PL spectra evolution upon LS

First, we compare the evolution of the solar cells´ J-V parameters under standard AM1.5G illumination [131] at OC, SC, and MPP working conditions followed by a relaxation in the dark (Fig. 36). Various working conditions are tested to study the role of excited charge carriers in segregation. In all regimes, there is an overall decrease in photovoltaic parameters during LS. Note that we observe an occasional performance improvement during the first 5 minutes of LS. The light-induced drop in V_{OC}, J_{SC}, fill factor (FF), and power conversion efficiency (PCE) is least pronounced when the cell is light-soaked at SC. Under SC condition, photo-generated carriers are mostly extracted to the contacts, the current density reaches its maximum and the recombination probability within the device is reduced. Conversely, at OC, no net current is flowing out of the device, so all photo-generated carriers recombine. The excess energy released during non-radiative recombination of photo-generated electron-hole pairs may lead to the creation of lattice defects [132], [133]. Such defects may act as new recombination centres, deteriorating photovoltaic parameters Voc [134], and FF [81]. A higher rate of defect formation at OC compared to SC, due to the higher number of excess carriers at OC, may then explain the more significant changes in photovoltaic parameters during OC. Besides changes in photovoltaic parameters, the light-induced defects may enhance phase segregation.

The V_{OC} decrease during LS is probably dominated by the formation of light-induced deep defects. This corresponds well with detailed-balance calculations in [134] and the observation in [135] that suppressing the PL redshift during illumination did not translate into significant gains in V_{OC}. The J_{SC} is seen to decrease substantially upon LS, which may indicate a reduced charge carrier extraction efficiency [136]. This large loss in J_{SC} supports the claims that only a small fraction of the material segregates to a lower bandgap [137] (otherwise J_{SC} would increase upon LS if the system would simply transform to a lower bandgap material without additional effects). After approximately 40 min of LS, the FF saturates at ~ 60%, indicating the presence of a second stabilizing process, similar to Ref. [138].

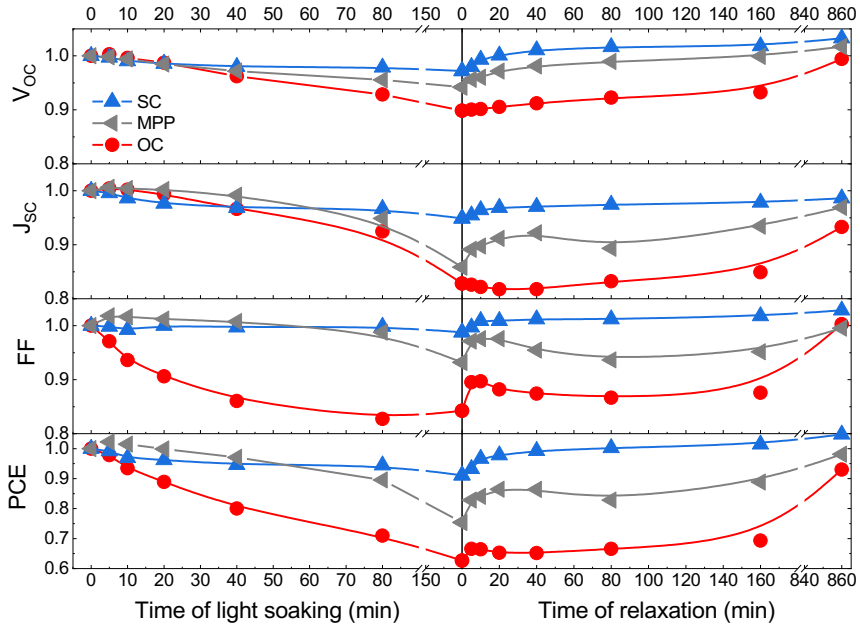

Fig. 36: Evolution of normalised photovoltaic parameters extracted from J-V curves measured under 1-sun illumination and during relaxation in the dark. From the top open-circuit voltage, short-circuit current, fill factor and the power conversion efficiency are illustrated, respectively. Solar cells were held at either open-circuit, short-circuit or MPP condition during light-soaking.

As seen in Fig. 36, a subsequent relaxation in the dark leads to a gradual recovery of the photovoltaic parameters for all LS conditions, and interestingly, for the case of short-circuit LS conditions, even to a slight improvement of parameters compared to the initial state. In contrast, a slightly lower V_{OC}, J_{SC}, and PCE compared to the initial state were found after one-day recovery for the cells LS at OC regime. Irreversibly deteriorated photovoltaic parameters after several hours of relaxation in mixed-halide perovskites with MA, FA cations were previously explained by migration or volatilisation of organic cations and halides [139].

The phase segregation process can be observed by tracking the PL spectra evolution upon LS. Even a small fraction of segregated material (~1%-10%) may be recorded by PL. This results from the so-called charge carrier funnelling which represents the accumulation of charge carriers within the lower bandgap I-rich region [140]. The radiative efficiency of minority I- rich region may grow a hundredfold since radiative band-to-band recombination dominates over trap-mediated recombination in case of high carrier densities in perovskite materials [141]. PL emission from lower

bandgap regions may be also enhanced by trap filling due to a local increase in carrier density [142]. Thanks to the above-mentioned phenomena, photoluminescence is often used as the basic tool to probe halide segregation. However it is not a reliable measure of the degradation rate, as well as it doesn´t provide information about the size and composition of segregated phases.

The evolution of the PL spectra upon LS and subsequent relaxation in the dark under OC and SC conditions are shown in Fig. 37. The emission is initially centred on ~1.76 eV. In both conditions, after ~5 min of LS, an additional PL peak appears at around 1.6 eV (red arrows, phase 1). Its intensity increases further with illumination time, comparable to [140], [143], [144], which suggests efficient carrier funnelling to the low bandgap domains.

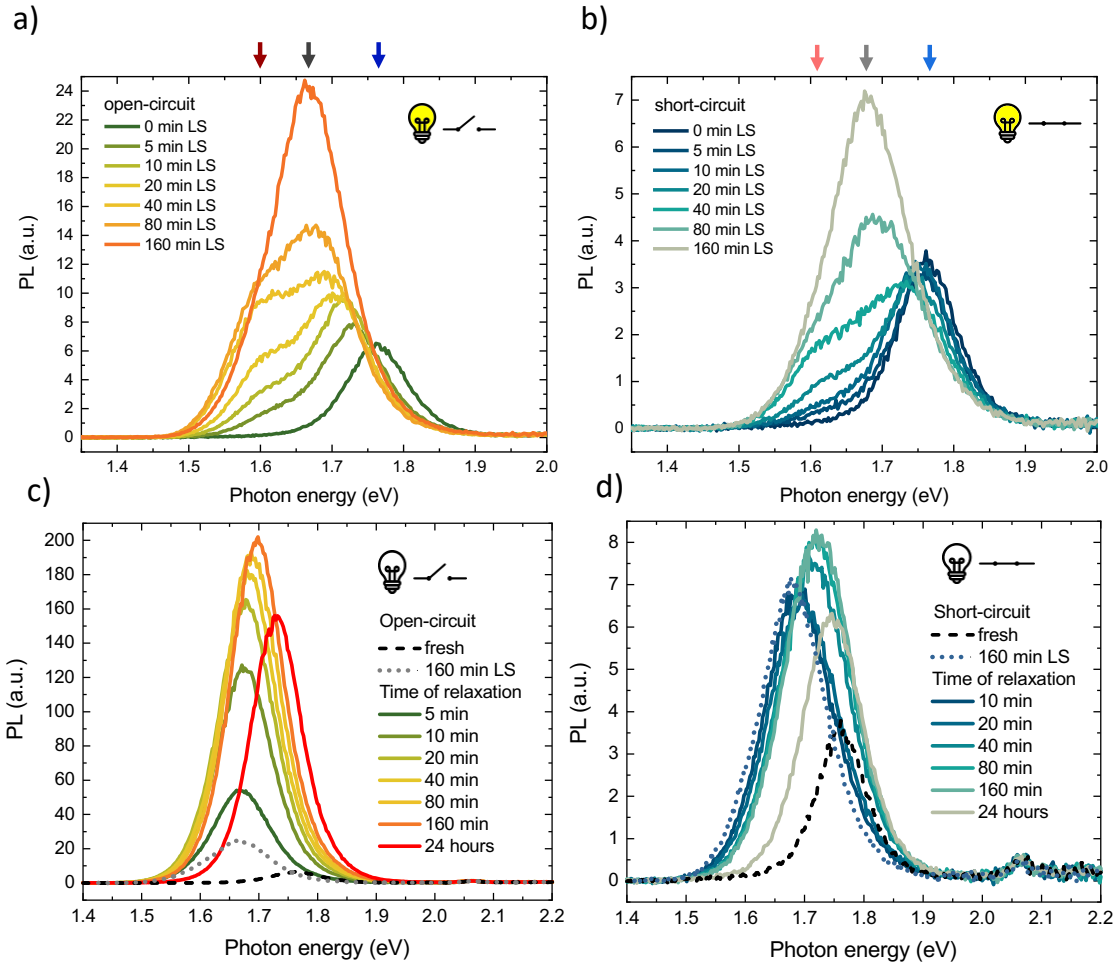

Fig. 37: Evolution of photoluminescence spectra under a 1-sun illumination at a) open-circuit and b) short-circuit condition. Evolution of photoluminescence spectra measurements during relaxation in the dark at c) open-circuit and d) short-circuit conditions.

Both, the newly formed peak (red arrow) and the initial peak at 1.76 eV (blue arrow) which corresponds to the original perovskite composition, show a slight redshift during light-soaking. Shifts to lower energies could correspond to a lattice relaxation as proposed by Tsai et al. [145]. However, the magnitude in our experimental observations exceeds 50 meV, indicating that lattice expansion alone cannot account for the shift. At the last stages of LS, the photoluminescence of both peaks is overwhelmed by one signal at 1.67 eV (grey arrow, phase 2). This latter peak corresponds to the emergence of a segregated I-rich phase 2, which contains less iodine than the previous I-rich phase 1, represented by a peak marked with a red arrow. Phase 2 must significantly outweigh in concentration phase 1 as it is more visible by PL despite charge funnelling, which favours radiative recombination in phase 1 with the lowest bandgap.

6.2 FTPS evolution upon LS

To investigate light-induced deep defects and their link to phase segregation in $FA_{0.83}Cs_{0.17}Pb(I_{0.6}Br_{0.4})_3$ we turn to FTPS. Measured FTPS spectra recorded at different LS times of cells held at OC, MPP, and SC and upon relaxation can be found in Fig. 38, Fig. 39, and Fig. 40. Additional FTPS measurements confirming the repeatability of the effects discussed below are shown in Fig. 42 and Fig. 44.

As observed in Fig. 38a, after 5 minutes of irradiation, the absorption edge slope decreases and the Urbach energy E_U of the pristine solar cell evolves from ~16 meV to ~22 meV. The width of the Urbach tail indicates compositional inhomogeneity in the perovskite due to phase segregation. After 40 min of LS a new distinct shoulder appears at ~1.58 eV, in line with the low bandgap phase 1 measured by PL in Fig. 37a. After a longer LS duration (>40 min), a feature shoulder at 1.68 eV further emerges, which is most pronounced in the case of LS under OC (see Fig. 38a). This 1.68 eV phase is visible also by PL at the last stages of LS (phase 2).

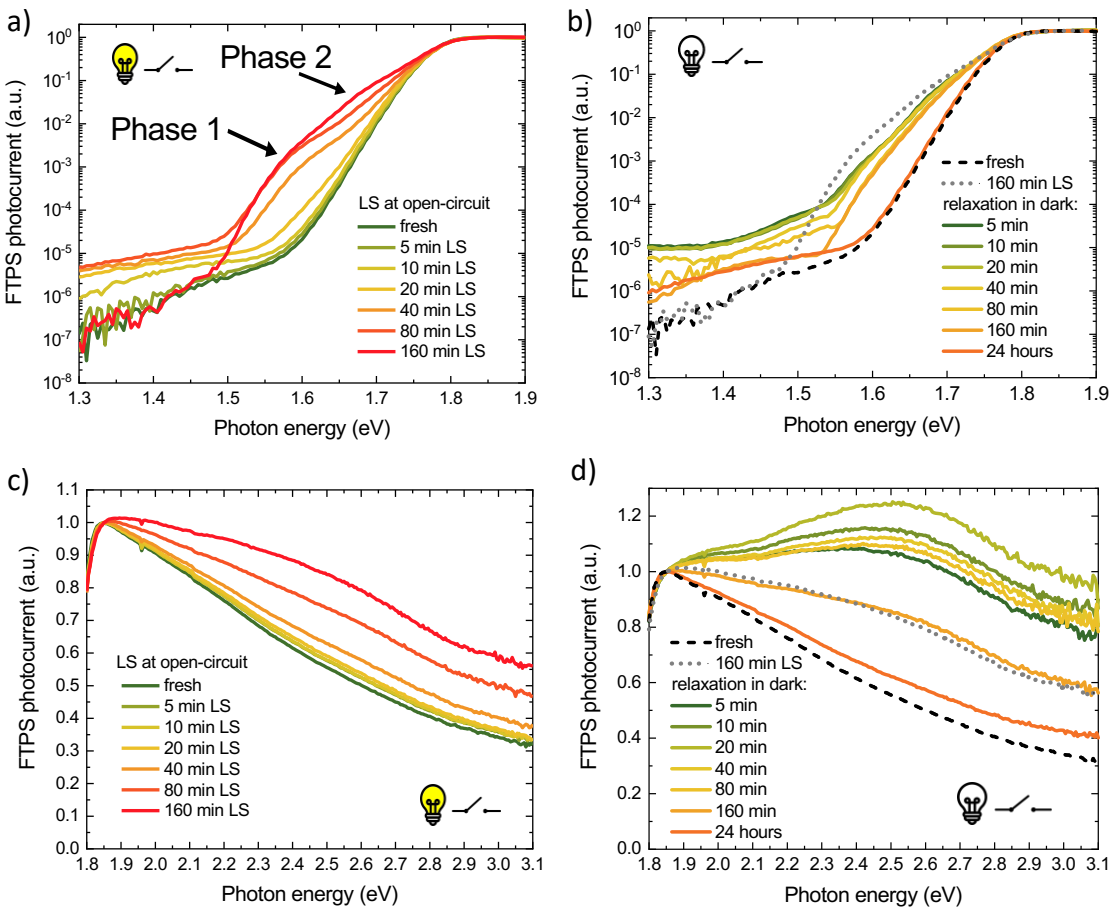

Fig. 38: FTPS showing the effect of 1 sun illumination under open-circuit (on the left) and relaxation in dark (on the right). Spectra are divided into the region of a), b) the sub-bandgap and c), d) above-bandgap absorption.

The exact composition of the segregated phases may be obtained using the reference absorption spectra of Ref. [146] measured on $FA_{0.83}Cs_{0.17}Pb(I_xBr_{1-x})_3$ films with various Br compositions assuming a linear relationship between the bandgap and halide composition. Based on [146], we estimate that the shoulder at ~ 1.58 eV corresponds to an I-rich phase with x=0.9, which is in good accordance with phase segregation measurements in FAMACs mixed-halide perovskites [147]. The shoulder at ~ 1.68 eV suggests a dominant I-rich phase with x=0.8. Our result is thus consistent with previous studies which have reported that independently of the original stoichiometry of mixed-halide perovskites the segregated I-rich domain is characterised by the terminal value x=0.8 [29], [148], [78], [130].

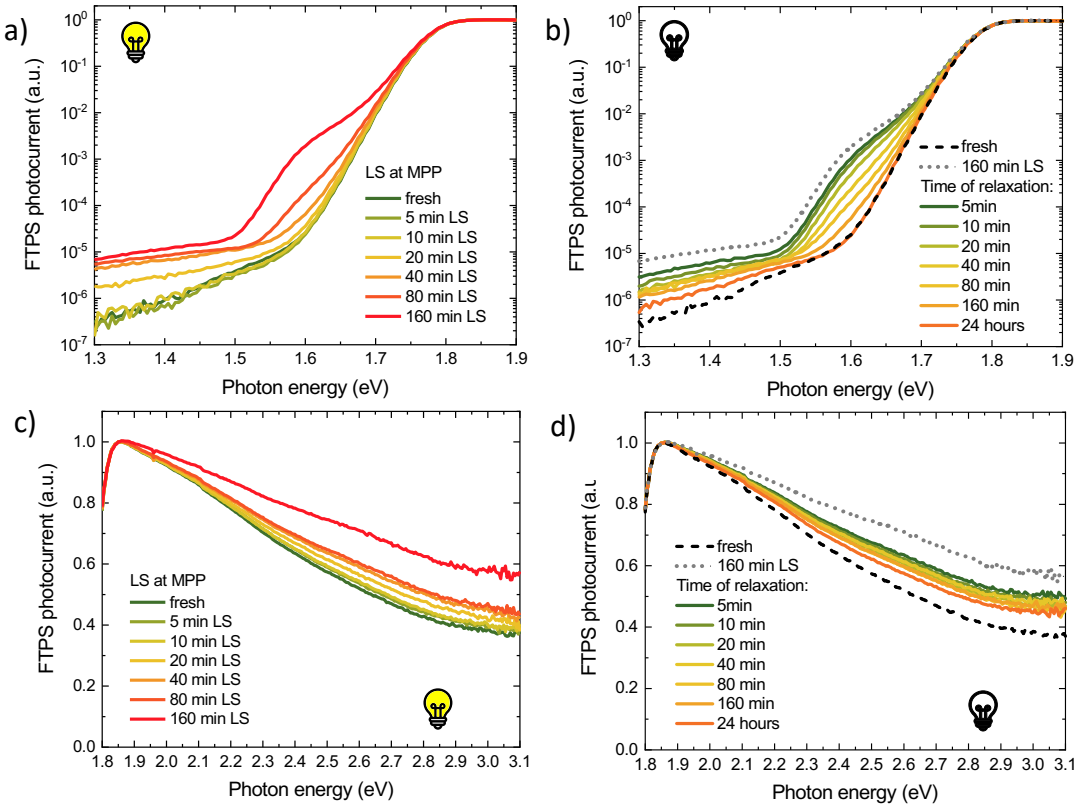

Fig. 39: FTPS spectra evolution under LS at MPP (on the left) and relaxation in dark (on the right). a), b) sub-bandgap absorption and c), d) above-bandgap

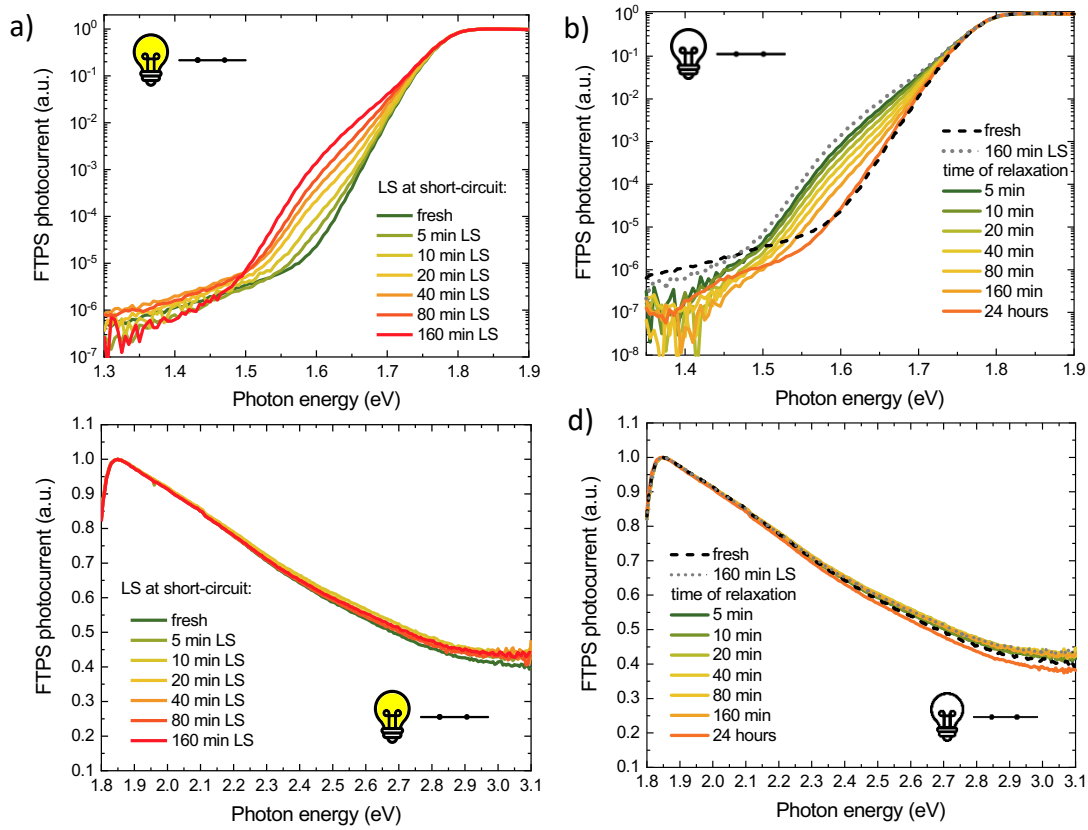

Fig. 40: FTPS spectra evolution under LS at SC (on the left) and relaxation in dark (on the right). a), b) sub-bandgap absorption and c), d) above-bandgap

By deconvoluting FTPS data, we estimate that the domain with x=0.8 (x=0.9) contributes about 10% (0.1%) to the total measured photocurrent at 160 min of LS. The possibility of evaluation of the proportion of segregated phases from FTPS is not a common accomplishment, as most used techniques, PL and X-ray diffraction, are not so reliable in quantity determination due to charge funnelling and strong sensitivity to texture [78], respectively.

The intermediate phase 1, however, has not been observed to form upon LS in $MAPb(I_x, Br_y)_3$. This may result from the fact that phase segregation progresses much quicker in MA-based thin films (within a few minutes) [29], [78], [130] compared to the phase segregation in $FA_{0.83}Cs_{0.17}Pb(I_{0.6}Br_{0.4})_3$ ones. Different segregation rates may be explained by the suppression of halide migration via FA and Cs cations [149], [150].

We suggest that phase segregation generally starts with the formation of the I-rich phase 1 (x=0.9) in all mixed-halide perovskites, but it's quickly overwhelmed in fast-segregating films by the dominating final phase 2 (x = 0.8). We do not observe the intermediate phase 1 in $FA_{0.83}Cs_{0.17}Pb(I_{0.6}Br_{0.4})_3$ thin films, as can be seen in Fig. 41. Phase segregation in thin films has also emerged more rapidly compared to FA, Cs-based whole devices, thereby preventing the intermediate phase 1 from being recorded. This indicates that the contacts also slow phase segregation, probably thanks to reduced recombination and subsequent defect formation due to the charge carrier collection at contacts.

More importantly, we observe in Fig. 38- Fig. 44 that the sub-bandgap photocurrent signal (at photon energies < 1.45 eV) is generally growing in intensity during LS, which suggests the formation of deep levels upon LS. Similarly, to the J-V data, the most significant changes in the sub-bandgap part of the FTPS signal are observed for devices kept at OC during irradiation. This correlates well with the above-proposed explanation that defects are created via the excess energy released during non-radiative recombination in OC conditions, as there is a higher carrier concentration in these conditions.

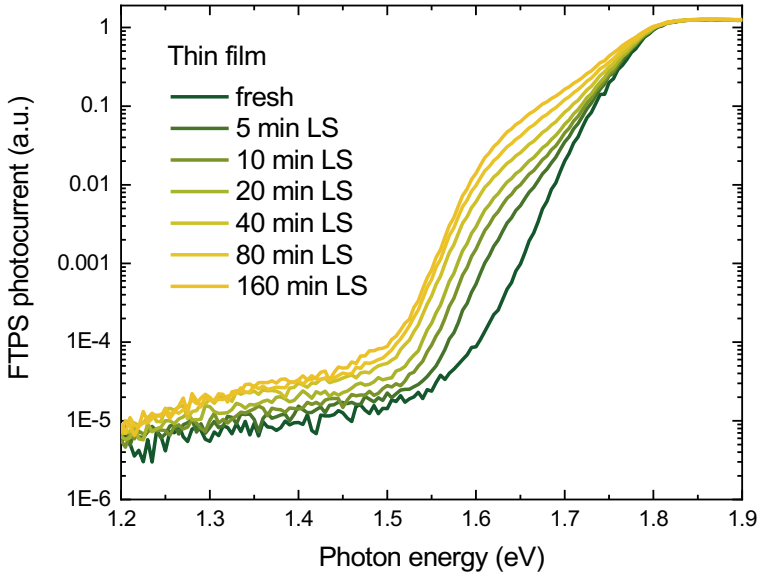

Fig. 41: Evolution of FTPS measured on thin films under continuous AM1.5G illumination. Spectra were measured under applied voltage 100 V.

After an initial trap formation, further illumination leads, in several samples, to a decrease in the FTPS sub-bandgap signal, as can be seen on curves acquired after 160 min of LS in Fig. 38a, and Fig. 42. The decrease observed only in the sub-bandgap part of the FTPS signal cannot originate in a deteriorated charge carrier collection (e.g. due to the creation of a non-radiative-recombination centre) as charge carrier collection evenly affects the entire spectrum, including the above-bandgap signal. The drop in the sub-bandgap photo-current may be therefore assigned to the decrease in deep-level concentration. Such an explanation correlates well with J-V measurements (Fig. 36) performed upon LS at OC, in which the FF slightly improves during the later stages of the LS process.

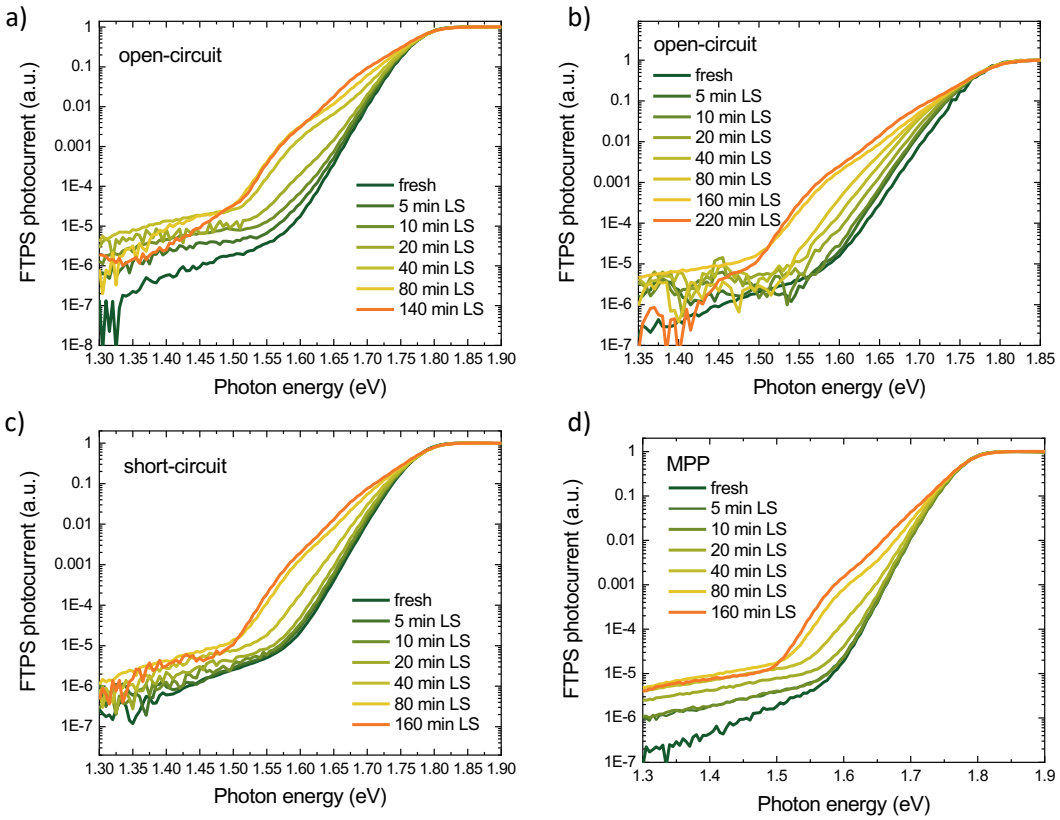

Fig. 42: a)-d) additional FTPS measurements on different $FA_{0.83}Cs_{0.17}Pb(I_{0.6}Br_{0.4})_3$ samples confirming the repeatability of the sub-bandgap signal decrease at longer times of LS, which is accompanied by the formation of the phase 2 with x=0.8.

Some samples, however, do not show any decline in the concentration of deep defects even after a long-term illumination (see Fig. 43 and Fig. 44). Upon extended LS, the deep level concentration only saturates simultaneously with phase 1 (see Fig. 43 and Fig. 45a), while the previously observed final phase 2 with x= 0.8 is not detected in these samples. The sub-bandgap signal decline therefore seems to be associated with formation of the phase 2 with x=0.8. The reason why some samples do not show the commonly observed terminal phase ($I_{0.8}Br_{0.2}$) will be discussed in detail in section 6.6.

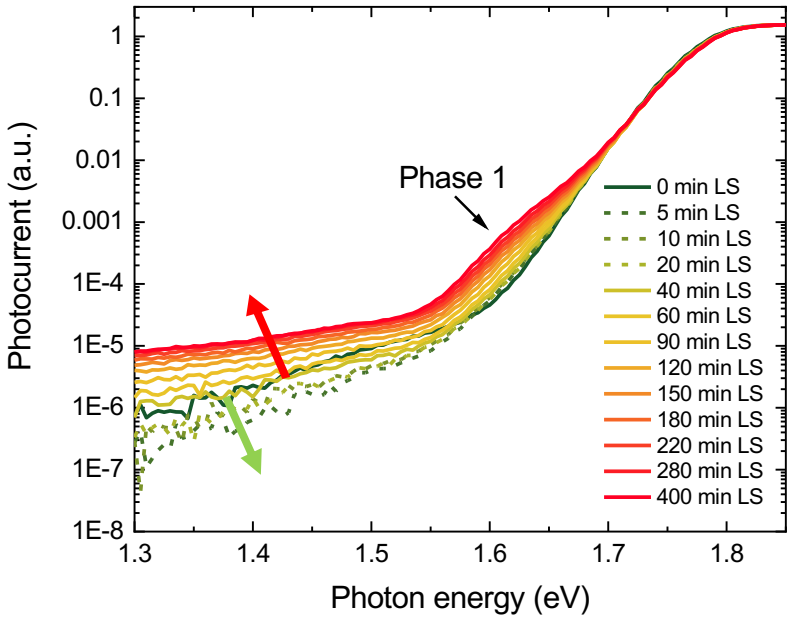

Fig. 43: FTPS showing the effect of 1sun illumination under OC. Measured on sample where phase 2 is not formed even under a long-term illumination.

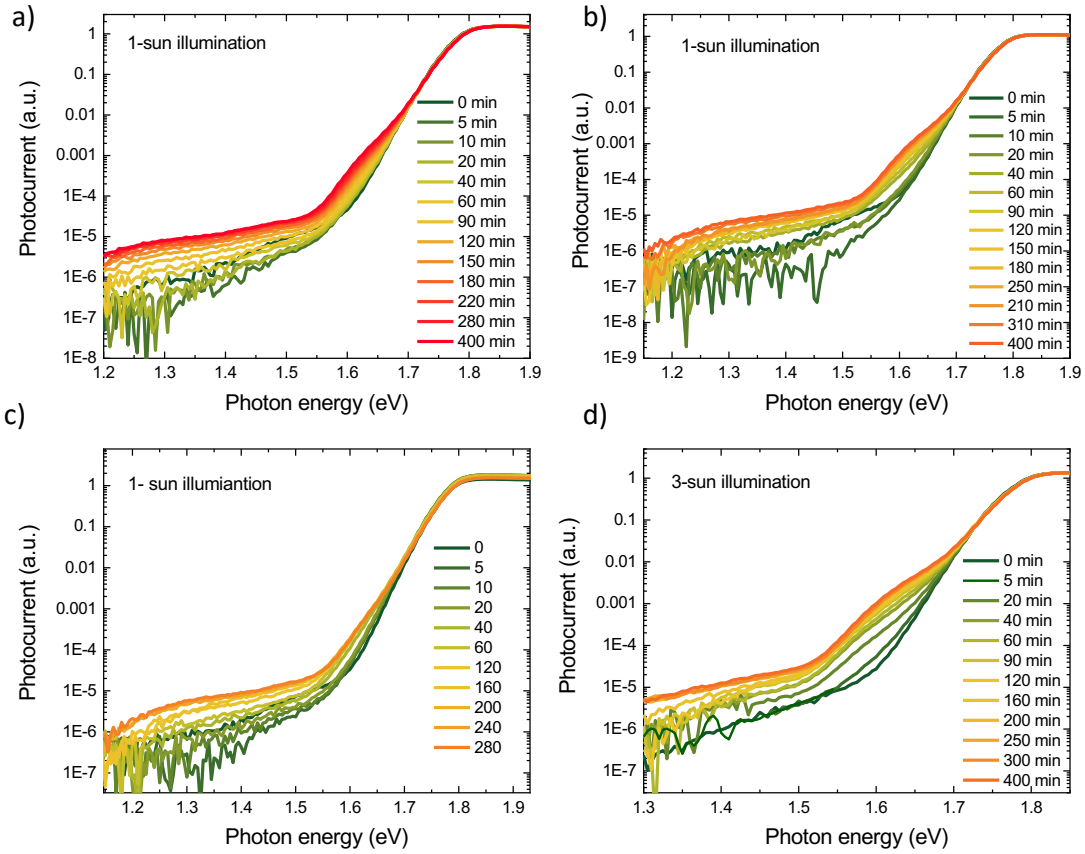

Fig. 44: a)-d) additional FTPS measurements on $FA_{0.83}Cs_{0.17}Pb(I_{0.6}Br_{0.4})_3$ solar cells where phase 2 is not formed even under a long-term illumination.

To better understand the relationship between deep defect level formation and phase segregation rate, we measure the evolution of the FTPS spectra during LS with a higher temporal resolution. In Fig. 45b, we can see a strong correlation between the concentration of light-induced deep defects, obtained by monitoring the sub-bandgap FTPS signal at 1.45 eV, and the magnitude of phase segregation, given by the FTPS signal at ~1.6 eV. The phase segregation rate is highest up to 40-60 min of LS, which coincides with a significant increase in the concentration of deep defects (Fig. 45a). After 40-60 min of LS, both the phase segregation rate (connected with the formation of the I-rich phase 1) and the deep defect formation saturate. Linear dependence of phase segregation on deep defect concentration with a correlation coefficient r = 0.97 indicates that photo-induced deep defects are the main migration channel in the transport of halide ions during phase segregation. Correlation, however, applies only to phase 1. When phase 2 begins to form at longer times of LS, the linear correlation ceases to apply, as can be seen in Fig. 46. This suggests that phase 2 results from a different mechanism than phase 1. To fully understand the dynamics of phase segregation as a two-step process and to answer why phase 2 is not formed in several samples we first need to find out the nature of the observed deep defects.

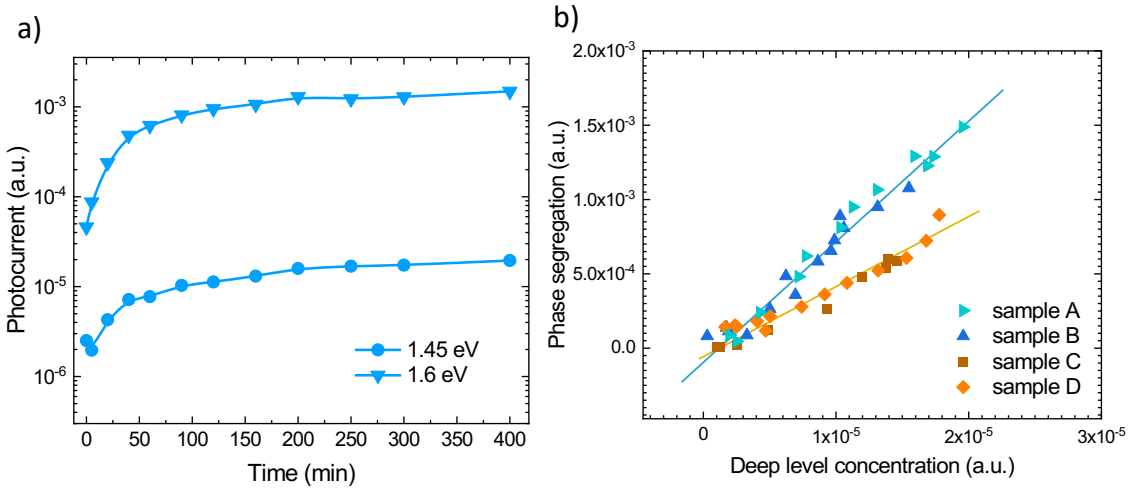

Fig. 45: a) Evolution of non-normalised FTPS photocurrent signals obtained at fixed photon energies 1.45 eV and 1.6 eV during LS; b) correlation of deep level concentration (given by the photocurrent at 1.45 eV) and phase segregation (given by the photocurrent at 1.6 eV).

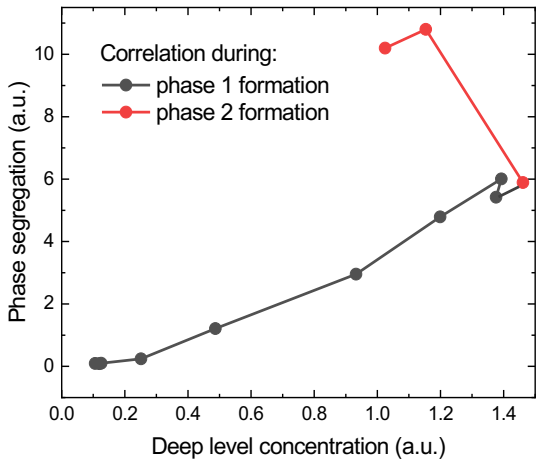

Fig. 46: Correlation of deep level concentration (given by the photocurrent at 1.45 eV) and phase segregation (given by the photocurrent at 1.58 eV). Measured on sample where phase 2 is formed under a long-term illumination.

6.3 XRD evolution upon LS

We have further measured the X-ray diffraction (XRD) powder pattern of the perovskite layer in a pristine state and irradiated for 5, 20, and 40 minutes to support the existence of phase segregation under LS. Thanks to the dependency of the lattice parameter on the halide content [151], [28] the phase separation into I-rich and Br-rich regions should be observable in the XRD pattern as the splitting or appearance of new diffraction peaks. Such light-induced peak splitting was previously reported in $MAPb(I, Br)_3$ by Hoke et al. [29] and Hu et al. [75].

The measured diffraction pattern of $FA_{0.83}Cs_{0.17}Pb(I_{0.6}Br_{0.4})_3$ thin film in Fig. 47 corresponds to the cubic perovskite phase of the claimed composition, in accordance with [146], [152]. As seen in Fig. 47b, with a longer light-soaking the peak (200) starts to be strongly asymmetric, being composed seemingly of two peaks. The original peak is slightly shifting towards higher diffraction angles and gets wider, while the new less intense peak is located at lower diffraction angles. Not so pronounced, but similar behaviour can be observed for peak (111) (Fig. 47c). When segregation occurs, the I-rich and Br-rich regions should have larger and smaller lattice parameters, respectively, compared with the well-mixed homogeneous phase [78].

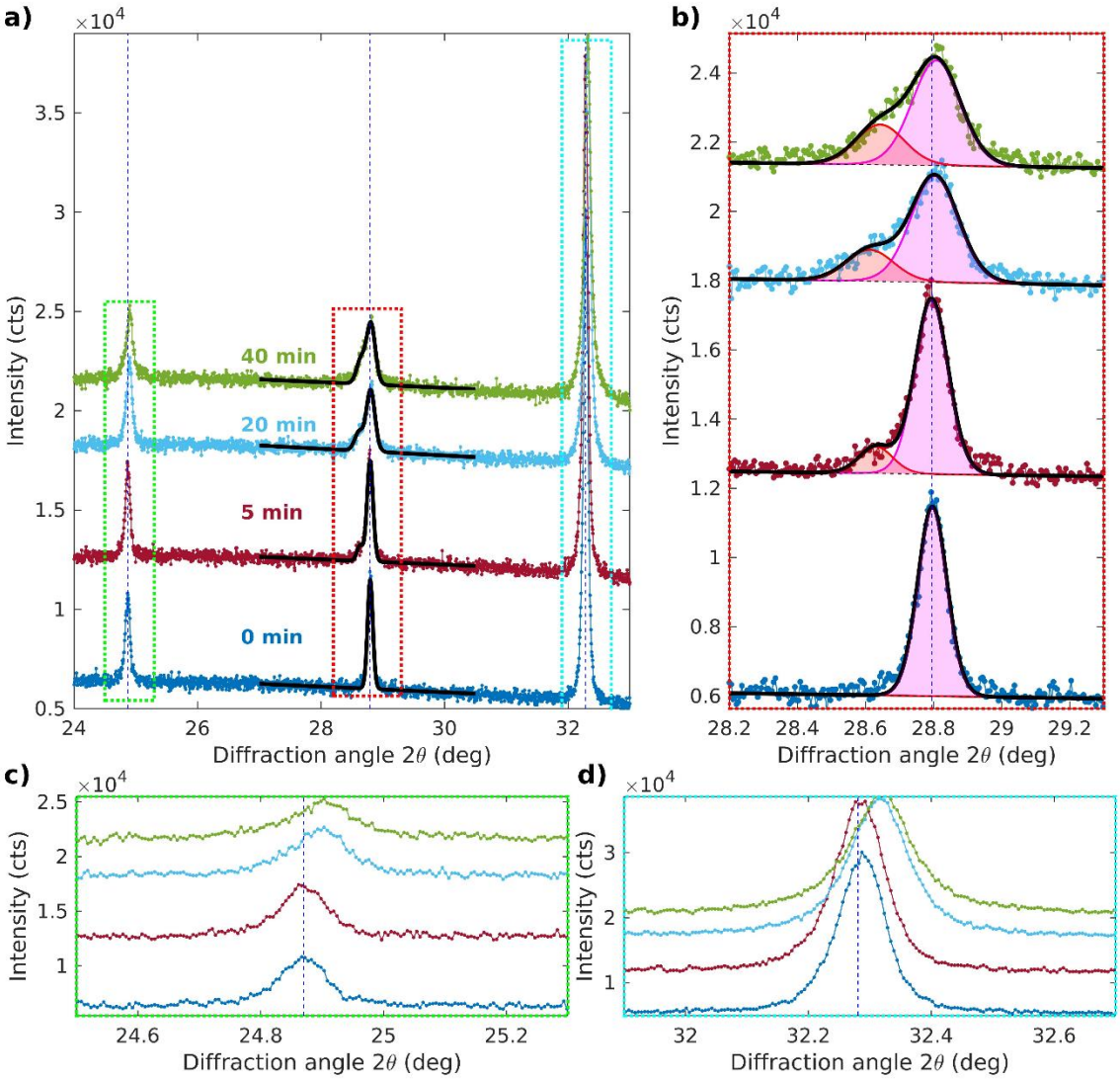

Fig. 47: XRD powder patterns showing the effect of a continuous AM1.5G illumination on a thin film $FA_{0.83}Cs_{0.17}Pb(I_{0.6}Br_{0.4})_3$. a) Cubic peaks (111), (200) and (201) at diffraction angles 24.87, 28.8, and 32.8 deg are shown, respectively. A detail of b) (200), c) (111) and d) (201) XRD peak.

The observed splitting to lower diffraction angles may be therefore associated with the formation of the I-rich phase while shifting to higher diffraction angles with the Br-rich phase. Comparing the cubic (200) reflections for $FA_{0.83}Cs_{0.17}Pb(I_{1-x}Br_x)_3$ perovskites with varying Br composition, the light-induced peak at ~ 28.6° corresponds best to the cubic (200) reflection of $FA_{0.83}Cs_{0.17}Pb(I_{0.75}Br_{0.25})_3$, which is close to the estimated composition $FA_{0.83}Cs_{0.17}Pb(I_{0.8}Br_{0.2})_3$ of phase 2 observed in PL and FTPS spectra (Fig. 37, Fig. 38, Fig. 42). Regarding the phase 1, observed in PL and

FTPS spectra, it is expected that its contribution to XRD pattern must be below the detection limit of XRD, thanks to the low concentration of segregated phase 1 (~ 0.1%).

Interestingly, peak (201), shown in Fig. 47d does not exhibit any visible splitting, only becomes wider and shifted to higher diffraction angles. If all of these phases were cubic and homogenous, we should observe the splitting of all the peaks in the diffraction pattern similar to Hoke's measurement [29]. On the contrary, we assume that firstly an I-rich non-homogenous layer is formed under LS in the close vicinity of grain boundaries of 220 nm large grains. This picture is consistent with the model of Br-rich/I-rich core-shell particles with a large amount of defects. Therefore we expect to observe broadening and asymmetry of the peaks rather than splitting. The diffraction pattern should be calculated using the Debye formula taking into account the strain field resulting from different compositions between core and shell. Since sample degradation in the ambient air forced us to collect data in a very limited time, the data are not sufficient for unambiguous line profile analysis. Nevertheless, qualitatively we observe the hkl-dependent splitting, broadening, and shift of the peaks as we expected for such a core-shell system. Based on these indications, we are quite convinced that phase segregation to I-rich and Br-rich regions occurs in our sample during light-soaking.

6.4 Origin of deep defects

A likely scenario is that under illumination of mixed-halide perovskites iodine atoms are mobilized as iodine is less bound in the lattice than bromine [153]. This results in the formation of new Frenkel pairs of iodine interstitials and iodine vacancies. The observed deep-level traps created during LS may be rather attributed to iodine interstitials which according to density functional theory (DFT) calculations [154] are the most common and stable deep defects in lead halide perovskites. Both the positive charge state I_i^+ and negative charge state I_i^- iodine interstitials are possible while neutral iodine interstitials are predicted to be thermodynamically unstable [154]. Iodine vacancies V_I do not introduce electronic states in the bandgap or create only shallow levels according to DFT investigations on similar material $FAPbI_3$, $CH_3NH_3PbI_3$ [155]–[157].

The origin of observed deep defects stemming from point defects other than iodine interstitials is unlikely. For instance, FA or Pb vacancies (V_{FA}, V_{Pb}) are reported to form more shallow traps in perovskites [155]–[157]. FA_I and I_{FA} antisites can create deep levels within the bandgap of FA-based perovskites. However, cation mixing substantially increases their defect formation energies and reduces the probability of their formation in perovskites with mixed cations (e.g. FACs or FAMA) [156]. Bromine interstitials have according to DFT more shallow nature in perovskites [158] and are less stable. Several spectra measurements on $APbBr_3$ perovskites [127], [159], [160], however, reveal deep sub-bandgap levels, which possibly originate from V_{Br}, Pb_i, and even Br_i. Light-induced formation of pairs of Br_i and V_{Br} appears to be less likely due to the weaker I-Pb bond than Br-Pb.

To prove that deep defect levels originate in iodine interstitials we measure the evolution of structure $FA_{0.83}Cs_{0.17}Pb(I_{0.6}Br_{0.4})_3$/ PbI_2 under continuous LED with a wavelength of 420 nm (see Fig. 48a). The structure is illuminated from the PbI_2 side. The selected illumination is above-bandgap for PbI_2 and therefore most of the light is predominantly absorbed in the PbI_2 layer, while only a negligible fraction of photons is absorbed in the upper perovskite layer. As can be seen in Fig. 48c, after 20 min of LS of the structure depicted in Fig. 48a, we observe an enhancement of sub-bandgap absorption in the upper perovskite layer which points to the increase in perovskite's deep defect concentration. As photons are considered to be absorbed predominantly in PbI_2 thin film, the increase of deep defect concentration in perovskite can be explained by the diffusion of light-induced iodine interstitials from the PbI_2 layer into the perovskite layer where they act as deep defect levels. A similar phenomenon was previously observed also on $MAPbI_3$ in Ref. [161].

Illumination of the similar structure $FA_{0.83}Cs_{0.17}Pb(I_{0.6}Br_{0.4})_3$/ glass/ PbI_2 from the side of PbI_2 (Fig. 48a) does not lead to any significant change in photocurrent spectra of perovskite layer as no diffusion of light-induced iodine interstitials from PbI_2 is possible in this configuration. A small change in FTPS spectra in configuration according to Fig. 48b is given by the photons that were directly absorbed in the perovskite layer. A comparison of the changes in both configurations shows that the effect of light absorption in the perovskite layer is negligible to the effect of I_i diffusion from PbI_2. The obtained experimental data in Fig. 48c reduces the possibilities of the

origin of observed deep levels in mixed-halide perovskite to iodine interstitials. The light-induced I_i diffusing from PbI_2 into mixed-halide perovskite induces also changes in the perovskite absorption edge as they form here I-rich phase domains.

Interestingly, the diffusing iodine from the PbI_2 layer to the perovskite layer leads beside the deep defect formation also to the formation of the I-rich phase. This can be seen in Fig. 49, where the FTPS spectra show an absorption edge shift toward low energies.

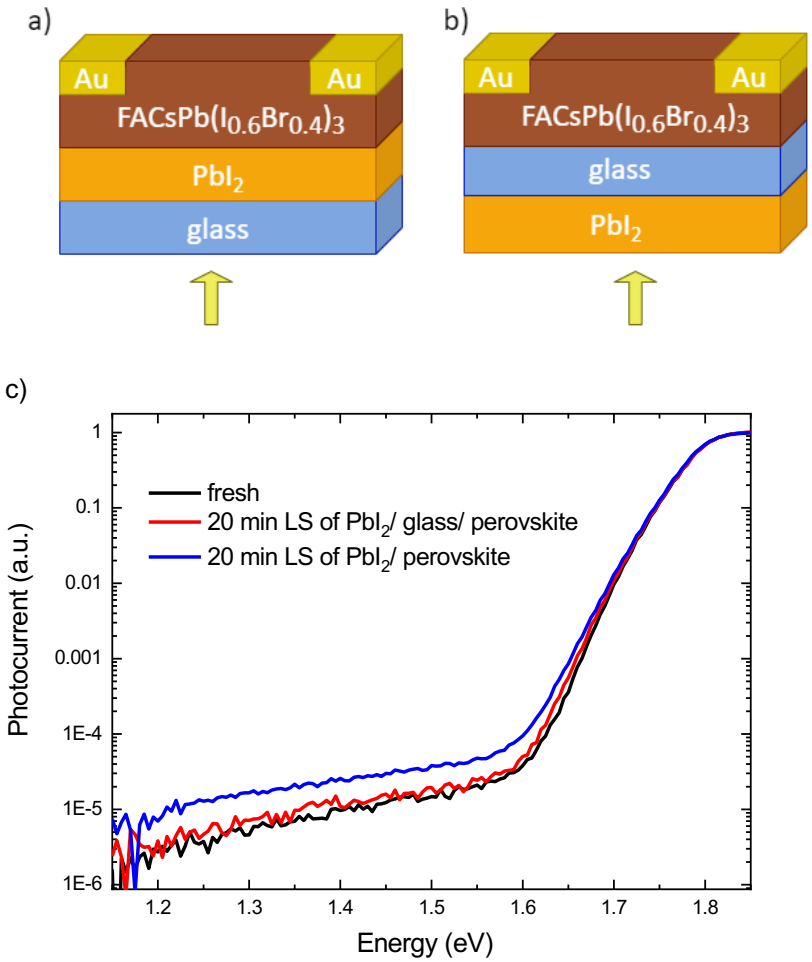

Fig. 48: Evolution of perovskite thin film after 20 min of LS from the PbI_2 side. Measured at architecture which a) allows and b) prevents the diffusion of light-induced iodines from PbI_2 into the perovskite layer. c) Comparison of light-induced changes for device architectures a) and b).

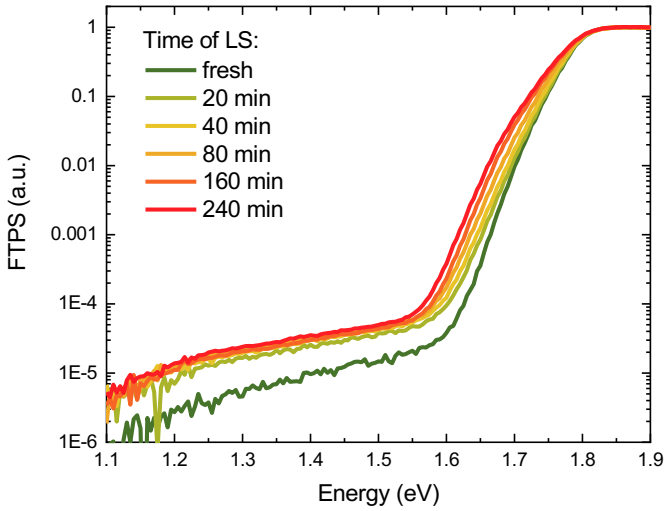

Fig. 49: $FA_{0.83}Cs_{0.17}Pb(I_{0.6}Br_{0.4})_3$ absorption edge shift and increase of sub-bandgap absorption due to exposure to iodine diffusing from mechanically attached PbI_2 layer. Measured at configuration according to Fig. 48a with blue LED illumination (420 nm).

We repeat a similar experiment using the $PbBr_2$ instead of PbI_2, as can be seen in Fig. 50. In this case, a UV lamp is used for LS to ensure that most of the light will be absorbed in the thin $PbBr_2$ layer. As can be seen in Fig. 50c, both structures, $FA_{0.83}Cs_{0.17}Pb(I_{0.6}Br_{0.4})_3$/ glass/ $PbBr_2$ and $FA_{0.83}Cs_{0.17}Pb(I_{0.6}Br_{0.4})_3$/ $PbBr_2$, do not show the formation of deep defects in the perovskite layer. This may be explained by a negligible diffusion of light-induced bromine interstitials Br_i from the $PbBr_2$ layer into the perovskite layer. The second possibility in the case of non-negligible Br_i diffusion is that Br_i do not form deep defects in FA, Cs-based mixed halide perovskites.

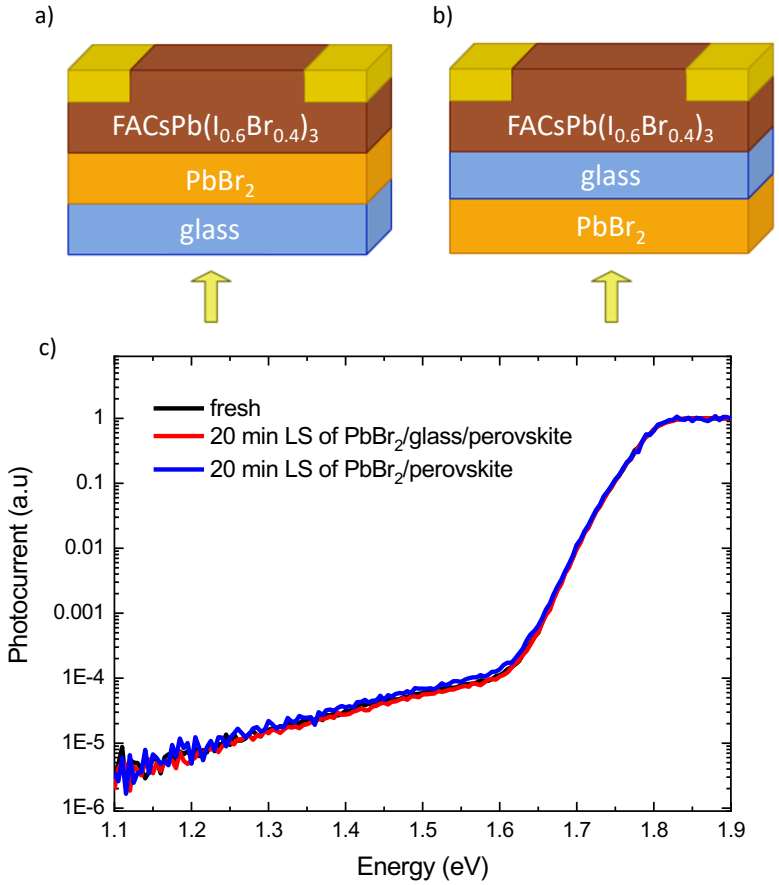

Fig. 50: Evolution of perovskite thin film after 20 min of LS. Measured at architecture which a) allows and b) prevents the diffusion of light-induced iodines from $PbBr_2$ into the perovskite layer. c) Comparison of light-induced changes for device architectures a) and b).

6.5 Phase segregation mechanism

In summary, considering the above-described experiment in Fig. 48, the weaker I-Pb bond than Br-Pb and deep-level nature as well as low formation energies of I_i, the observed deep defect levels can be linked to iodine interstitials. Linear dependence of phase segregation on deep defect concentration (Fig. 45) hence suggests that phase segregation may be attributed to iodine transport via iodine interstitial sites.

Frenkel pairs of I_i and V_I, formed upon LS, diffuse within the grain in random directions thanks to the concentration gradient. The light-induced I_i are most likely re-integrated into the lattice at grain boundaries/surfaces, which are characterised

by an excess of unsaturated bonds/vacancies and act as sinks for charged defects [162]. The I_i and V_I diffusion coefficient of ~2×10^{-9} cm^2s^{-1} [163], [164] and average grain size of ~ 200 nm enables their fast diffusion toward the grain surface within ~ 50 ms. Excess iodide may at the grain boundaries form a non-homogenous layer. Such a non-homogenous I-rich layer, shown by the grey area in Fig. 51b, is represented by the initial decrease in the slope of the absorption edge (Fig. 38a) in FTPS spectra and may also explain the observed broadening and asymmetry of the peak (201) with no distinguishable splitting in XRD pattern (Fig. 47d).

Further accumulation of iodide on surfaces and at grain boundaries leads to the formation of the segregated I-rich phase 1 with x=0.9, which manifests itself in the formation of a clearly distinguished inflection point at 1.58 eV (Fig. 38a).

Electron trapping at the positively charged I_i^+ or hole trapping at the negatively charged I_i^- and subsequent reaction of two filled traps I_i^0 can also lead to the formation of an I_2 molecules at the grain boundaries/surfaces [165]. Iodine imbalance between surface and bulk can trigger a series of compensating reactions and as a consequence, PbI_2 may segregate as a separate phase [165]. PbI_2 formation is supported by the previous formation of an I_2 molecule [165]. Such I_2/PbI_2 formation may explain a distinct feature at 2.5 eV, which appears during LS in the above-bandgap part of the FTPS spectra at OC and MPP condition (see Fig. 38c and Fig. 39c). The assignment of the feature at 2.5 eV to the I_2/PbI_2 is in good accordance with spectra measurements in [166] and may moreover explain spectra measurements on mixed-halide perovskites with varying I and Br concentration from x= 0 to x= 1 in [29]. Here an increasing iodine concentration leads to a more pronounced hump at 2.5 eV and is completely missing in the case of pure $MAPbBr_3$ perovskites. The above-proposed formation mechanism of I_2/PbI_2, which is dependent on free carrier concentration, explains also why the feature at 2.5 eV is not visible in the case of samples light-soaked at short-circuit. The phenomenon is observed only at open-circuit and MPP conditions when the higher concentration of light-induced iodine interstitials and photo-generated carriers encourages I_2 and subsequent PbI_2 formation.

Our proposed mechanism of phase segregation based on iodine migration through interstitial sites, described below, agrees with the first-principle calculations

in [167], according to which interstitial and vacancy hopping barriers in $MAPbI_3$ perovskites are similar, and hence both mechanisms are probable. However, the proposed interstitial ion migration is not in accordance with the prevailing notion in the scientific community according to which phase segregation proceeds solely through vacancy-mediated migration [78], [47], [79]. This conclusion was derived from experiments on materials with intentionally created intrinsic defects, e.g. with non-stoichiometric precursors. Therefore, only one type of defect, either halide vacancies or interstitials, prevailed in the studied perovskites. Phase segregation observed in the case of excess intrinsic halide vacancies has been so far explained by an increased number of available pathways for anion hopping via vacancies. Negligible phase segregation in materials with excess halide has been also presented as evidence of an exclusively vacancy-mediated anion migration. Previous works have however neglected that the efficacy of phase segregation depends not only on anion migration efficiency but also on the efficiency of halide incorporation into the lattice. Intentionally created excess halide vacancies, primarily located at grain boundaries or surfaces [168], support the incorporation of migrating halides into the lattice. Excess halides on the contrary passivate unsaturated bonds at the grain boundaries [169], decreasing the number of sites where the LS-induced halide interstitials can be created or where migrating iodines can be incorporated. Therefore, the importance of interstitial-mediated anion migration cannot be excluded based on observations in [47], [78], [79]. Light-induced iodine interstitials being the main migrating species can also explain the discrepancy between Monte Carlo simulations in [78], which was based on the assumption of the vacancy mechanism, and experimental results obtained by spatially resolved PL measurements [44], [77], [170], [80], [171], [172]. Experimental results showed that I-rich domains are preferentially located along grain boundaries leaving the Br-rich phase in the grain interior, while the Monte Carlo simulation in [78] predicted exactly the opposite arrangement with the Br-rich phase accumulating along boundaries. This discrepancy between theory and experiment probably arises from the incorrect assumption, that vacancies are the main migrating species.

It is worth noting, that thanks to the charge of created defects, there must be a difference between the mechanism of phase segregation at OC and SC regimes. In

the case of OC, charged iodine interstitials diffuse in a random direction, until they are built in the lattice, creating an I-rich phase, or until they annihilate with light-induced iodine vacancies [173]. Under SC and MPP, charged iodine interstitials and vacancies are affected by an internal electric field and drift in one opposite direction. SC/MPP should therefore lead to a different spatial arrangement of phase segregation than in samples that were light-soaked at OC or as thin films. In the case of SC, the I-rich phase should be predominantly located at grain boundaries which are closer to the electron or hole transport layer depending on the sign of formed iodine interstitial, while the Br-rich phase should be located oppositely. Now it is not possible to clearly decide whether pairs I_i^+/V_I^- or I_i^-/V_I^+ are formed and therefore assign at which contact iodine accumulates and at which bromine. As various operational conditions should lead to a different spatial arrangement of phase segregation, we highlight the importance of measurements at MPP, to compare phase segregation in real devices, since solar cells operate near their maximum power point.

6.5.1 Phase 1 formation

Besides I_i diffusion to grain boundaries/surfaces, V_I also diffuses through the grain and with each jump moves lattice bromine or iodine to the opposite direction of its movement. The ratio of the diffusion current of lattice iodine J_I and diffusion current of lattice bromine J_{Br} is given by the ratio of iodine and bromine stoichiometry in mixed-halide perovskite $APb(I_xBr_{1-x})_3$:

$$\frac{J_I}{J_{Br}} = \frac{x}{1-x} \tag{6.1}$$

$$J_{vac} = -J_I - J_{Br} = -\frac{J_I}{x} = J_{int}. \tag{6.2}$$

Here $x \in (0, 1)$ corresponds to the halide local stoichiometry coefficient and J_{vac} represents the diffusion current of V_I, which is equal to the diffusion current of iodine interstitials J_{int} thanks to the same generation rate of I_i/V_I and very similar diffusion constants [167]. Since $x < 1$, the eq.(6.2) shows that the flux J_{int} of I_i facing to the surface is greater than the opposite flux of lattice iodine J_I to the grain interior (Fig.

51a). This enables the formation of phase 1, which is governed by the total flux of lattice and interstitial iodine J_{tot}:

$$J_{tot} = J_{int} + J_I = J_{int}(1 - x). \tag{6.3}$$

Consequently, an I-rich phase accumulates along the perovskite grain boundaries and surfaces, while an iodine-depleted region remains within the grain interior. This is in good accordance with [77], [143], [170], [144], [47], [80], [171], [172], [174]–[176]. There, various microscopy techniques, including PL mapping [80], [171]; cathodoluminescence imaging [143], [170], [172]; transmission electron microscopy TEM [174]; energy-dispersive X-ray spectroscopy EDS [175] and atomic force microscopy AFM [176] show that I-rich domains are preferentially located in the close vicinity of grain boundaries/ surfaces and maternal/Br-rich domains in grain interiors. Reaching sites near grain boundaries by mobile iodides is moreover supported by accelerated I_i diffusion along the grain boundaries [172].

Using the molecular weight MW of 1 mol of $FA_{0.83}Cs_{0.17}Pb(I_{0.6}Br_{0.4})_3$ (591 $g.mol^{-1}$) obtained from particular atomic masses, the Avogadro constant A (6.022 $\cdot 10^{22}$ mol^{-1}), the mass density ρ_m of lead halide perovskite $CH_3NH_3PbI_3$ (3950 $kg.m^{-3}$)

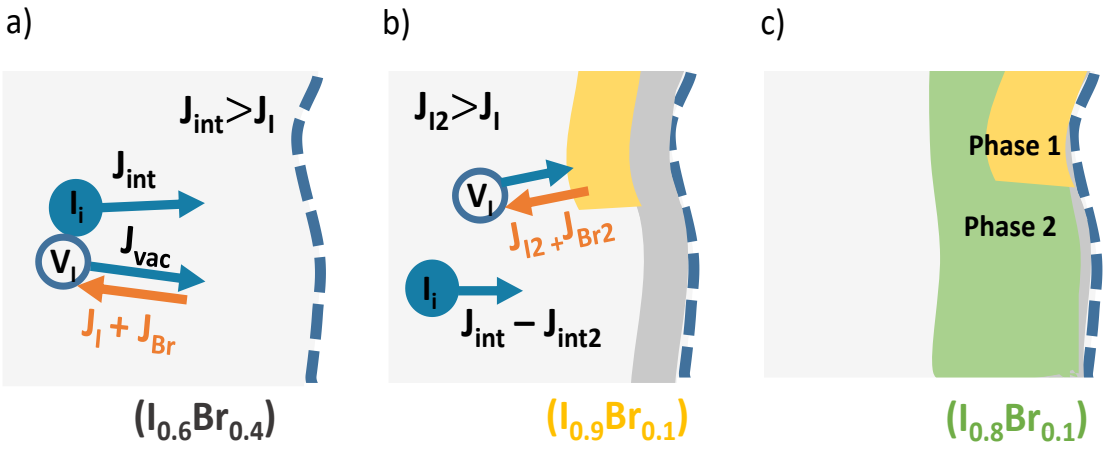

Fig. 51: Mechanism of phase segregation: a) light-induced formation of I_i/V_I pairs and the principle of I_i accumulation at grain boundaries; b) formation of an I-rich non-homogenous layer (marked with grey area), the perovskite phase 1 (marked with a yellow area) and a subsequent dissolution of iodine from phase 1/inhomogeneous layer slightly deeper into the perovskite grain interior; c) formation of phase 2 (marked with green area).

and average grain size obtained from SEM measurement (2R=220 nm), one can estimate the number of molecules N in one grain as:

$$N = \frac{4}{3}\pi R^3 \rho_m \frac{A}{MW}. \quad (6.4)$$

The number of iodine atoms in one grain can be then obtained by multiplying the number of molecules N by an iodine stoichiometry factor of 0.6x3. Considering that phase 1 makes up according to the FTPS measurement 0.1 % of perovskite at 160 min of LS, we estimate that from one grain, an estimated 40 000 iodine atoms are involved in the formation of phase 1 at 160 min of LS. Based on this estimation, phase 1 does not evenly cover the entire grain surface and forms rather discontinuous islands at the interfaces of several grains where an enhanced disorder and amplified stress seed an optimal place for the new phase nucleation (see yellow area in Fig. 51b). This is in line with spatially resolved measurement in Ref. [143], which was performed on mixed halide perovskites with an identical composition to ours. There, combining scanning electron microscopy (SEM) and high-resolution cathodoluminescence (CL) mapping showed that segregated I-rich phases are preferentially located near grain boundaries and form rather isolated clusters, rather than continuous layers along the grain boundary. Since the observed I-rich phase in Ref. [143] may be attributed to phase 1, thanks to the identical PL redshift to 1.6 eV under LS, Ref. [143] confirms the proposed spatial arrangement of phase 1 in Fig. 51b.

In addition to the iodine concentrating in phase 1, iodine-rich regions at the grain boundaries, which do not form a spatially resolved phase, should be anticipated, too (see grey area in Fig. 51b).

6.5.2 Phase 2 formation

At longer times of LS, several samples show the formation of the I-rich phase 2 with x=0.8, which is manifested in PL and FTPS spectra by a shoulder at 1.68 eV (Fig. 37, Fig. 38 and Fig. 42). Phase 2 must be formed by a different mechanism since the linear correlation between segregation and deep defect concentration ceases to apply (Fig. 46).

A combination of several underlying mechanisms may be involved in the formation of phase 2. Firstly, the accumulation of I_i at the grain boundaries leads to

the second iodine concentration gradient J_{int2}, which is oriented to the grain interior (Fig. 51b). Such gradient prevents diffusion of other iodine interstitials from the grain interior to the boundaries. Moreover, as the local stoichiometry coefficient x has a higher value on the surface due to the presence of phase 1, the flux of lattice iodine J_I to the grain interior (caused by V_I diffusion) increases (see equations (6.2), (6.3) and Fig. 51b). Furthermore, the formation of phase 1 with different lattice constant [151] may lead to the mechanical strain between phase 1 and maternal phase [170]. All these processes allow iodine from the I-rich phase 1 at the grain boundaries or inhomogeneous layer to re-distribute slightly more into the grain interior, leading to the formation of a new phase 2 in close vicinity of the grain boundary/surface. Weakly bound iodine at grain boundaries/surfaces from the inhomogeneous layer or iodine obtained after disintegration of an I_2 molecule at grain surfaces must be also involved in the formation of phase 2 as the amount of phase 2 is 100x higher than the amount of phase 1. Phase 2 may, thanks to the $\sim$ 4 million iodine atoms contributing from one grain, form a continuous layer along the grain boundary/ surface (Fig. 51c). This is consistent with spatially-resolved measurements on MA-based and Cs-based mixed halide perovskites [170], [80], [171], [172].

6.5.3 Relaxation mechanism

As seen in Fig. 38b, Fig. 39b, and Fig. 40b, by storing the samples in the dark, the concentration of deep-level traps generally gradually decreases. This decrease in defect concentration during relaxation in the dark was also recorded on $MAPbI_3$ solar cells in Ref. [177] and may be explained by the annihilation of iodine interstitials with iodine vacancies [173]. The slower rate of recovery compared to the phase segregation rate when exposed to light may be due to the slower ionic conductivity in the dark [178]. In the dark, I_i diffusing from grain boundaries back to the volume must be first thermally created, which is a slower process than light-induced I_i formation causing phase segregation. It is worth noting that some samples that were previously LS in OC conditions show an increase in defect concentration within the first 5 min of relaxation (see Fig. 38b).

6.5.4 Drop (increase) in the deep defect concentration at longer times of LS (after switching off LS)

The observed drop in the concentration of deep-level defect at longer times of LS (Fig. 38a-160 min) may be explained by the formation of I_2/PbI_2 from iodine interstitials. This explanation is consistent with the fact that the decrease in deep defect concentration occurs only in those samples where after a long period of LS a considerable feature at 2.5 eV emerges. The initial increase in defect concentration in the case of OC within the first 5 min of relaxation is probably also related to I_2 molecules. After switching off the illumination, there is an excess concentration of light-generated vacancies which may react with an I_2 molecule and lead to its decay. During the decay of an I_2 molecule, one iodine occupies the vacancy and the second iodine remains in the sample as an interstitial. Therefore, we observe such a sudden increase in iodine interstitial concentration during the first minutes of relaxation in the dark. Such mechanism of initial increase in defect concentration during relaxation due to decay of an I_2 molecule correlates well with the observation that a steep increase is pronounced more, the larger the hump at 2.5 eV is and that it is completely missing at SC when the hump at 2.5 eV is not observed.

Another possible explanation of the drop in the deep defect concentration at longer times of LS is that phase 2 may cause the formation of a barrier that is less permeable to vacancies. As a consequence, V_I accumulate in the grain interior and recombine more with the new light-induced iodide interstitials. Such an explanation is consistent with the observation that a drop in deep defect concentration at longer times of LS is observed only when phase 2 occurs and may explain also the sudden increase in the deep defect concentration after switching off the illumination. As the new Frenkel pairs are no longer formed without a source, the previously formed V_I quickly recombine with I_i diffusing from the surface. Other interstitials then have nothing to recombine with, which leads to an increase in their concentration. Since phase 2 makes up 10% of the material, the formation of a diffusion barrier is well justified.

6.6 Variation in terminal phase

We found two typical patterns of phase segregation in our $FA_{0.83}Cs_{0.17}Pb(I_{0.6}Br_{0.4})_3$ samples. About half of the studied samples show first formation of the lower bandgap phase ($I_{0.9}Br_{0.1}$) which is subsequently followed by phase 2 with 80% iodine (Fig. 38, Fig. 42). The other half of the studied samples, however, do not show any formation of I-rich phase 2 even at longer times of LS. The deep level concentration only saturates simultaneously with I-rich phase 1 in such samples (Fig. 43, Fig. 44). This saturation is most probably caused by the dynamic equilibrium between the flow of light-induced I_i, diffusing from grain interior towards the boundary, and the flow of thermally released I_i, diffusing from the grain boundaries/ surfaces to the volume. The idea of dynamic equilibrium is also supported by the reversibility of the spectra evolution in the dark when only the flow of thermally released I_i, diffusing from the grain boundaries to the volume is present.

By comparing the FTPS evolution typical for both categories of samples with a terminal phase 1 and terminal phase 2, we see that the key difference lies in the FTPS evolution during the initial stages of LS (see Fig. 38, Fig. 43, Fig. 52). In samples with terminal phase 1, the general growth of the deep defect concentration is first preceded by its decrease within the first 5 – 20 min of illumination. The decrease in deep defect concentration is accompanied by the improvement in the overall photocurrent signal, which is present in both types of samples, but the phenomenon is strongest in samples with terminal phase 1 (Fig. 52). Overall photocurrent improves in samples with terminal phase 1 on average by the 25 % and in the samples with terminal phase 2 only by the 5 % after 5 min of LS. Such initial signal enhancement may be explained in a way that light-induced iodine interstitials passivate defects at grain boundaries, which act as more efficient non-radiative recombination centres. Once the concentration of iodines exceeds some threshold value needed for surface/grain boundaries passivation, they itself start to form deep iodine interstitial defects [169]. Such an explanation may be used also for observation in PL data in Fig. 37, where PL intensity increases in the maternal phase during LS thanks to the passivation of defects at grain boundaries and the resultant reduction in non-radiative recombination. The passivation of a strong recombination centre by light-

induced defects was proposed also in 5.3, and 5.4 for MAPB single crystal. There, the passivation explains a disappearance of the rapid current drop in CWFs (Fig. 33) and improvement in hole carrier lifetime under above-bandgap illumination (Fig. 27).

Another major difference between both categories of samples lies in the evolution of the above-bandgap part of the FTPS spectra (see Fig. 53). In samples with two segregated phases, the illumination leads to the formation of a distinctive shoulder around 2.5 eV. This shoulder is, however, significantly suppressed in the case of samples with terminal phase 1. Based on spectra measurements in [166], [179] the shoulder at 2.5 eV may be attributed to the formation of an I_2 or PbI_2. The connection of the shoulder at 2.5 eV with iodine is also supported by the spectra measurements on mixed-halide perovskites with varying I and Br concentration in Ref. [29], where increasing iodine concentration leads to a more pronounced hump at 2.5 eV and is completely missing in case of pure $MAPbBr_3$ perovskites.

Both categories of samples were prepared by the same process. However, as the preparation is manual, deviations in the quality and morphology of perovskite films, that have a significant effect on the result of phase segregation, are possible.

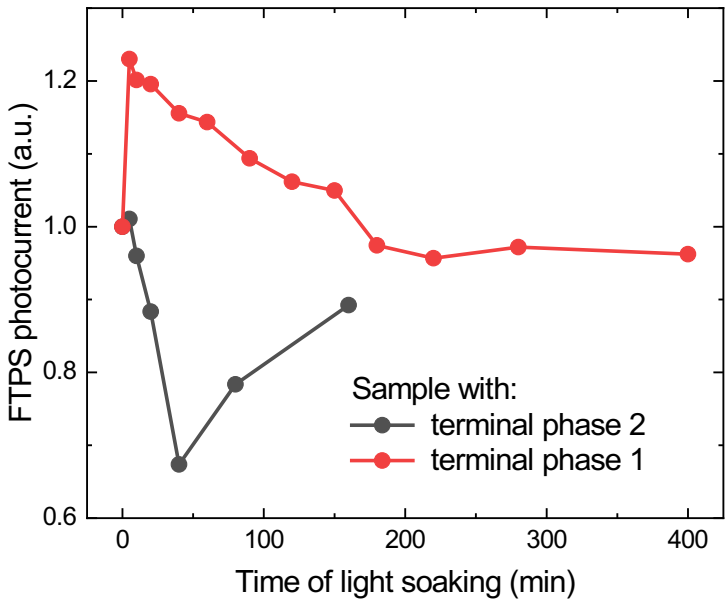

Fig. 52: Comparison of typical evolution of photocurrent signal, obtained at fixed photon energy 1.85 eV from non-normalised FTPS spectra, for samples with terminal phase 1 and 2.

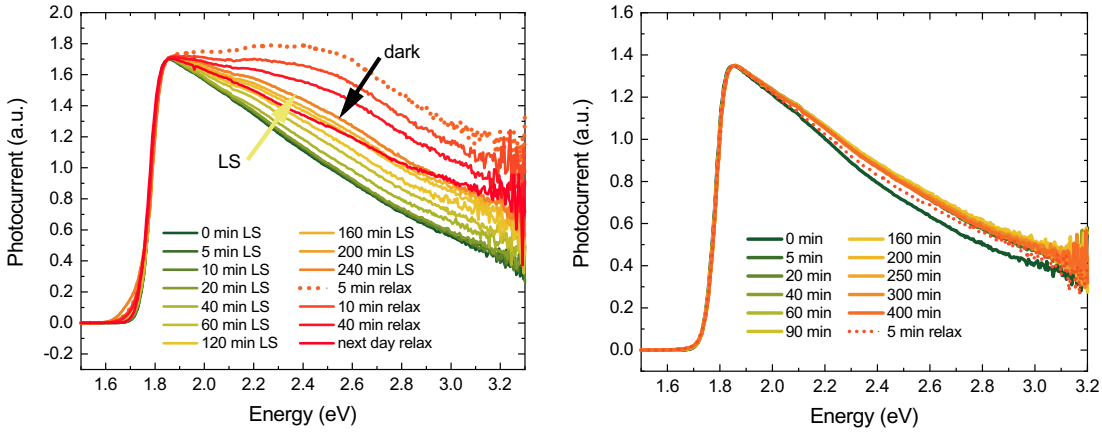

Fig. 53: Typical evolution of above-bandgap FTPS spectra under continuous AM1.5G illumination at open-circuit. Measured on samples a) with terminal phase 2 and b) with terminal phase 1.

The difference between the two categories of samples may lie in the variation of their grain size. Samples with terminal phase 1 probably have smaller grains and thus more defects associated with grain boundaries. This can explain why the photocurrent enhancement at the early stages of LS is most pronounced in the samples with terminal phase 1 as here passivation effect shows most due to the large amount of defects associated with grain boundaries. Conversely, samples with larger grains are characterized by the lower density of defects at grain boundaries, which act as efficient non-radiative recombination centres. In the case of samples with larger grains, a lower amount of iodine interstitials is necessary for the passivation of surface defects. This explains why samples with terminal phase 2, characterized by larger grains, typically do not show an initial decline in deep defect concentration after the first 5 min of LS as was observed in samples with terminal phase 1. The number of I_i probably already exceeded the threshold value necessary for passivation of grain boundary defects before the first 5 min of LS. Excess light-induced I_i, however, also form deep defects, which act as less efficient recombination centres compared to defects at grain boundaries, as it is proposed in [169], [180].

Variation in grain size may also explain the formation or absence of phase 2. Photo-generated I_i may be more evenly distributed at grain boundaries in samples with smaller grain sizes, as here the larger area of grain boundaries is available. Weak overall accumulation of iodine interstitials at surfaces/grain boundaries in samples with low crystallinity may not create a sufficient concentration gradient to prevent

diffusion of other iodines to grain boundaries. Insufficient concentration gradient also does not lead to the predominance of vacancy transport toward grain boundaries, which is a key process responsible for the creation of phase 2. The high relative surface area in small grain-sized perovskites further enhances the contribution of thermally-induced I_i from the surface. As a consequence, a dynamic equilibrium occurs for small grains more easily. Phase segregation is terminated by phase 1 when dynamic equilibrium is reached under illumination. The dynamic equilibrium prevents the formation of the excess of I_i at grain boundaries which is necessary to support vacancy transport via concentration gradient. For even smaller grain sizes, it can be expected that phase segregation will not occur at all. A complete suppression of phase segregation will occur when the number of deep defects associated with grain boundaries reaches such an amount that the flow of light-induced I_i, passivating boundary defects, will equal the flow of thermally-induced I_i from these defects. Therefore, a suitable way how to suppress or fully reverse phase segregation should be to intentionally grow perovskites with lower grain size. This prediction is in line with current research [181], [48] in which the threshold grain size of around 44 nm was found for $CsPb(Br_xI_{1-x})_3$ perovskites. Here, phase segregation was found to take place only for an average crystal size equal to or larger than this threshold size. Similarly, work in Ref. [45] did not record phase segregation in mixed-halide nanocrystals with an average 12 nm grain size. On the other hand, as grain boundaries/surfaces are the places, where phase segregation primarily occurs, the presence of surfaces/ grain boundaries is inevitable for the process of phase segregation.

Samples with larger grains have lower relative surface area and thus light-induced I_i can easily saturate the grain boundaries/surfaces. Overall accumulation of I_i is hence more easily achievable in samples with improved crystallinity. This increases the probability that phase 2 will be formed before thermodynamic equilibrium occurs and stops the further evolution of phase segregation. Thanks to the greater trajectory that I_i has to overcome in a large grain before reaching the grain boundary, the larger grain sizes may also increase the probability of I_i annihilation with V_I in grain interior. Annihilation will be most pronounced at longer times of LS when there is a statistically highest concentration of V_I in grain interior.

Larger grain size in samples with terminal phase 2 can therefore also explain the observed drop in deep defect concentration at longer times of LS. The suggested variation in crystallinity of samples with terminal phase 1 or 2 is also in line with the observed differences in the above-bandgap absorption. More significant accumulation of I_i at grain boundaries in samples with terminal phase 2, characterized by larger grain size, increases the probability of an I_2 or PbI_2 formation. The larger the grains, the more pronounced the shoulder at 2.5 eV can be therefore expected.

To prove that variation in grain sizes is the main difference between samples with terminal phase 1 or 2, we measure the cross-section SEM images of studied samples. As can be seen in Fig. 54, the sample with terminal phase 1 possesses lower grain sizes in the perovskite layer than the sample showing the formation of both phases 1 and 2. The average grain size of perovskite with terminal phase 2, obtained from several scans, is 220 nm, while the grains in samples with terminal phase 1 are typically 30% smaller, with an average grain size of 160 nm.

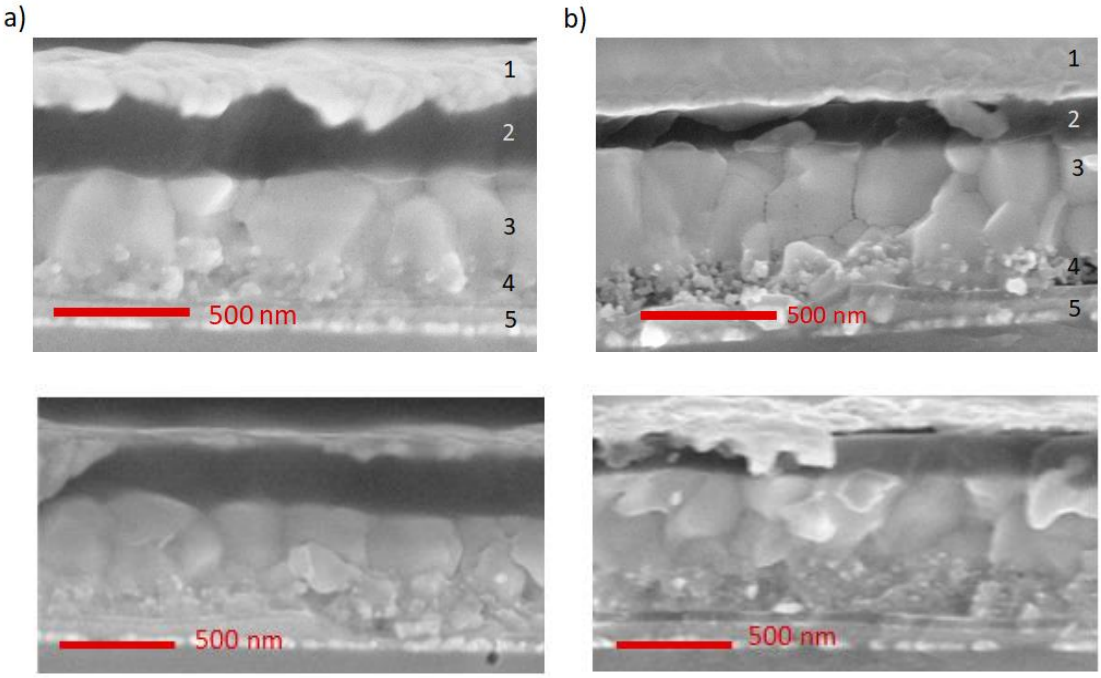

Fig. 54: Cross-section SEM images of mixed-halide perovskite solar cells. a), c) measured on SC with terminal phase 2 and b), d) on SC with terminal phase 1. The layers 1, 2, 3, 4 and 5 stands for Au, Spiro-OMeTAD, $FA_{0.83}Cs_{0.17}Pb(I_{0.6}Br_{0.4})_3$, mesoporous TiO_2 and compact TiO_2 layers, respectively.

6.7 Diffusion equation in a sphere

To outline the dependence of phase segregation velocity on the grain size, we solve the diffusion equation for the transport of light-induced I_i in a spherical grain of radius R:

$$\frac{\partial C_i}{\partial t} = G - \mathrm{div}\overrightarrow{J_{int}}. \tag{6.5}$$

Here, C_i represents the deep defect concentration of I_i created at a constant generation rate G per unit volume per second, and J_{int} stands for the diffusion current of I_i to the grain surface, which is related to the I_i diffusion constant D_i:

$$\overrightarrow{J_{int}} = -D_i \nabla C_i. \tag{6.6}$$

The diffusion coefficient D_i of $\sim 2\times10^{-9}$ cm^2s^{-1} [163],[164] and average grain size of ~ 220 nm enable fast diffusion of I_i toward the grain surface within ~ 50 ms. Considering that the transport of defects is mediated purely by the diffusion and taking into account that photo-excited defects recombine at the grain boundary in the time range of ~ 50 ms, which is much less than the characteristic time used at the measurement (tens of minutes), we may neglect the time derivative at the diffusion equation (6.5) and express the diffusion in the quasi-steady-state approximation:

$$0 = \frac{\partial C_i}{\partial t} = G + D_i \Delta C_i \tag{6.7}$$

The same equation (6.7) applies to the diffusion of iodine vacancies. After rewriting eq. (6.7) in spherical coordinates:

$$\frac{1}{r^2}\frac{\partial}{\partial r}\left(r^2 \frac{\partial C_i}{\partial r}\right) + \frac{1}{r^2 \sin\theta}\frac{\partial}{\partial \theta}\left(\sin\theta \frac{\partial C_i}{\partial \theta}\right) + \frac{1}{r^2 \sin^2\theta}\frac{\partial^2 C_i}{\partial \varphi^2} = -\frac{G}{D_i} \tag{6.8}$$

and considering no angular dependence of the concentration $C_i(r)$ on the spherical coordinate angles θ and φ, the continuity eq. (6.7) takes the form:

$$\frac{d}{dr}\left(r^2 \frac{dC_i}{dr}\right) = -\frac{G}{D_i} r^2. \tag{6.9}$$

By integrating the eq. (6.9) we get:

$$r^2 \frac{dC_i}{dr} = -\frac{G}{D_i}\frac{r^3}{3} + c_1, \tag{6.10}$$

where the integration constant c_1 is related to the flow from the centre of the sphere as concentration gradient of iodine interstitials multiplied by the diffusion coefficient represents according to the Fick´s Law the diffusion current of iodine interstitials J_{int}. Since there is no additional source of charged deep defects in the centre of the sphere, the integration constant c_1 must be zero and equation can be simplified to the form:

$$J_{int}(r) = -D_i \frac{dC_i}{dr} = \frac{Gr}{3}. \tag{6.11}$$

The integration of eq. (6.11) leads to the form:

$$C_i(r) = -\frac{Gr^2}{6D_i} + c_2, \tag{6.12}$$

where the value of integration constant c_2 is given by the boundary condition, which considers that the concentration $C_i(R)$ has a defined value on the surface: $C_i(R)$ = constant. By setting the value of c_2 so that the dependence of concentration on the coordinate r in eq. (6.12) disappears, we get

$$C_i(r) = C_i(R) + G\frac{R^2 - r^2}{6D_i}. \tag{6.13}$$

As further follows from the eq. (6.11), the diffusion current of I_i at the grain surface J_{int} depends directly on the grain size R:

$$J_{int}(R) = \frac{GR}{3}. \tag{6.14}$$

The larger the grain, the higher the flux J_{int} flows to the boundary, which increases the iodine accumulation at grain boundaries and hence the likelihood of phase 2 formation.

The simplified model derived above does not describe the formation of phase 2 as it does not consider the contribution of diffusion of iodine vacancies. For a detailed description of phases 1 and 2, a more detailed theoretical analysis is necessary.

6.8 Grain size effect on perovskite response to light-soaking

To verify the influence of grain size on the sample response to prolonged illumination, we prepare MAPI thin films *A, B,* and *C* with intentionally varied crystallinity. The MAPI material has been chosen over mixed-halide perovskite thanks to the much easier grain size control during the growth process. We perform similar measurements on the structure MAPI/PbI_2 as in section 6.4 (see Fig. 48a, c). We illuminate the structure from the PbI_2 side by the continuous LED of 420 nm wavelength. The selected illumination is above-bandgap for PbI_2 and therefore most of the light is predominantly absorbed in the PbI_2 layer. As shown in Fig. 55, we generally observe an enhancement of sub-bandgap absorption in the upper perovskite layer. This points to the increase in perovskite's deep defect concentration which appears thanks to the diffusion of light-induced iodine interstitials from the PbI_2 layer into the perovskite layer.

Interestingly, sample *A* with the lowest crystallinity shows the smallest spectra changes upon LS of PbI_2 (Fig. 55). On the contrary, the sub-bandgap absorption increases most significantly in sample *C* with the largest crystallinity. Such behavioural differences are in accordance with the previous explanation in section 6.6. The light-induced I_i first passivate defects at grain boundaries, which act as more efficient non-radiative recombination centres. Once the concentration of iodines exceeds some threshold value needed for surface/grain boundaries passivation, they itself start to form deep iodine interstitial defects [169]. Larger grain-sized samples have a lower density of defects associated with grain boundaries and hence a lower amount of I_i is necessary for the passivation of surface defects. The number of I_i diffusing to samples *B* and *C* quickly exceeds the threshold value for surface defect passivation and starts to form deep defects even before the first 10 minutes of LS. The lower grain-sized sample *A* needs a much higher amount of I_i to fully passivate grain/surface defects. The passivation of surface defects by diffusing iodine is manifested in sample *A* by a slight decrease of the sub-bandgap part within the first 10 min of LS. Thanks to strong passivation, a much smaller amount of diffusing iodine can itself form interstitial deep defect levels and we get the smallest increments of deep defect levels at 60 min of LS in the sample *A*.

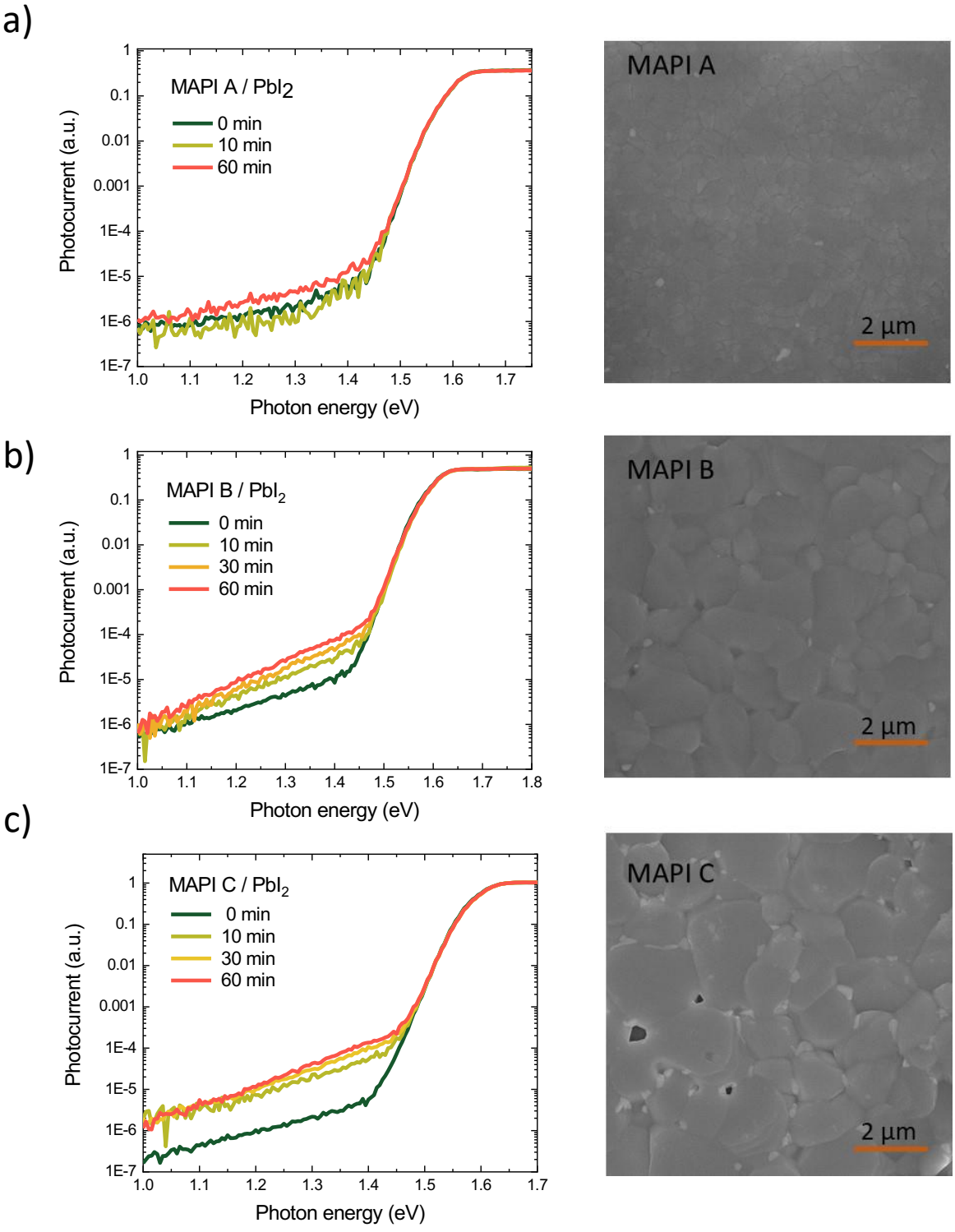

Fig. 55: Measurement on the structure MAPI/PbI_2 with varying grain sizes of MAPI thin films. On the left side is evolution of MAPI thin film FTPS after LS by 420 nm LED from the PbI_2 side. On the right side is SEM image of the corresponding MAPI thin film.

6.9 Conclusion: Phase segregation in mixed-halide perovskites

We studied the phase segregation process occurring in $FA_{0.83}Cs_{0.17}Pb(I_{0.6}Br_{0.4})_3$ solar cells caused by light-soaking. Whole devices with FA- and Cs- based mixed-halide perovskites exhibited a slower phase segregation compared to literature observations reported in [29], [78], [130] for $MAPb(I_x,Br_y)_3$ thin films. The slow process observed here enabled us to record that the generally observed I-rich terminal phase ($I_{0.8}Br_{0.2}$) is preceded by an even lower bandgap phase ($I_{0.9}Br_{0.1}$). Several samples, however, do not segregate to the I-rich phase ($I_{0.8}Br_{0.2}$), even at longer times of LS. The different patterns of phase segregation, with variations in the iodine content of the terminal phase, are likely to result from differences in the perovskite grain size. FTPS spectra further reveal that deep defects form in $FA_{0.83}Cs_{0.17}Pb(I_{0.6}Br_{0.4})_3$ solar cells under continuous illumination. A correlation between phase segregation rate and deep defect formation suggests that light-induced deep defects promote phase segregation by acting as the main halide migration channel. We connect phase segregation with iodine transport via interstitial sites. Light-induced halide interstitials were shown to passivate stronger recombination centres connected with surface grain boundaries, similarly as in MAPB single crystals in section 5.4. Based on our results, an effective way to suppress or even fully reverse phase segregation may be to reduce the perovskite grain size.

Most of the above-presented results from section 6 were published in the article *Ridzonova et al., J. Mater. Chem. A, 2022* [182].

7. Conclusion

The thesis is based on the application of photocurrent measurements in semiconductor material research. First, we focused on the space-charge-related effects in CdZnTe detectors and developed SCLP1, SCLP2, and drift-diffusion models (sections 2.4 - 2.6) for space-charge limited photocurrents. The numerical drift-diffusion model gives us a detailed picture of the CdZnTe defect structure (Table 1) and explains consistently all measured data, including photo-current voltage characteristics and transient current measurements in dark and under continuous illumination. A linear photocurrent onset at low voltages, observed also in other works, was connected with anode hole injection. Besides detail analysis, we propose a simple method to determine the average space-charge density from the SCLP1 model at a certain voltage. This may be helpful for the rapid evaluation of unwanted charging, which is still an ongoing issue of CdZnTe radiation detectors. By numerical simulations, we further show that steady-state photocurrent measurements cannot be used to credibly evaluate the carrier lifetime as well as other carrier dynamic parameters. Phenomena such as photoconductive gain and invisibility of certain shallow levels lead to lower $\mu_e\tau_e$, while space charge formation from trapped photoelectrons to larger $\mu_e\tau_e$. We propose to complete steady-state photocurrent measurements by transient current technique or alpha spectroscopy measurements. Moreover, we explain the non-saturation of PV characteristics by persisting surface recombination and photoconductive gain.

In section 5, we studied the transport properties of MAPI and MAPB perovskite single crystals with an emphasis on light-induced changes. A strong ion migration under DC bias was observed. Using pulsed-bias L-TCT we obtained for MAPB single crystals a mobility-lifetime product of 6 x 10^{-4} cm^2V^{-1}, hole mobility of 18 $cm^2V^{-1}s^{-1}$, and lifetime of 33 µs. Based on photocurrents, L-TCT, and PDS measurements we suggest the formation of mobile Frenkel pairs, Br_i^- and V_{Br}^+ under continuous above-bandgap illumination. We demonstrated that such illumination increases charge carrier collection thanks to reduced surface recombination and hole lifetime improvement. The light-induced suppression of surface recombination is explained by the local increase of internal electric field under an illuminated anode

due to the negative space charge from trapped photo-electrons or accumulated Br_i^- interstitials. The hole lifetime improvement may originate from the shift of the Fermi energy level or the formation of new defects which passivate hole traps.

The light-soaked mixed-halide perovskites showed similarly, as MAPB crystals, the formation of deep defects under illumination, which we assigned to iodine interstitials. Similarly, as in MAPB crystals, it seems that iodine interstitials first passivate stronger recombination centres connected with surface grain boundaries before they start to act as deep defects. In section 6 we focused on the phase segregation process and as first showed that the generally observed I-rich terminal phase ($I_{0.8}Br_{0.2}$) is preceded by an even lower bandgap phase ($I_{0.9}Br_{0.1}$). Based on the correlation between phase segregation rate and deep defect formation, we suggested that the phase segregation mechanism consists of iodine transport via interstitial sites. Observed different patterns of phase segregation, varying in terminal phase, were shown to result from different grain sizes. An effective way to suppress phase segregation may be the reduction of perovskite grain size.

8. List of abbreviations

8.1 Greek symbols

α	absorption coefficient
β	quantum efficiency of photo-carrier formation
γ_e	transfer rate of electrons through electrode
γ_h	transfer rate of holes through electrode
Δ	optical path difference, retardation
ε_0	vacuum permittivity
ε_r	relative permittivity
θ	ratio of free and trapped electrons density
λ	light wavelength
μ_e	electron mobility
ν	photon frequency
π	Ludolphine number 3.14159
ρ	space charge density
σ_0	conductivity in the dark
τ_e	electron lifetime

8.2 Latin symbols

a	linear slope of internal electric field
D_e	Einstein electron diffusion coefficient
Br_i^-	bromine interstitial
e	electron elementary charge
E	internal electric field
E_C	conduction band
E_V	valence band
E_F	Fermi level
E_g	bandgap energy
E_0	internal electric field under irradiated electrode

G	number of photo-generated electrons per second in the volume unit
h	Planc constant
I_i	iodine interstitial
j	total current density
J_0	constant given by equation (2.19)
k_B	Boltzmann constant
L	thickness of the sample
m_e^*	effective mass of electron in E_C
n	free electron concentration
p	free hole density
s_e	electron surface recombination velocity
S	surface of illuminated area
T	absolute temperature
V_{Br}^+	bromine vacancy
V_I	iodine vacancy
x	location of the creation of electron-hole pair

8.3 Abbreviations

AM1.5G	standard solar spectrum of intensity of 1000 Wm^{-2}
CCE	charge collection efficiency
CdTe	cadmium telluride
CdZnTe/CZT	cadmium zinc telluride
CWF	transient current waveforms
DC	direct current
DDF	drift-diffusion model
DMF	N,N-Dimethylformamide
FA	formamidinium (CH_4N_2)
FTPS	Fourier-transform photocurrent spectroscopy
LED	light-emitting diode
LD	laser diode

LTCT	laser-induced transient current
MA	methylammonium (CH_3NH_3)
MAPI	methylammonium lead iodide $CH_3NH_3PbI_3$
MAPB	methylammonium lead bromide $CH_3NH_3PbBr_3$
MPP	maximum power point
OC	open-circuit
PV	photocurrent-voltage characteristic
SC	short-circuit
SCLP	space-charge limited photocurrents

9. List of authors publications

i. K. Ridzonova et al. Correlating light-induced deep defects and phase segregation in mixed-halide perovskites. Journal of Materials Chemistry A, 2022

ii. K. Ridzonova et al. Space charge limited photocurrents and transient currents in CdZnTe radiation detectors. Physical Review Applied, 2020

iii. K. Ridzonova et al. Influence of golden nanoparticles on the incorporation of Eu^{2+} into BaI_2 and defect concentration. Crystals, 2023

iv. A. Musiienko et al. Deep Levels, charge transport and mixed conductivity in organometallic halide perovskites. Energy and Environmental Science, 2019

v. J. Holovský et al. Below the Urbach Edge: Solar Cell Loss Analysis Based on Full External Quantum Efficiency Spectra. ACS Energy Letters, 2023

vi. J. Zazvorka et al. Inhomogeneous resistivity and its effect on CdZnTe-based radiation detectors operating at high radiation fluxes. Journal of Physics D Applied Physics, 2019

vii. A. Amalathas et al. Unveiling the Effect of Potassium Treatment on the Mesoporous TiO_2/Perovskite Interface in Perovskite Solar Cells. ACS Applied Energy Materials, 2021

viii. J. Holovský et al. Pulsed laser deposition of high-transparency molybdenum oxide thin films. Vacuum, 2021

ix. M. Buryi et al. Charge traps in Zn- and Mo-based oxide microstructures. The role of Mo. Journal of Physics: Conference Series, 2022

x. M. Buryi et al. Peculiarities of erbium incorporation into ZnO microrods at high doping level leading to upconversion and the morphology change. Influence on excitonic as well as shallow donor states. Applied Surface Science, 2023

xi. M. Buryi et al. The role of Er^{3+} content in the luminescence properties of $Y_3Al_5O_{12}$ single crystal: Incorporation into the lattice and defect states creation. Crystals, 2023

xii. M. Buryi et al. Effect of UV Irradiation on the Growth of ZnO:Er Nanorods and Their Intrinsic Defects. Chemosensors, 2023

xiii. M. Buryi et al. Changes to Material Phase and Morphology Due to High-Level Molybdenum Doping of ZnO Nanorods: Influence on Luminescence and Defects. Materials, 2023

xiv. J. Hrabovský et al. Correlated EPR and optical study of charge trapping phenomena in tellurite glasses. The role of barium oxide. Journal of Non-Crystalline Solids, 2023

10. Bibliography

[1] M. Spahn, "X-ray detectors in medical imaging," *Nucl. Instruments Methods Phys. Res. A*, vol. 731, pp. 57–63, 2013, doi: 10.1016/j.nima.2013.05.174.

[2] X. Duan, J. Cheng, L. Zhang, Y. Xing, Z. Chen, and Z. Zhao, "X-ray cargo container inspection system with few-view projection imaging," *Nucl. Instruments Methods Phys. Res. A*, vol. 598, no. 2, pp. 439–444, 2009, doi: 10.1016/j.nima.2008.08.151.

[3] R. P. Haff and N. Toyofuku, "X-ray detection of defects and contaminants in the food industry," *Sens. Instrum. Food Qual. Saf.*, vol. 2, no. 4, pp. 262–273, 2008, doi: 10.1007/s11694-008-9059-8.

[4] G. Harding, "X-ray scatter tomography for explosives detection," *Radiat. Phys. Chem.*, vol. 71, no. 3–4, pp. 869–881, 2004, doi: 10.1016/j.radphyschem.2004.04.111.

[5] H. Wei and J. Huang, "Halide lead perovskites for ionizing radiation detection," *Nat. Commun.*, vol. 10, no. 1, pp. 1–12, 2019, doi: 10.1038/s41467-019-08981-w.

[6] J. Franc and P. Hoschl, "Fyzika polovodičů pro optoelektroniku I," 2007. [Online]. Available: http://fu.mff.cuni.cz/semicond/files/courses/Francskriptum.pdf.

[7] E. C. Lin, "Radiation risk from medical imaging," *Mayo Clin. Proc.*, vol. 85, no. 12, pp. 1142–1146, 2010, doi: 10.4065/mcp.2010.0260.

[8] O. Limousin, "New trends in CdTe and CdZnTe detectors for X- and gamma-ray applications," *Nucl. Instruments Methods Phys. Res. Sect. A Accel. Spectrometers, Detect. Assoc. Equip.*, vol. 504, no. 1–3, pp. 24–37, 2003, doi: 10.1016/S0168-9002(03)00745-9.

[9] D. de Nobel, "Phase equilibria and semiconducting properties of cadmium telluride," *Philips Res. Reports*, vol. 14, pp. 361–399, 1959.

[10] J. Low, M. Kreider, D. Pulsifer, A. Jones, and T. Gilani, "Band Gap Energy in Silicon," *Am. J. Undergrad. Res.*, vol. 7, no. 1, 2008, doi: 10.33697/ajur.2008.010.

[11] F. Zhang, C. Herman, Z. He, G. De Geronimo, E. Vernon, and J. Fried, "Characterization of the H3D ASIC readout system and 6.0 cm 3 3-D position sensitive CdZnTe detectors," *IEEE Trans. Nucl. Sci.*, vol. 59, no. 1 PART 2, pp. 236–242, 2012, doi: 10.1109/TNS.2011.2175948.

[12] R. J. Cooper, M. Amman, P. N. Luke, and K. Vetter, "A prototype High Purity Germanium detector for high resolution gamma-ray spectroscopy at high count rates," *Nucl. Instruments Methods Phys. Res. Sect. A Accel. Spectrometers, Detect. Assoc. Equip.*, vol. 795, pp. 167–173, 2015, doi:

10.1016/j.nima.2015.05.053.

[13] A. Tanaka, Y. Masa, S. Seto, and T. Kawasaki, “Zinc and selenium co-doped CdTe substrates lattice matched to HgCdTe,” *J. Cryst. Growth*, vol. 94, pp. 166–170, 1989.

[14] S. Del Sordo, L. Abbene, E. Caroli, A. M. Mancini, A. Zappettini, and P. Ubertini, “Progress in the Development of CdTe and CdZnTe Semiconductor Radiation Detectors for Astrophysical and Medical Applications,” *Sensors*, vol. 9, pp. 3491–3526, 2009, doi: 10.3390/s90503491.

[15] N. Gehrels *et al.*, “THE SWIFT GAMMA-RAY BURST MISSION,” pp. 1005–1020, 2004.

[16] M. A. Scarpulla *et al.*, “CdTe-based thin film photovoltaics: Recent advances, current challenges and future prospects,” *Sol. Energy Mater. Sol. Cells*, vol. 255, no. August 2022, p. 112289, 2023, doi: 10.1016/j.solmat.2023.112289.

[17] A. Vigneswaran, M. S. Majid, H. A. Rahman, M. Y. Hassan, and M. K. Hamzah, “Cost comparison between amorphous silicon and cadmium telluride for stand-alone photovoltaic system in Malaysia,” *PECon 2008 - 2008 IEEE 2nd Int. Power Energy Conf.*, no. PECon 08, pp. 468–472, 2008, doi: 10.1109/PECON.2008.4762511.

[18] N. W. Harris, J. G. Grimm, and R. S. Eng, “Wideband long-pulse operation of an efficient electro-optic modulator at 106 μm,” *Opt. Lett.*, vol. 15, no. 20, p. 1156, 1990, doi: 10.1364/ol.15.001156.

[19] H. Wiedemeier, Y. R. Ge, M. A. Hutchins, and Y. G. Sha, “Growth of Hg1-xCdxTe epitaxial layers on (100) CdTe by chemical vapor transport under normal and reduced gravity conditions,” *J. Cryst. Growth*, vol. 146, no. 1–4, pp. 610–618, 1995, doi: 10.1016/0022-0248(94)00578-8.

[20] R. TRIBOULET and G. Neu, “GROWTH AND CHARACTERIZATION OF THE COMPLETE CdZnTe ALLOY SERIES,” *J. Cryst. Growth*, vol. 65, pp. 262–269, 1983.

[21] P. Cheuvart, U. El-Hanani, D. Schneider, and R. Triboulet, “Cdte and CdZnTe crystal growth by horizontal bridgman technique,” *J. Cryst. Growth*, vol. 101, no. 1–4, pp. 270–274, 1990, doi: 10.1016/0022-0248(90)90980-Y.

[22] M. Bruder, H. J. Schwarz, R. Schmitt, and H. Maier, “VERTICAL BRIDGMAN GROWTH OF CdZnTe AND CHARACTERIZATION OF SUBSTRATES FOR USE IN Hg11Cd1Te LIQUID PHASE EPITAXY,” *J. Cryst. Growth*, vol. 101, pp. 266–269, 1990.

[23] R. B. Lauer and F. Williams, “Photoelectronic properties of graded composition crystals of II-VI semiconductors,” *J. Appl. Phys.*, vol. 42, no. 7, pp. 2904–2910, 1971, doi: 10.1063/1.1660647.

[24] F. P. Doty, J. F. Butler, and J. F. Schetzina, “Properties of CdZnTe crystals grown by a high pressure Bridgman method,” *J. Vac. Sci. Technol. B*, vol. 10, no. 4, p. 1418, 1992, doi: 10.1116/1.586264.

[25] M. D. Alam, S. S. Nasim, and S. Hasan, “Recent progress in CdZnTe based room temperature detectors for nuclear radiation monitoring,” *Prog. Nucl. Energy*, vol. 140, no. July, 2021, doi: 10.1016/j.pnucene.2021.103918.

[26] T. E. Schlesinger *et al.*, “Cadmium zinc telluride and its use as a nuclear radiation detector material,” *Mater. Sci. Eng. R Reports*, vol. 32, no. 4–5, pp. 103–189, 2001, doi: 10.1016/S0927-796X(01)00027-4.

[27] D. Weber, “$CH_3NH_3PbX_3$, ein Pb(II)-System mit kubischer Perowskitstruktur / $CH_3NH_3PbX_3$, a Pb(II)-System with Cubic Perovskite Structure,” *Zeitschrift für Naturforsch. B*, vol. 33, no. 12, pp. 1443–1445, 1978, [Online]. Available: https://www.degruyter.com/document/doi/10.1515/znb-1978-1214/html.

[28] M. C. Brennan, S. Draguta, P. V. Kamat, and M. Kuno, “Light-Induced Anion Phase Segregation in Mixed Halide Perovskites,” *ACS Energy Lett.*, vol. 3, no. 1, pp. 204–213, 2018, doi: 10.1021/acsenergylett.7b01151.

[29] E. T. Hoke, D. J. Slotcavage, E. R. Dohner, A. R. Bowring, H. I. Karunadasa, and M. D. McGehee, “Reversible photo-induced trap formation in mixed-halide hybrid perovskites for photovoltaics,” *Chem. Sci.*, vol. 6, no. 1, pp. 613–617, 2015, doi: 10.1039/c4sc03141e.

[30] J. H. Noh, S. H. Im, J. H. Heo, T. N. Mandal, and S. Il Seok, “Chemical management for colorful, efficient, and stable inorganic-organic hybrid nanostructured solar cells,” *Nano Lett.*, vol. 13, no. 4, pp. 1764–1769, 2013, doi: 10.1021/nl400349b.

[31] M. C. Brennan, A. Ruth, P. V. Kamat, and M. Kuno, “Photoinduced Anion Segregation in Mixed Halide Perovskites,” *Trends Chem.*, vol. 2, no. 4, pp. 282–301, 2020, doi: 10.1016/j.trechm.2020.01.010.

[32] E. Bi, Z. Song, C. Li, Z. Wu, and Y. Yan, “Mitigating ion migration in perovskite solar cells,” *Trends Chem.*, vol. 3, no. 7, pp. 575–588, 2021, doi: https://doi.org/10.1016/j.trechm.2021.04.004.

[33] H. J. Snaith, “Perovskites: The emergence of a new era for low-cost, high-efficiency solar cells,” *J. Phys. Chem. Lett.*, vol. 4, no. 21, pp. 3623–3630, 2013, doi: 10.1021/jz4020162.

[34] S. D. Stranks *et al.*, “Electron-Hole Diffusion Lengths Exceeding 1 Micrometer in an Organometal Trihalide Perovskite Absorber,” *Science (80-.).*, vol. 342, pp. 1–5, 2013.

[35] G. Xing, N. Mathews, S. S. Lim, Y. M. Lam, S. Mhaisalkar, and T. C. Sum, “Long-Range Balanced Electron- and Hole-Transport Lengths in Organic-Inorganic CH3NH3PbI3,” vol. 6960, no. October, pp. 498–500, 2013.

[36] S. De Wolf *et al.*, “Organometallic halide perovskites: Sharp optical absorption edge and its relation to photovoltaic performance,” *J. Phys. Chem. Lett.*, vol. 5, no. 6, pp. 1035–1039, 2014, doi: 10.1021/jz500279b.

[37] K. X. Steirer *et al.*, “Defect Tolerance in Methylammonium Lead Triiodide Perovskite,” *ACS Energy Lett.*, vol. 1, no. 2, pp. 360–366, 2016, doi:

10.1021/acsenergylett.6b00196.

[38] T. Wu *et al.*, “The Main Progress of Perovskite Solar Cells in 2020–2021,” *Nano-Micro Lett.*, vol. 13, no. 1, p. 18, 2021, doi: 10.1007/s40820-021-00672-w.

[39] G. Grancini *et al.*, “One-Year stable perovskite solar cells by 2D/3D interface engineering,” *Nat. Commun.*, vol. 8, pp. 1–8, 2017, doi: 10.1038/ncomms15684.

[40] W. Tress, N. Marinova, T. Moehl, S. M. Zakeeruddin, M. K. Nazeeruddin, and M. Grätzel, “Understanding the rate-dependent J-V hysteresis, slow time component, and aging in CH3NH3PbI3 perovskite solar cells: The role of a compensated electric field,” *Energy Environ. Sci.*, vol. 8, no. 3, pp. 995–1004, 2015, doi: 10.1039/c4ee03664f.

[41] H. S. Kim *et al.*, “Control of I-V Hysteresis in CH3NH3PbI3 Perovskite Solar Cell,” *J. Phys. Chem. Lett.*, vol. 6, no. 22, pp. 4633–4639, 2015, doi: 10.1021/acs.jpclett.5b02273.

[42] X. Yan *et al.*, “Ion migration in hybrid perovskites: Classification, identification, and manipulation,” *Nano Today*, vol. 44, p. 101503, 2022, doi: 10.1016/j.nantod.2022.101503.

[43] Y. Yuan *et al.*, “Photovoltaic Switching Mechanism in Lateral Structure Hybrid Perovskite Solar Cells,” *Adv. Energy Mater.*, vol. 5, no. 15, pp. 1–7, 2015, doi: 10.1002/aenm.201500615.

[44] T. Duong *et al.*, “Light and Electrically Induced Phase Segregation and Its Impact on the Stability of Quadruple Cation High Bandgap Perovskite Solar Cells,” *ACS Appl. Mater. Interfaces*, vol. 9, no. 32, pp. 26859–26866, 2017, doi: 10.1021/acsami.7b06816.

[45] H. Zhang *et al.*, “Phase segregation due to ion migration in all-inorganic mixed-halide perovskite nanocrystals,” *Nat. Commun.*, vol. 10, no. 1, pp. 1–8, 2019, doi: 10.1038/s41467-019-09047-7.

[46] S. Draguta *et al.*, “Rationalizing the light-induced phase separation of mixed halide organic-inorganic perovskites,” *Nat. Commun.*, vol. 8, no. 1, 2017, doi: 10.1038/s41467-017-00284-2.

[47] A. J. Barker *et al.*, “Defect-Assisted Photoinduced Halide Segregation in Mixed-Halide Perovskite Thin Films,” *ACS Energy Lett.*, vol. 2, no. 6, pp. 1416–1424, 2017, doi: 10.1021/acsenergylett.7b00282.

[48] A. F. Gualdrón-Reyes *et al.*, “Controlling the Phase Segregation in Mixed Halide Perovskites through Nanocrystal Size,” *ACS Energy Lett.*, vol. 4, no. 1, pp. 54–62, 2019, doi: 10.1021/acsenergylett.8b02207.

[49] R. Grill *et al.*, “Polarization study of defect structure of CdTe radiation detectors,” *IEEE Trans. Nucl. Sci.*, vol. 58, no. 6 PART 2, pp. 3172–3181, 2011, doi: 10.1109/TNS.2011.2165730.

[50] Y. Cui, M. Groza, D. Hillman, A. Burger, and R. B. James, “Study of surface recombination velocity of CdZnTe radiation detectors by direct current photoconductivity,” *J. Appl. Phys.*, vol. 92, no. 5, p. 2556, 2002, doi: 10.1063/1.1497696.

[51] Y. Cui, G. W. Wright, X. Ma, K. Chattopadhyay, R. B. James, and A. Burger, “DC Photoconductivity Study of Semi-insulating CdZnTe Crystals,” *J. Electron. Mater.*, vol. 30, no. 6, pp. 774–778, 2001.

[52] Y. Ling *et al.*, “Carrier transport performance of CdZnTe detector by direct current photoconductive technology,” *J. Appl. Phys.*, vol. 121, p. 34502, 2017, doi: 10.1063/1.4974201.

[53] M. Zanichelli, M. Pavesi, A. Zappettini, L. Marchini, N. Auricchio, and E. Caroli, “Characterization of Bulk and Surface Transport Mechanisms by Means of the Photocurrent Technique,” *IEEE Trans. Nucl. Sci.*, vol. 56, no. 6, pp. 3591–3596, 2009.

[54] Y. Cui *et al.*, “Characterization of Cd1 – xZnxTe Crystals Grown from a Modified Vertical Bridgman Technique,” *J. Electron. Mater.*, vol. 35, no. 6, pp. 1267–1274, 2006.

[55] L. Bao, G. Zha, B. Zhang, J. Dong, Y. Li, and W. Jie, “Investigation of neutron irradiation effects on the properties of Au/CdZnTe junction,” *Vacuum*, vol. 167, pp. 340–343, 2019, doi: 10.1016/j.vacuum.2019.06.028.

[56] M. Zanichelli *et al.*, “Characterization of Bulk and Surface Transport Mechanisms by Means of the Photocurrent Technique,” *IEEE Trans. Nucl. Sci.*, vol. 56, no. 6, pp. 3591–3596, 2009.

[57] Z. Burshtein, J. K. Akujieze, and E. Silberman, “Carrier surface generation and recombination effects in photoconduction of HgI2 single crystals,” *J. Appl. Phys.*, vol. 60, no. 9, pp. 3182–3187, 1986, doi: 10.1063/1.337733.

[58] A. Levi, M. M. Schieber, and Z. Burshtein, “Carrier surface recombination in HgI2 photon detectors,” *J. Appl. Phys.*, vol. 54, no. 5, pp. 2472–2476, 1983, doi: 10.1063/1.332363.

[59] S. Wang *et al.*, “Crystal Growth of Tl4CdI6 : A Wide Band Gap Semiconductor for Hard Radiation Detection,” *Cryst. Growth Des.*, vol. 14, pp. 2401–2410, 2014, doi: 10.1021/cg5001446.

[60] A. C. Wibowo *et al.*, “Photoconductivity in the Chalcohalide Semiconductor, SbSeI: a New Candidate for Hard Radiation Detection,” *Inorg. Chem.*, vol. 52, pp. 7045–7050, 2013, doi: 10.1021/ic401086r.

[61] S. L. Nguyen *et al.*, “Photoconductivity in Tl6SI4 : A Novel Semiconductor for Hard Radiation Detection,” *Chem. Mater.*, vol. 25, pp. 2868–2877, 2013, doi: 10.1021/cm401406j.

[62] S. M. Islam *et al.*, “Cs2Hg3S4 : A Low-Dimensional Direct Bandgap Semiconductor,” *Chem. Mater.*, vol. 27, pp. 370–378, 2015, doi: 10.1021/cm504089r.

[63] S. J. Grenadier, A. Maity, J. Li, J. Y. Lin, and H. X. Jiang, “Origin and roles of oxygen impurities in hexagonal boron nitride epilayers,” *Appl. Phys. Lett.*, vol. 112, p. 162103, 2018, doi: 10.1063/1.5026291.

[64] K. Ahmed, R. Dahal, A. Weltz, J. J. Lu, Y. Danon, and I. B. Bhat, “Solid-state neutron detectors based on thickness scalable hexagonal boron nitride,” *Appl. Phys. Lett.*, vol. 110, p. 23503, 2017, doi: 10.1063/1.4973927.

[65] A. Maity *et al.*, “Hexagonal boron nitride neutron detectors with high detection efficiencies,” vol. 44501, 2018, doi: 10.1063/1.5017979.

[66] A. Maity, S. J. Grenadier, J. Li, J. Y. Lin, and H. X. Jiang, “Toward achieving flexible and high sensitivity hexagonal boron nitride neutron detectors,” *Appl. Phys. Lett.*, vol. 111, no. 2017, p. 33507, 2018, doi: 10.1063/1.4995399.

[67] A. Maity, S. J. Grenadier, J. Li, J. Y. Lin, and H. X. Jiang, “High sensitivity hexagonal boron nitride lateral neutron detectors,” *Appl. Phys. Lett.*, vol. 114, no. 22, p. 222102, 2019, doi: 10.1063/1.5098331.

[68] W. Zheng, R. Lin, Z. Zhang, Q. Liao, J. Liu, and F. Huang, “An ultrafast-temporally-responsive flexible photodetector with high sensitivity based on high-crystallinity organic–inorganic perovskite nanoflake,” *Nanoscale*, vol. 9, pp. 12718–12726, 2017, doi: 10.1039/c7nr04395c.

[69] Z. Yang *et al.*, “Engineering the Exciton Dissociation in Quantum-Confined 2D CsPbBr3 Nanosheet Films,” *Adv. Funct. Mater.*, vol. 28, p. 1705908, 2018, doi: 10.1002/adfm.201705908.

[70] A. J. Knight and L. M. Herz, “Preventing phase segregation in mixed-halide perovskites: a perspective,” *Energy Environ. Sci.*, vol. 13, pp. 2024–2046, 2020, doi: 10.1039/d0ee00788a.

[71] I. L. Braly *et al.*, “Current-Induced Phase Segregation in Mixed Halide Hybrid Perovskites and its Impact on Two-Terminal Tandem Solar Cell Design,” *ACS Energy Lett.*, vol. 2, no. 8, pp. 1841–1847, 2017, doi: 10.1021/acsenergylett.7b00525.

[72] P. Vashishtha and J. E. Halpert, “Field-Driven Ion Migration and Color Instability in Red-Emitting Mixed Halide Perovskite Nanocrystal Light-Emitting Diodes,” *Chem. Mater.*, vol. 29, no. 14, pp. 5965–5973, 2017, doi: 10.1021/acs.chemmater.7b01609.

[73] Y. Shynkarenko *et al.*, “Direct synthesis of quaternary alkylammonium-capped perovskite nanocrystals for efficient blue and green light-emitting diodes,” *ACS Energy Lett.*, vol. 4, no. 11, pp. 2703–2711, 2019, doi: 10.1021/acsenergylett.9b01915.

[74] R. A. Belisle, K. A. Bush, L. Bertoluzzi, A. Gold-Parker, M. F. Toney, and M. D. McGehee, “Impact of surfaces on photoinduced halide segregation in mixed-halide perovskites,” *ACS Energy Lett.*, vol. 3, no. 11, pp. 2694–2700, 2018, doi: 10.1021/acsenergylett.8b01562.

[75] M. Hu, C. Bi, Y. Yuan, Y. Bai, and J. Huang, “Stabilized wide bandgap

MAPbBrxI3-x perovskite by enhanced grain size and improved crystallinity," *Adv. Sci.*, vol. 3, no. 6, pp. 6–11, 2015, doi: 10.1002/advs.201500301.

[76] J. Xu *et al.*, "Triple-halide wide-band gap perovskites with suppressed phase segregation for efficient tandems," *Science (80-.).*, vol. 367, no. 6482, pp. 1097–1104, 2020, doi: 10.1126/science.aaz4639.

[77] W. Rehman *et al.*, "Photovoltaic mixed-cation lead mixed-halide perovskites: Links between crystallinity, photo-stability and electronic properties," *Energy Environ. Sci.*, vol. 10, no. 1, pp. 361–369, 2017, doi: 10.1039/c6ee03014a.

[78] A. Ruth *et al.*, "Vacancy-Mediated Anion Photosegregation Kinetics in Mixed Halide Hybrid Perovskites: Coupled Kinetic Monte Carlo and Optical Measurements," *ACS Energy Lett.*, vol. 3, no. 10, pp. 2321–2328, 2018, doi: 10.1021/acsenergylett.8b01369.

[79] S. J. Yoon, M. Kuno, and P. V. Kamat, "Shift Happens. How Halide Ion Defects Influence Photoinduced Segregation in Mixed Halide Perovskites," *ACS Energy Lett.*, vol. 2, no. 7, pp. 1507–1514, 2017, doi: 10.1021/acsenergylett.7b00357.

[80] X. Tang *et al.*, "Local Observation of Phase Segregation in Mixed-Halide Perovskite," *Nano Lett.*, vol. 18, no. 3, pp. 2172–2178, 2018, doi: 10.1021/acs.nanolett.8b00505.

[81] K. Datta *et al.*, "Effect of Light-Induced Halide Segregation on the Performance of Mixed-Halide Perovskite Solar Cells," *Appl. Energy Mater.*, vol. 4, no. 7, pp. 6650–6658, 2021, doi: 10.1021/acsaem.1c00707.

[82] R. H. Bube, *Photoelectronic Properties of Semiconductors*, 1st EDN. Cambridge University Press, 1992.

[83] A. Many, "High-Field Effects in Photoconducting Cadmium Sulphide," *J. Phys. Chem. Solids*, vol. 26, pp. 575–585, 1965.

[84] N. F. Mott and R. W. Gurney, *Electronic Processes in Ionic Crystals*, 2nd EDN. Dover Publications Inc., 1964.

[85] F. J. Chatenier, "Space-charge-limited photocurrent in vapour-deposited layers of red lead monoxide," *Philips Res. Repts*, vol. 23, pp. 142–150, 1968.

[86] M. Lavagna, J. P. Pique, and Y. Marfaing, "Theoretical analysis of the quantum photoelectric yield in Schottky diodes," *Solid State Electron.*, vol. 20, no. 3, pp. 235–240, 1977, doi: 10.1016/0038-1101(77)90190-3.

[87] D. Gutkowicz-Krusin, "On the carrier collection efficiency of amorphous silicon hydride schottky barrier solar cells: Effects of recombination," *J. Appl. Phys.*, vol. 52, no. 8, pp. 5370–5376, 1981, doi: 10.1063/1.329397.

[88] J. R. Haynes and W. Shockley, "The mobility and life of injected holes and electrons in germanium," *Phys. Rev.*, vol. 81, no. 5, pp. 835–843, 1951, doi: 10.1103/PhysRev.81.835.

[89] Š. Uxa, E. Belas, R. Grill, P. Praus, and R. B. James, "Determination of Electric-

Field Profile in CdTe and CdZnTe Detectors Using Transient-Current Technique," *IEEE Trans. Nucl. Sci.*, vol. 59, no. 5, pp. 2402–2408, 2012.

[90] P. Praus, E. Belas, J. Bok, R. Grill, and J. Pekárek, "Laser Induced Transient Current Pulse Shape Formation in (CdZn)Te Detectors," *IEEE Trans. Nucl. Sci.*, vol. 63, no. 1, pp. 246–251, 2016.

[91] G. Cavalleri, E. Fabri, E. Gatti, and V. Svelto, "On the induced charge in semiconductor detectors," *Nucl. Instruments Methods*, vol. 21, pp. 177–178, 1963.

[92] C. Canali, F. Nava, and L. Reggiani, "Drift velocity and diffusion coefficients from time-of-flight measurements," in *Topics in Applied Physics 58, Hot–Electron transport in Semiconductors*, 1st ed., New York: Springer US, 1985, pp. 87–112.

[93] K. Suzuki, T. Sawada, and K. Imai, "Effect of DC Bias Field on the Time-of-Flight Current Waveforms of CdTe and CdZnTe Detectors," *IEEE Trans. Nucl. Sci.*, vol. 58, no. 4, pp. 1958–1963, 2011.

[94] A. P. Letters, A. Cola, I. National, I. Farella, and I. National, "The polarization mechanism in CdTe Schottky detectors The polarization mechanism in CdTe Schottky detectors," no. October 2016, pp. 1–5, 2009, doi: 10.1063/1.3099051.

[95] Š. Uxa, "Transport and optical properties of CdTe / CdZnTe single crystals," Charles University in Prague, 2014.

[96] K. Hecht, "Zum Mechanismus des lichtelektrischen Primarstromes in isolierenden Kristallen.," *Zeitschrift fur Phys.*, vol. 77, no. 3–4, pp. 235–245, 1932.

[97] J. Pekarek, "Room-temperature semiconducting detectors," Charles University, 2017.

[98] P. Praus, E. Belas, J. Franc, R. Grill, P. Höschl, and J. Pekárek, "Electronic Pulse Shape Formation in Transient Charge and Transient Current Detection Approach in (CdZn)Te Detectors," *IEEE Trans. Nucl. Sci.*, vol. 61, no. 4, pp. 2333–2337, 2014.

[99] K. Ridzoňová, "Charge transport optical characterization in semiconductor radiation detectors," Charles University, 2016.

[100] H. Jongbloets, J. Stoelinga, M. van de Steeg, and P. Wyder, "Temperature dependence of the photothermal conductivity of high-purity germanium containing very low concentrations of Al, B and P," *Phys. Rev. B*, vol. 20, no. 8, 1979.

[101] M. Vanecek and A. Poruba, "Fourier-transform photocurrent spectroscopy of microcrystalline silicon for solar cells," *Appl. Phys. Lett.*, vol. 80, no. 5, pp. 719–721, 2002, doi: 10.1063/1.1446207.

[102] J. Holovský, A. Poruba, A. Purkrt, Z. Remeš, and M. Vaněček, "Comparison of

photocurrent spectra measured by FTPS and CPM for amorphous silicon layers and solar cells," *J. Non. Cryst. Solids*, vol. 354, no. 19–25, pp. 2167–2170, 2008, doi: 10.1016/j.jnoncrysol.2007.09.106.

[103] M. Vanecek and A. Poruba, "Fourier transform photocurrent spectroscopy applied to a broad variety of electronically active thin films (silicon, carbon, organics)," *Thin Solid Films*, vol. 515, no. 19 SPEC. ISS., pp. 7499–7503, 2007, doi: 10.1016/j.tsf.2006.11.145.

[104] X. Liu, "Fourier Transform Interferometer," 2012. http://www.physics.drexel.edu/~bob/Term_Reports/Liu_2012.pdf (accessed Jul. 25, 2023).

[105] D. Wang, M. Wright, N. K. Elumalai, and A. Uddin, "Stability of perovskite solar cells," *Sol. Energy Mater. Sol. Cells*, vol. 147, pp. 255–275, 2016, doi: 10.1016/j.solmat.2015.12.025.

[106] W. Wang *et al.*, "Growth of mixed-halide perovskite single crystals," *CrystEngComm*, vol. 20, no. 12, pp. 1635–1643, 2018, doi: 10.1039/c7ce01691c.

[107] H. S. Rao, W. G. Li, B. X. Chen, D. Bin Kuang, and C. Y. Su, "In Situ Growth of 120 cm2 CH3NH3PbBr3 Perovskite Crystal Film on FTO Glass for Narrowband-Photodetectors," *Adv. Mater.*, vol. 29, no. 16, 2017, doi: 10.1002/adma.201602639.

[108] P. K. Nayak *et al.*, "Mechanism for rapid growth of organic-inorganic halide perovskite crystals," *Nat. Commun.*, vol. 7, pp. 1–8, 2016, doi: 10.1038/ncomms13303.

[109] D. Kranzer, "Mobility of Holes of Zinc-Blende III-V and II-VI Compounds," *Phys. Status Solidi*, vol. 26, p. 11, 1974.

[110] P. Horodyský and P. Hlídek, "Free-exciton absorption in bulk CdTe: Temperature dependence," *Phys. Status Solidi Basic Res.*, vol. 243, no. 2, pp. 494–501, 2006, doi: 10.1002/pssb.200541402.

[111] K. Ahmed, R. Dahal, A. Weltz, J. J. Lu, Y. Danon, and I. B. Bhat, "Solid-state neutron detectors based on thickness scalable hexagonal boron nitride," *Appl. Phys. Lett.*, vol. 110, p. 23503, 2017, doi: 10.1063/1.4973927.

[112] S. F. Soares, "Photoconductive Gain in a Schottky Barrier Photodiode," *Jpn. J. Appl. Phys.*, vol. 31, pp. 210–216, 1992.

[113] J. Franc *et al.*, "Control of electric field in CdZnTe radiation detectors by above-bandgap light," *J. Appl. Phys.*, vol. 117, no. 16, p. 165702, 2015, doi: 10.1063/1.4919073.

[114] A. Musiienko, R. Grill, E. Belas, P. Praus, J. Pipek, and H. Elhadidy, "Characterization of polarizing semiconductor radiation detectors by laser-induced transient currents," *Appl. Phys. Lett.*, vol. 111, p. 8, 2017.

[115] S. J. Grenadier, A. Maity, J. Li, J. Y. Lin, and H. X. Jiang, "Origin and roles of

oxygen impurities in hexagonal boron nitride epilayers," *Appl. Phys. Lett.*, vol. 112, p. 162103, 2018, doi: 10.1063/1.5026291.

[116] A. Maity, S. J. Grenadier, J. Li, J. Y. Lin, and H. X. Jiang, "Hexagonal boron nitride neutron detectors with high detection efficiencies," *J. Appl. Phys.*, vol. 123, p. 44501, 2018, doi: 10.1063/1.5017979.

[117] A. E. Bolotnikov *et al.*, "Use of the drift-time method to measure the electron lifetime in long-drift-length CdZnTe detectors," *J. Appl. Phys.*, vol. 120, p. 104507, 2016.

[118] J. Zázvorka *et al.*, "Inhomogenous resistivity and its effect on CdZnTe-based radiation detectors operating at high radiation fluxes," *J. Phys. D. Appl. Phys.*, vol. 52, p. 325109, 2019.

[119] A. Cola and I. Farella, "Electric Field and Current Transport Mechanisms in Schottky CdTe X-ray Detectors under Perturbing Optical Radiation," pp. 9414–9434, 2013, doi: 10.3390/s130709414.

[120] P. G. Kasherininov, A. V Kichaev, and A. A. Tomasov, "Photoelectric phenomena in structures based on high-resistivity semiconductor crystals with a thin insulator layer at the semiconductor-metal boundary."

[121] M. Klingenstein *et al.*, "Photocurrent gain mechanisms in metal-semiconductor-metal photodetectors," *Solid State Electron.*, vol. 37, no. 2, pp. 333–340, 1994, doi: 10.1016/0038-1101(94)90086-8.

[122] F. Xie *et al.*, "Low dark current and internal gain mechanism of GaN MSM photodetectors fabricated on bulk GaN substrate," *Solid. State. Electron.*, vol. 57, no. 1, pp. 39–42, 2011, doi: 10.1016/j.sse.2010.12.005.

[123] B. Y. Zheng, Y. Wang, P. Nordlander, and N. J. Halas, "Color-Selective and CMOS-Compatible Photodetection Based on Aluminum Plasmonics," *Adv. Mater.*, vol. 26, no. 36, pp. 6318–6323, 2014, doi: 10.1002/adma.201401168.

[124] G. Kano *et al.*, "Photoconductive Gain in a Schottky Barrier Photodiode."

[125] A. Rebello and A. O. Adeyeye, "Robust electric-field tunable opto-electrical behavior in Pt-NiO-Pt planar structures," *Sci. Rep.*, vol. 6, no. June, pp. 1–8, 2016, doi: 10.1038/srep28007.

[126] K. Ridzonova, E. Belas, R. Grill, J. Pekarek, and P. Praus, "Space-charge-limited photocurrents and transient currents in (Cd,Zn)Te radiation detectors," *Phys. Rev. Appl.*, vol. 13, no. 6, p. 1, 2020, doi: 10.1103/PhysRevApplied.13.064054.

[127] A. Musiienko *et al.*, "Deep levels, charge transport and mixed conductivity in organometallic halide perovskites," *Energy Environ. Sci.*, vol. 12, no. 4, pp. 1413–1425, 2019, doi: 10.1039/c9ee00311h.

[128] C. Wehrenfennig, G. E. Eperon, M. B. Johnston, H. J. Snaith, and L. M. Herz, "High charge carrier mobilities and lifetimes in organolead trihalide perovskites," *Adv. Mater.*, vol. 26, no. 10, pp. 1584–1589, 2014, doi: 10.1002/adma.201305172.

[129] A. Musiienko *et al.*, “Deciphering the effect of traps on electronic charge transport properties of methylammonium lead tribromide perovskite,” *Sci. Adv.*, vol. 6, no. 37, 2020, doi: 10.1126/sciadv.abb6393.

[130] W. Rehman *et al.*, “Charge-Carrier Dynamics and Mobilities in Formamidinium Lead Mixed-Halide Perovskites,” *Adv. Mater.*, vol. 27, no. 48, pp. 7938–7944, 2015, doi: 10.1002/adma.201502969.

[131] H. Christiana and S. Bowden, “Standard Solar Spectra.” https://www.pveducation.org/pvcdrom/appendices/standard-solar-spectra (accessed Sep. 16, 2023).

[132] A. J. Knight *et al.*, “Electronic Traps and Phase Segregation in Lead Mixed-Halide Perovskite,” *ACS Energy Lett.*, vol. 4, no. 1, pp. 75–84, 2019, doi: 10.1021/acsenergylett.8b02002.

[133] A. J. Knight, J. B. Patel, H. J. Snaith, M. B. Johnston, and L. M. Herz, “Trap States, Electric Fields, and Phase Segregation in Mixed-Halide Perovskite Photovoltaic Devices,” *Adv. Energy Mater.*, vol. 10, no. 9, pp. 1–11, 2020, doi: 10.1002/aenm.201903488.

[134] S. Mahesh *et al.*, “Revealing the origin of voltage loss in mixed-halide perovskite solar cells,” *Energy Environ. Sci.*, vol. 13, no. 1, pp. 258–267, 2020, doi: 10.1039/c9ee02162k.

[135] M. Abdi-Jalebi *et al.*, “Maximizing and stabilizing luminescence from halide perovskites with potassium passivation,” *Nature*, vol. 555, no. 7697, pp. 497–501, 2018, doi: 10.1038/nature25989.

[136] J. Thiesbrummel *et al.*, “Universal Current Losses in Perovskite Solar Cells Due to Mobile Ions,” *Adv. Energy Mater.*, vol. 11, no. 34, 2021, doi: 10.1002/aenm.202101447.

[137] D. J. Slotcavage, H. I. Karunadasa, and M. D. McGehee, “Light-Induced Phase Segregation in Halide-Perovskite Absorbers,” *ACS Energy Lett.*, vol. 1, no. 6, pp. 1199–1205, 2016, doi: 10.1021/acsenergylett.6b00495.

[138] K. Domanski, E. A. Alharbi, A. Hagfeldt, M. Grätzel, and W. Tress, “Systematic investigation of the impact of operation conditions on the degradation behaviour of perovskite solar cells,” *Nat. Energy*, vol. 3, no. 1, pp. 61–67, 2018, doi: 10.1038/s41560-017-0060-5.

[139] K. Domanski *et al.*, “Migration of cations induces reversible performance losses over day/night cycling in perovskite solar cells,” *Energy Environ. Sci.*, vol. 10, no. 2, pp. 604–613, 2017, doi: 10.1039/c6ee03352k.

[140] M. Yuan *et al.*, “Perovskite energy funnels for efficient light-emitting diodes,” *Nat. Nanotechnol.*, vol. 11, no. 10, pp. 872–877, 2016, doi: 10.1038/nnano.2016.110.

[141] M. B. Johnston and L. M. Herz, “Hybrid Perovskites for Photovoltaics: Charge-Carrier Recombination, Diffusion, and Radiative Efficiencies,” *Acc. Chem. Res.*, vol. 49, no. 1, pp. 146–154, 2016, doi: 10.1021/acs.accounts.5b00411.

[142] F. Deschler *et al.*, “High photoluminescence efficiency and optically pumped lasing in solution-processed mixed halide perovskite semiconductors,” *J. Phys. Chem. Lett.*, vol. 5, no. 8, pp. 1421–1426, 2014, doi: 10.1021/jz5005285.

[143] P. Caprioglio *et al.*, “Nano-emitting Heterostructures Violate Optical Reciprocity and Enable Efficient Photoluminescence in Halide-Segregated Methylammonium-Free Wide Bandgap Perovskites,” *ACS Energy Lett.*, vol. 6, no. 2, pp. 419–428, 2021, doi: 10.1021/acsenergylett.0c02270.

[144] Z. Andaji-Garmaroudi *et al.*, “A Highly Emissive Surface Layer in Mixed-Halide Multication Perovskites,” *Adv. Mater.*, vol. 31, no. 42, 2019, doi: 10.1002/adma.201902374.

[145] H. Tsai *et al.*, “Light-induced lattice expansion leads to high-efficiency perovskite solar cells",” *Science (80-.).*, vol. 360, no. 6384, pp. 67–70, 2018, doi: 10.1126/science.aap8671.

[146] D. P. McMeekin *et al.*, “A mixed-cation lead mixed-halide perovskite absorber for tandem solar cells,” *Science (80-.).*, vol. 351, no. 6269, pp. 151–155, 2016, doi: 10.1126/science.aad5845.

[147] D. Di Girolamo *et al.*, “Ion Migration-Induced Amorphization and Phase Segregation as a Degradation Mechanism in Planar Perovskite Solar Cells,” *Adv. Energy Mater.*, vol. 10, no. 25, p. 2000310, 2020, doi: 10.1002/aenm.202000310.

[148] D. Guo, Z. Andaji Garmaroudi, M. Abdi-Jalebi, S. D. Stranks, and T. J. Savenije, “Reversible Removal of Intermixed Shallow States by Light Soaking in Multication Mixed Halide Perovskite Films,” *ACS Energy Lett.*, vol. 4, no. 10, pp. 2360–2367, 2019, doi: 10.1021/acsenergylett.9b01726.

[149] R. García-Rodríguez, D. Ferdani, S. Pering, P. J. Baker, and P. J. Cameron, “Influence of bromide content on iodide migration in inverted MAPb(I1-: XBrx)3 perovskite solar cells,” *J. Mater. Chem. A*, vol. 7, no. 39, pp. 22604–22614, 2019, doi: 10.1039/c9ta08848b.

[150] D. W. Ferdani *et al.*, “Partial cation substitution reduces iodide ion transport in lead iodide perovskite solar cells,” *Energy Environ. Sci.*, vol. 12, no. 7, pp. 2264–2272, 2019, doi: 10.1039/c9ee00476a.

[151] C. Yu, “Advances in modelling and simulation of halide perovskites for solar cell applications,” *J. phys. Energy*, vol. 1, p. 30, 2019.

[152] J. Barrier *et al.*, “Compositional heterogeneity in CsYFA1-yPb(BrxI1-x)3perovskite films and its impact on phase behavior,” *Energy Environ. Sci.*, vol. 14, no. 12, pp. 6394–6405, 2021, doi: 10.1039/d1ee01184g.

[153] S. Sun, Y. Fang, G. Kieslich, T. J. White, and A. K. Cheetham, “Mechanical properties of organic-inorganic halide perovskites, CH3NH3PbX3 (X = I, Br and Cl), by nanoindentation,” *J. Mater. Chem. A*, vol. 3, no. 36, pp. 18450–18455, 2015, doi: 10.1039/c5ta03331d.

[154] S. G. Motti *et al.*, “Defect Activity in Lead Halide Perovskites,” *Adv. Mater.*,

vol. 31, no. 47, pp. 1–11, 2019, doi: 10.1002/adma.201901183.

[155] D. Meggiolaro *et al.*, “Iodine chemistry determines the defect tolerance of lead-halide perovskites,” *Energy Environ. Sci.*, vol. 11, no. 3, pp. 702–713, 2018, doi: 10.1039/c8ee00124c.

[156] Y. Chen and H. Zhou, “Defects chemistry in high-efficiency and stable perovskite solar cells,” *J. Appl. Phys.*, vol. 128, no. 6, 2020, doi: 10.1063/5.0012384.

[157] N. Liu and C. Y. Yam, “First-principles study of intrinsic defects in formamidinium lead triiodide perovskite solar cell absorbers,” *Phys. Chem. Chem. Phys.*, vol. 20, no. 10, pp. 6800–6804, 2018, doi: 10.1039/c8cp00280k.

[158] J. S. Park, J. Calbo, Y. K. Jung, L. D. Whalley, and A. Walsh, “Accumulation of Deep Traps at Grain Boundaries in Halide Perovskites,” *ACS Energy Lett.*, vol. 4, no. 6, pp. 1321–1327, 2019, doi: 10.1021/acsenergylett.9b00840.

[159] I. Levine *et al.*, “Deep Defect States in Wide-Band-Gap ABX3 Halide Perovskites,” *ACS Energy Lett.*, vol. 4, no. 5, pp. 1150–1157, 2019, doi: 10.1021/acsenergylett.9b00709.

[160] I. Levine *et al.*, “Direct probing of gap states and their passivation in halide perovskites by high-sensitivity, variable energy ultraviolet photoelectron spectroscopy,” *J. Phys. Chem. C*, vol. 125, no. 9, pp. 5217–5225, 2021, doi: 10.1021/acs.jpcc.0c11627.

[161] J. Holovský *et al.*, “Lead Halide Residue as a Source of Light-Induced Reversible Defects in Hybrid Perovskite Layers and Solar Cells,” *ACS Energy Lett.*, vol. 4, no. 12, pp. 3011–3017, 2019, doi: 10.1021/acsenergylett.9b02080.

[162] A. Walsh and S. D. Stranks, “Taking Control of Ion Transport in Halide Perovskite Solar Cells,” *ACS Energy Lett.*, vol. 3, no. 8, pp. 1983–1990, 2018, doi: 10.1021/acsenergylett.8b00764.

[163] C. Li, A. Guerrero, S. Huettner, and J. Bisquert, “Unravelling the role of vacancies in lead halide perovskite through electrical switching of photoluminescence,” *Nat. Commun.*, vol. 9, no. 1, p. 8, 2018, doi: 10.1038/s41467-018-07571-6.

[164] A. Senocrate *et al.*, “The Nature of Ion Conduction in Methylammonium Lead Iodide: A Multimethod Approach,” *Angew. Chemie - Int. Ed.*, vol. 56, no. 27, pp. 7755–7759, 2017, doi: 10.1002/anie.201701724.

[165] S. G. Motti *et al.*, “Controlling competing photochemical reactions stabilizes perovskite solar cells,” *Nat. Photonics*, vol. 13, no. 8, pp. 532–539, 2019, doi: 10.1038/s41566-019-0435-1.

[166] J. Holovský *et al.*, “Photocurrent Spectroscopy of Perovskite Layers and Solar Cells: A Sensitive Probe of Material Degradation,” *J. Phys. Chem. Lett.*, vol. 8, no. 4, pp. 838–843, 2017, doi: 10.1021/acs.jpclett.6b02854.

[167] J. H. Yang, W. J. Yin, J. S. Park, and S. H. Wei, “Fast self-diffusion of ions in CH3NH3PbI3: The interstiticaly mechanism: Versus vacancy-assisted mechanism,” *J. Mater. Chem. A*, vol. 4, no. 34, pp. 13105–13112, 2016, doi: 10.1039/c6ta03599j.

[168] A. S. Thind *et al.*, “Atomic Structure and Electrical Activity of Grain Boundaries and Ruddlesden–Popper Faults in Cesium Lead Bromide Perovskite,” *Adv. Mater.*, vol. 31, no. 4, pp. 1–8, 2019, doi: 10.1002/adma.201805047.

[169] D. H. Kang, S. Y. Kim, J. W. Lee, and N. G. Park, “Efficient surface passivation of perovskite films by a post-treatment method with a minimal dose,” *J. Mater. Chem. A*, vol. 9, no. 6, pp. 3441–3450, 2021, doi: 10.1039/d0ta10581c.

[170] C. G. Bischak *et al.*, “Origin of Reversible Photoinduced Phase Separation in Hybrid Perovskites,” *Nano Lett.*, vol. 17, no. 2, pp. 1028–1033, 2017, doi: 10.1021/acs.nanolett.6b04453.

[171] W. Chen, W. Mao, U. Bach, B. Jia, and X. Wen, “Tracking Dynamic Phase Segregation in Mixed-Halide Perovskite Single Crystals under Two-photon Scanning Laser Illumination Weijian Chen , † Wenxin Mao , † Udo Bach , Baohua Jia *, Xiaoming Wen * Dr . W . Chen , † Prof . B . Jia ,* Dr . X . Wen * Centre fo,” 2019.

[172] W. Li *et al.*, “Phase Segregation Enhanced Ion Movement in Efficient Inorganic CsPbIBr2 Solar Cells,” *Adv. Energy Mater.*, vol. 7, no. 20, pp. 1–8, 2017, doi: 10.1002/aenm.201700946.

[173] E. Mosconi, D. Meggiolaro, H. J. Snaith, S. D. Stranks, and F. De Angelis, “Light-induced annihilation of Frenkel defects in organo-lead halide perovskites,” *Energy Environ. Sci.*, vol. 9, no. 10, pp. 3180–3187, 2016, doi: 10.1039/c6ee01504b.

[174] H. Funk, O. Shargaieva, A. Eljarrat, E. L. Unger, C. T. Koch, and D. Abou-Ras, “In Situ TEM Monitoring of Phase-Segregation in Inorganic Mixed Halide Perovskite,” *J. Phys. Chem. Lett.*, vol. 11, no. 13, pp. 4945–4950, 2020, doi: 10.1021/acs.jpclett.0c01296.

[175] T. A. S. Doherty *et al.*, “Performance-limiting nanoscale trap clusters at grain junctions in halide perovskites,” *Nature*, vol. 580, no. 7803, pp. 360–366, 2020, doi: 10.1038/s41586-020-2184-1.

[176] L. A. Frolova *et al.*, “Reversible Pb2+/Pb0 and I−/I3− Redox Chemistry Drives the Light-Induced Phase Segregation in All-Inorganic Mixed Halide Perovskites,” *Adv. Energy Mater.*, vol. 11, no. 12, pp. 1–11, 2021, doi: 10.1002/aenm.202002934.

[177] W. Nie *et al.*, “Light-activated photocurrent degradation and self-healing in perovskite solar cells,” *Nat. Commun.*, vol. 7, no. May, pp. 1–9, 2016, doi: 10.1038/ncomms11574.

[178] G. Y. Kim, A. Senocrate, Y. R. Wang, D. Moia, and J. Maier, “Photo-Effect on Ion Transport in Mixed Cation and Halide Perovskites and Implications for Photo-Demixing,” *Angew. Chemie - Int. Ed.*, vol. 60, no. 2, pp. 820–826, 2021, doi: 10.1002/anie.202005853.

[179] J. M. Gardner, M. Abrahamsson, B. H. Farnum, and G. J. Meyer, “Visible Light Generation of Iodine Atoms and I-I Bonds: Sensitized I- Oxidation and I3- Photodissociation,” *J. Am. Chem. Soc.*, vol. 131, no. 44, pp. 16206–16214, 2009.

[180] S. Tan *et al.*, “Shallow Iodine Defects Accelerate the Degradation of α-Phase Formamidinium Perovskite,” *Joule*, vol. 4, no. 11, pp. 2426–2442, 2020, doi: 10.1016/j.joule.2020.08.016.

[181] L. Hu *et al.*, “Linking Phase Segregation and Photovoltaic Performance of Mixed-Halide Perovskite Films through Grain Size Engineering,” *ACS Energy Lett.*, vol. 6, no. 4, pp. 1649–1658, 2021, doi: 10.1021/acsenergylett.1c00213.

[182] K. Ridzoňová *et al.*, “Correlating light-induced deep defects and phase segregation in mixed-halide perovskites,” *J. Mater. Chem. A*, vol. 10, no. 36, pp. 18928–18938, 2022, doi: 10.1039/d2ta03538c.

[183] T. Baikie *et al.*, “Synthesis and crystal chemistry of the hybrid perovskite (CH 3NH3)PbI3 for solid-state sensitised solar cell applications,” *J. Mater. Chem. A*, vol. 1, no. 18, pp. 5628–5641, 2013, doi: 10.1039/c3ta10518k.